https://doi.org/10.15388/vu.thesis.49

VILNIUS UNIVERSITY
CENTER FOR PHYSICAL SCIENCES AND TECHNOLOGY

Sergejus
BALČIŪNAS

Broadband dielectric spectroscopy of some perovskite compounds

DOCTORAL DISSERTATION

Nature Science,
Physics (N 002)

VILNIUS 2020

This dissertation was written between 2016 and 2020 in Vilnius University.

Scientific supervisor – dr. Maksim Ivanov (Vilnius University, nature sciences, physics – N 002)

https://doi.org/10.15388/vu.thesis.49

VILNIAUS UNIVERSITETAS
FIZINIŲ IR TECHNOLOGIJOS MOKSLŲ CENTRAS

Sergejus
BALČIŪNAS

Kai kurių perovskitinių struktūrų plačiajuostė dielektrinė spektrometrija

DAKTARO DISERTACIJA

Gamtos mokslai,
Fizika (N 002)

VILNIUS 2020

Disertacija rengta Vilniaus Universitete 2016– 2020 metais.

Mokslinis vadovas – dr. Maksim Ivanov (Vilniaus Universitetas, gamtos mokslai, fizika – N 002).

Table of Contents

Abbreviations

MPB	Morphotropic phase boundary
TGS	Triglycine sulphate
SBN	Strontium barium niobate
PZT	Lead zirconate titanate
FA	Formamidium
MA	Methylammonium
DMA	Dimethylammonium
PCE	Power conversion efficiency
MOF	Metal – organic frameworks
PNRs	Polar nano regions

List of samples

BT	$BaTiO_3$
0.22BT/KN	$0.78BaTiO_3 - 0.22KNbO_3$
0.25BT/KN	$0.75BaTiO_3 - 0.25KNbO_3$
ST/KN	$0.75SrTiO_3 - 0.25KNbO_3$
BT/BT	$\frac{2}{3}BaTiO_3 - \frac{1}{3}BaTiO_3$
BF/BT	$\frac{2}{3}BiFeO_3 - \frac{1}{3}BaTiO_3$
$MAPbI_3$	$CH_3NH_3PbI_3$
$MAPbBr_3$	$CH_3NH_3PbBr_3$
$MAPbCl_3$	$CH_3NH_3PbCl_3$
$MA/DMAPbBr_3$	$(CH_3NH_3)_{1-x}((CH_3)_2NH_2)_x PbBr_3$
$DMAZn(HCOO)_3$	$[(CH_3)_2NH_3][Zn][(HCOO)_3]$

1. Introduction

Perovskites are a class of solid-state compounds with a structure of the mineral perovskite, $CaTiO_3$. Perovskites as a group were studied since the middle of the XX century, when first perovskite ferroelectric $BaTiO_3$ was discovered. Since then a large number of different perovskites were synthesized with a huge verity of properties, such as ferroelectricity, piezoelectricity, superionic conductivity, high electric and thermal conductivity, high tensile strength, tunable refractive index and many more. In some cases, perovskites may exhibit several desirable properties such as ferroelectricity and ferromagnetism (multiferroics) for memory devices.

One of the most appealing features of the perovskite structure is the ability to tune perovskite ABX_3 structure by substituting A, B and X cations and anions with other ions. This widens the possibilities but also can produce very complex $A_xA_{x-1}B_yB_{y-1}X_zX_{z-1}$ systems. Due to complexity the nature of the desirable characteristics is not clear. Relaxor ferroelectric is an example of a mixed system. The key feature of relaxor ferroelectric is very high dielectric permittivity value and very slim hysteresis loops although till this day scientist argue to explain the behaviour.

In some mixed systems for example in $PbZr_xTi_{1-x}O_3$ an increase in piezoelectric and ferroelectric properties can be observed. This is usually attributed to the stressed lattice that is created due to different $PbZrO_3$ and $PbTiO_3$ sub lattice sizes. Although many elements can be substituted in ABX_3 perovskite system, it is still limited by Goldschmidt tolerance factor (which describes perovskite stability based on atomic radius). Thus, in some cases a composite with bulk hetero epitaxial interface may be desired. In such system a thin layer of a shell compound surrounds and stresses the lattice of a core compound which may result in improved overall properties. Therefore, in the first part of this work we focus on $BaTiO_3/KNbO_3$, $BaTiO_3/BaTiO_3$ and $BiFeO_3/BaTiO_3$ core/shell systems.

Perovskites may also have organic counterparts in A, B or X position. Recently considerable attention was given to perovskite with organic counterparts $CH_3NH_3PBX_3$ (I, Br, Cl) due to remarkable performance in solar cell industry. It was suggested that the reason for the high performance of as solar cell absorbers is due to ferroelectricity although no concrete evidence was provided. Misconception about ferroelectric nature of organic perovskites is quite common thus it will be addressed in several chapters. Moreover, it was observed that a small amount of $(CH_3)_2NH_2$ (DMA) in A position greatly

increases the stability of $CH_3NH_3PBX_3$ although the solar cell efficiency decreases. Such systems are complicated and considerable attention is required in understanding the effect of the cation and anion replacement.

In this work broadband (10^{-2} - 10^{11}) dielectric spectroscopy results for different perovskites systems from simple inorganic to complex organic will be presented. The experimental investigation is focused on the structural phase transition, dipolar relaxations, effect of mixing organic cations and the strain effect in inorganic core - shell composites. Further we will discuss the issue of the ferroelectricity in the organic perovskites.

1.1 Aim and tasks of the work

The aims of this work are to investigate the effect of the composite core – shell structure to dielectric permittivity in perovskite systems, examine effect of mixing different cations and determine the types of the structural phase transitions in measured organic perovskite systems.

The following tasks were formulated to achieve the aims of this work:

- To investigate the dielectric properties of core – shell system of BT/KN ($BaTiO_3/KNbO_3$) in the broad frequency and temperature range, perform ferroelectric study and calculate spontaneous polarization value from dielectric data and compare with the values obtained in traditional way.
- To perform broadband dielectric study on BT/BT and BF/BT core – shell systems and analyse dielectric behaviour.
- To perform broadband dielectric spectroscopy and ferroelectric measurements for $MAPbI_3$, $MAPbBr_3$ and $MAPbCl_3$ (MA - CH_3NH_3) compounds in the vicinity of phase transition and investigate phase transition type to confirm or deny ferroelectric nature and analyse dipolar dynamics in $MAPbI_3$, $MAPbBr_3$ and $MAPbCl_3$ compounds.
- To investigate the effect of DMA ($(CH_3)_2NH_2$) cation in $DMA_xMA_{1-x}PbBr_3$ perovskite system and analyse dipolar dynamics in those crystals.
- To perform broadband dielectric study on $DMAZn(HCOO)_3$ crystal and investigate structural phase transition and dipolar dynamics.

1.2 Scientific novelty

- BT/KN, BT/BT and BF/BT core-shell samples are sintered using solvothermal reaction method for the first time. Only one group in the world uses this method to prepare barium titanate based samples, to create new piezo

materials with outstanding properties. Thus, our dielectric measurements are unique and new. Also, polarization calculation from dielectric data for core – shell like systems was not yet been done before.

- The $MAPbX_3$ is one of the most widely studied compounds in the past decade due to potentials in solar cell industry. Although at the time of our research broadband dielectric spectroscopy was not performed, therefore results are new. Also, there was a huge debate about ferroelectricity of $MAPBX_3$ in scientific community. Thus, the nature of the structural phase transition and dielectric spectroscopy data is new and very important.
- Considering the popularity of $MAPbBr_3$ in the scientific community and the focus to improve the compound by changing different cations and anions and also the fact that during sintering traces of DMA can be found in the $MAPbBr_3$ it is very important to know the effect of DMA cations in $MAPbBr_3$ structure. Therefore, for the first-time dielectric data of $DMA_xMA_{x-1}PbBr_3$ crystals was measured and the effect of DMA molecule in $MAPbBr_3$ compound was investigated, thus results are new.
- There was no dielectric data on $DMAZn(HCOO)_3$ systems and also it was not clear if $DMAZn(HCOO)_3$ is ferroelectric or not. Thus, broadband dielectric data in the vicinity of the phase transition and ferroelectric measurements are novel.

1.3 Author contribution

In this dissertation all experimental data, calculations and approximations presented in the third chapter „Results and discussion“ were performed by the Author. This includes broadband dielectric spectroscopy, ferroelectric, acoustic, IR, pyroelectric measurements. Although I would like to mention that Acoustic results were obtain under supervision of Vytautas Samulionis. And result shown in Appendix are not performed by the Author (accept Appendix B Figure 1 and Appendix C Figure 1). Also I would like to note that a preview of dielectric spectroscopy results for $DMAZn(HCOO)_3$ crystals were shown in “Appendix D” in M. Šimėnas dissertation.

Furthermore, samples investigated in this work were produce by colleagues, such as prof. dr. S. Wada, prof. dr. D. Lupascu and prof. dr. Miroslaw Maczka group. The Authors contribution concerning sample preparation was cutting, polishing and applying silver paste before measurements.

1.4 Statements presented for defence

1. The main contribution to dielectric permittivity in BT/KN, BT/BT "core – shell" system is due to electro – mechanical resonance. The increase in the spontaneous polarization value in BT/KN can be considered as an indication of an artificial MPB.
2. At low temperatures first – order, order – disorder, anti-polar phase transitions are observed in $MAPbX_3$ (I, Br, Cl) compounds also those compounds cannot be classified as ferroelectrics. High dielectric permittivity values are attributed to MA cation dipolar relaxation.
3. A small amount up to 4 % of DMA cation in the $MA_{1-x}DMA_xPbBr_3$ crystals leads to a shift of the phase transition temperature to the lower temperatures. And higher amount of DMA cations concentration results in significant broadening and suppression of tetragonal phase, due to frustrated state.
4. $DMAZn(HCOO)_3$ undergoes first – order, non – ferroelectric phase transition at 155 K temperature from trigonal to monoclinic phase. And high temperature phase is dominated by DMA molecule dipolar relaxation.

1.5 Publications related to thesis

1. S. Balčiūnas, M. Ivanov, J. Banys, S. Wada, "Dielectric Properties Of BaTiO3-KNbO3 Composites", Ferroelectrics. 2017 May 19;512(1):8-13, Impact Factor 0.491 [1].
2. I. Anusca, S. Balčiūnas, P. Gemeiner, Š. Svirskas, M. Sanlialp, G. Lackner, C. Fettkenhauer, J. Belovickis, V. Samulionis, M. Ivanov, B. Dkhil, J. Banys, V. V. Shvartsman and D. C. Lupascu, "Dielectric Response: Answer to Many Questions in the Methylammonium Lead Halide Solar Cell Absorbers", Advanced Energy Materials, 2017, 7.19, Impact Factor 15.23 [2].
3. S. Balčiūnas, M. Ivanov, M. Watanabe, K. Matsumoto, S. Ueno, I. Fujii, J. Banys, S. Wada "Dielectric properties of BT-BT and BF-BT composites" Ferroelectrics. 2018 Sep 10;533(1):145-50. Impact Factor 0.53.[3]
4. M. Šimėnas, S. Balčiūnas, M. Mączka, J. Banys and E. E. Tornau „Exploring Antipolar Nature of Methylammonium Lead Halide Perovskites: a Monte Carlo and Pyrocurrent Study", Physical chemistry letters, 2017, 8.19: 4906-4911, Impact Factor 9,353 [4].

5. M. Šimėnas, S. Balčiūnas, A. Ciupa, L. Vilčiauskas, D. Jablonskas, M. Kinka, A. Sieradzki, V. Samulionis, M. Ma, J. Banys "Elucidation of dipolar dynamics and the nature of structural phases in the [(CH 3) 2 NH 2][Zn (HCOO) 3] hybrid perovskite framework" Journal of Materials Chemistry C. 2019;7(22):6779-85, Impact factor: 6.641 [5].

Publications that are related to thesis but not yet published:

1. M. Simenas, S. Balciunas, J. N. Wilson, S. Svirskas, M. Kinka, A. Garbaras, A. Gagor, A. Sieradzki, M. Maczka, V. Samulionis, A. Walsh, R. Grigalaitis, J. Banys "Emergence of a glassy phase from frustrated dipoles in mixed cation halide perovskites", Nature communication, **Submitted.**
2. S. Balčiūnas, M. Ivanov, J. Banys, S. Ueno, S. Wada "In search of an artificial morphotropic phase boundary: lead free barium titanate based composite structure", Journal of Electroceramics, **submitted**.

1.6 Other publication

1. S. Balčiūnas, M. Ivanov, R. Grigalaitis, J. Banys, H. Amorín, A. Castro, "Revisiting the broadband dielectric properties of high-sensitivity piezoelectric BiScO3–PbTiO3: Size effects", physica status solidi (b), 2015, vol. 252, pp. 2727-2734, Impact Factor 1.522.
2. F. B. Tahar, C. Hrizi, S. Chaabouni, N. Chniba-Boudjada, N. R. Ramond, S. Balčiūnas, M. Ivanov, R. Mackevičiūtė, J. Banys, R. Chtourou, "Synthesis, Crystal structure, Vibrational, Optical and Dielectric properties Of 2-(2-Aminoethyl)-1-methylpyrrolidinum chloride hexachlorobismuthate (III) monohydrate [C7H18N2]2ClBiCl6.H2O", Journal of Advances in Chemistry,2014, Vol 9, No 3, pp. 2005-2022, No impact.
3. M. Simenas, S. Balciunas, M. Maczka, J. Banys and E. Tornau, "Structural Phase Transition in Perovskite Metal-Formate Frameworks: a Potts-Type Model with Dipolar Interactions", Physical Chemistry Chemical Physics, 2016, 18.27: 18528-18535, Impact Factor 4.449.
4. M. Mączka, M. Ptak, S. Pawlus, W. Paraguassu, A. Sieradzki, S. Balciunas, M. Simenas and J. Banys, "Temperature- and pressure-dependent studies of niccolite-type formate frameworks of [NH3(CH2)4NH3][M2(HCOO)6] (M = Zn, Co, Fe)†" Physical Chemistry Chemical Physics, 2016, 18.39: 27613-27622, Impact Factor 4.449.

5. M. Šimėnas, S. Balčiūnas, M. Trzebiatowska, M.j Ptak, M. Mączka, G. Völkel, A. Pöppl and J. Banys "Electron paramagnetic resonance and electric characterization of [CH 3 NH 2 NH 2][Zn (HCOO) 3] perovskite metal formate framework." Journal of Materials Chemistry C, 2017, 5(18), 4526-4536, Impact Factor 5.066.
6. M. Šimėnas, A. Kultaeva, S. Balciunas, M. Trzebiatowska, D. Klose, G. Jeschke, M. Maczka, J. Banys, A. Pöppl "Single Crystal Electron Paramagnetic Resonance of Dimethylammonium and Ammonium Hybrid Formate Frameworks: Influence of External Electric Field" The Journal of Physical Chemistry C. 2017 Jul 13, 121.30, 16533-16540, Impact Factor 4.536.
7. S. Balčiūnas, A. Peterson, M. Ivanov, J. Adamson, J. Banys "Dielectric properties of one-dimensional ice in HHTP-4H2O crystallites." Ferroelectrics. 2018 Sep 10;533(1):192-7, Impact Factor 0.53.
8. S. Balčiūnas, M. Ivanov, R. Grigalaitis, J. Banys, H. Amorín, A Castro, and M. Algueró „Kittel type behaviour of the permittivity of a nanostructured high sensitivity piezoelectric“, Journal of Applied Physics, 2018, volume 123: 20, Impact Factor 2.1.
9. S. Adam, M. Maczka, M. Simenas, J. K. Zaręba, A. Gągor, S. Balciunas, M. Kinka et al. "On the origin of ferroelectric structural phases in perovskite-like metal-organic formate." Journal of Materials Chemistry C 2018 Aug 13, Impact Factor 5.976.
10. M. Rok, G. Bator, W. Medycki, M. Zamponi, S. Balciunas, M. Simenas and J. Banys. "Reorientational dynamics of organic cations in perovskite-like coordination polymers." Dalton Transactions, 2018 Nov 14, Impact Factor 4.099.
11. S. Balciunas, M. Šimėnas, D. Pavlovaite, M. Kinka , F.K. Shieh, K.C. Wu, J. Banys, R. Grigalaitis "Low-Frequency Dipolar Dynamics and Atmospheric Effects in ZIF-90 Metal-Organic Framework" The Journal of Physical Chemistry C. 2018 Dec 1, Impact factor 4.536.
12. M. Šimėnas, S. Balciunas, A. Gonzalez-Nelson, M. Kinka, M. Ptak, M.A. Van Der Veen, M. Maczka, J. Banys "Preparation and Dielectric Characterization of P (VDF-TrFE) Copolymer Based Composites Containing Metal-Formate Frameworks" The Journal of Physical Chemistry C. 2019 Jun 12, Impact Factor 5.976.
13. M. Trzebiatowska, M. Maczka, M. Ptak, L. Giriunas, S. Balciunas, M. Šimėnas, D. Klose, J. Banys "Spectroscopic Study of Structural Phase Transition and Dynamic Effects in [(CH3] 2NH2][Cd (N3) 3] Hybrid

Perovskite Framework" The Journal of Physical Chemistry C. 2019 May 9 Impact Factor 4.309.

14. L. Dagys, S. Balčiūnas, J. Banys, F. Kuliešius, V. Chizhik, V. Balevičius "CP MAS kinetics and impedance spectroscopy studies of local disorder in low-dimensional H-bonded proton-conducting materials" Lithuanian Journal of Physics. 2019 Oct 28;59(3), Impact Factor 0.822.

15. M. Mączka, A. Gagor, J. K. Zaręba, D. Stefanska, M. Drozd, S. Balciunas, M. Šimėnas, J. Banys, A. Sieradzki, „Methylhydrazinium Lead Chloride Is a Three-dimensional perovskite That Features Two Polar Phases and Unusual Second-Harmonic Generation Bistability Above Room Temperature", Chemistry of Materials. 2020 April 13, just accepted, Impact Factor 10.159.

16. S. Balčiūnas, D. Pavlovaitė, M. Kinka, J.-Y. Yeh, P.-C. Han, F.-K. Shieh, K C.-W. Wu, M. Šimėnas, R. Grigalaitis, J. Banys |"Dielectric Spectroscopy of Water Dynamics in Functionalized UiO-66 Metal-Organic Frameworks", Molecules, 2020 March 21, just accepted, Impact Factor 3.06.

1.7 Oral presentations and Internships.

1. Sergejus Balčiūnas, Maksim Ivanov, Jūras Banys, Satoshi Wada, "Dielectric Properties Of $BaTiO_3$-$KNbO_3$ Composites", Properties of ferroelectric and superionic systems, Uzhhorod, Ukraine, 2016 – 11 – 17..18, page 13.
2. Sergejus Balčiūnas, Maksim Ivanov, Jūras Banys, Satoshi Wada, "Dielectric Properties Of $BaTiO_3$-$KNbO_3$ Composites ", Functional materials and nanotechnologies, Tartu, Estonia, 2017 - 04 - 24..28, page 74.
3. Sergejus Balčiūnas, Maksim Ivanov, Jūras Banys, Satoshi Wada "Dielectric Properties Of $BaTiO_3$-$KNbO_3$ Composites", Modern Multifunctional Materials and Ceramics, Vilnius, Lithuania 2017-04-19-20, page 15.
4. Sergejus Balčiūnas, Maksim Ivanov, Jūras Banys, Satoshi Wada, "Porous barium titanate composites: in search of artificial MPBs", UPL – 2018, Ukraine, Uzhgorod, 2018-09-18....20, page 32.

Internships:

1. 2017-05-28 to 2017-06-28 Belarus, Minsk (Practical – Scientific material science center).
2. 2017-11-25 to 2017-11-30 Japan, Kofu. (Interdisciplinary Graduate School of Medical and Engineering, University of Yamanash).
3. 2017-12-05 to 2017-12-10 Belarus, Minsk (Laboratory of Electrodynamics of Nonhomogeneous Media).
4. 2017-12-13 to 2017-12-17 Belarus, Minsk (Laboratory of Electrodynamics of Nonhomogeneous Media).
5. 2018-04-02 to 2018-04-22 Belarus, Minsk (Practical – Scientific material science center).
6. 2018-05-14 to 2018-05-20 Belarus, Minsk (Laboratory of Electrodynamics of Nonhomogeneous Media).

1.8 Poster presentation by the author

1. Sergejus Balčiūnas, Maksim Ivanov, Jūras Banys, Satoshi Wada, "Dielectric properties of $BaTiO_3$-$KNbO_3$ composites" Open readings 2017, Vilnius, Lithuania, 2017-03-14..17, page 257.
2. Sergejus Balčiūnas, Maksim Ivanov, Jūras Banys, Satoshi Wada „Dielectric properties of $BaTiO_3$ based composites“, International Meeting on ferroelectricity, San Antonio, USA, 2017-09-04-08, page 87.
3. Sergejus Balčiūnas, Anna Peterson, Maksim Ivanov, Jasper Adamson, Jūras Banys „Dielectric properties of HHTP-4H2O cold pressed pellets“, International Meeting on ferroelectricity, San Antonio, USA, 2017-09-04-08, page 201.
4. Sergejus Balčiūnas, Maksim Ivanov, Jūras Banys, Satoshi Wada, "Dielectric Properties Of $BaTiO_3$ Based Composites", 42-oji Lietuvos Nacionalinė Fizikos Konferencija, Vilnius, Lithuania, 2017 – 10 – 04..06, page 217.
5. Sergejus Balčiūnas, Anna Peterson, Maksim Ivanov, Jasper Adamson, Jūras Banys, "Dielectric Properties of one dimensional ice in HHTP-4H2O crystallites", 42-oji Lietuvos Nacionalinė Fizikos Konferencija, Vilnius, Lithunia, 2017 – 10 – 04..06, page 218.
6. Sergejus Balčiūnas, Maksim Ivanov, Jūras Banys, Satoshi Wada "Dielectric Properties Of $BaTiO_3$ Based Composites", ISAF-FMA-AMF-AMEC-PFM, Hiroshima, Japan, 2018 – 05–27..01, 28pm-P047A.

7. S. Balčiūnas, R. Grigalaitis, D. Pavlovaitė, M. Šimėnas, M. Kinka, J. Banys, F.-K. Shieh and K. C.-W. Wu „Dielectric Properties of ZIF-90 and UiO-66 Metal-Organic Frameworks“, ISAF-FMA-AMF-AMEC-PFM, Hiroshima, Japan, 2018 – 05–27..01, 30pm-P125A.
8. S. Balciunas, I. Anusca, ,P. Gemeiner, S. Svirskas, M. Sanlialp, G. Lackner, C. Fettkenhauer, J. Belovickis, V. Samulionis, M. Simena, E. Tornau, M. Ivanov, B. Dkhil, J. Banys, V. V. Shvartsman and D. C. Lupascu, „Dielectric and Ultrasonic studies of the Methylammonium Lead Halide Solar Cell Absorbers“ ECAPD 2018, Russia, Moscow, 2018 – 06 25...28, 1 - 20.
9. Sergejus Balčiūnas, Maksim Ivanov, Jūras Banys, Satoshi Wada „Dielectric Properties Of barium titanate Based Composites“, Electroceramics XVI, Belgium, Hasselt, 2018 – 07 – 9...12, PS-1C.06.
10. Sergejus Balčiūnas, Maksim Ivanov, Jūras Banys, Satoshi Wada, Dielectric Properties of $BaTiO_3$ Based Composites, FMNT – 2018, Latvia, Ryga, 2018-10-2....5, PO-81.
11. Sergejus Balciunas, Karpavičius, Augustas, Maksim Ivanov, Jūras Banys, Satoshi Wada, „Dielectric Properties of $BaTiO_3$ Based Composites”, EMF – 2019, Switzerland, Lausanne, 2019-07-14…19, ThPOiiPosters.19.
12. Sergejus Balciunas, Maksim Ivanov, Jūras Banys, Satoshi Wada, “Dielectric Properties Of barium titanate Based Composites” EMN-Ceramics, Korea, Jeju, 2019 – 06 – 20…24, P-01.
13. Sergejus Balčiūnas, Maksim Ivanov, Jūras Banys, Satoshi Wada, „Dielectric Properties of $BaTiO_3$ Based Composites”, 43-oji Lietuvos Nacionalinė Fizikos Konferencija, Vilnius, Lietuva, 2019 – 10 – 03..05, page 209.
14. S. Balciunas, A. Karpavicius, M. Ivanov, J. Banys, S. Wada, „Dielectric Properties of Barium Titanate Based Composites?“, Electronic Materials and Applications 2020, Orlando, USA, 2020 – 01 – 22 ... 24, page 35

1.9 Co-author in other presentations

1. Sergejus Balčiūnas, Maksim Ivanov, Jūras Banys, Satoshi Wada "Dielectric Properties Of $BaTiO_3$-$KNbO_3$ Composites" Joint IEEE ISAF-IWATMD-PFM Conference, Atlanta, GA, J.A.V. 2017-04-7...11, page II 23.

2. Maksim Ivanov, Sergejus Balčiūnas, Jūras Banys, Satoshi Wada „In search for artificial MPBs: Dielectric spectroscopy of $BaTiO_3$-$KNbO_3$ composites“, International Meeting on ferroelectricity, San Antonio, USA, 2017-09-04-08, page 32.
3. Mantas Simenas, Sergejus Balciunas, Monika Trzebiatowska-Gusowska, Miroslaw Maczka, Georg Völkel, Andreas Pöppl, Juras Banys „Phase transitions in dense perovskite formate frameworks: EPR and dielectric study“, International Meeting on ferroelectricity, San Antonio, USA, 2017-09-04-08, page 76.
4. Mantas Šimėnas, Sergejus Balčiūnas, Jūras Banys, Evaldas E. Tornau, "Methylammonium lead iodide – a model for a sequence of structural phase transitions", 42-oji Lietuvos Nacionalinė Fizikos Konferencija, Vilnius, Lithuania, 2017 – 10 – 04..06, page 118.
5. Maksim Ivanov, Sergejus Balčiūnas, Jūras Banys, Satoshi Wada "In search for artificial MPBs: dielectric spectroscopy of $BaTiO_3$-$KNbO_3$ composites", 42-oji Lietuvos Nacionalinė Fizikos Konferencija, Vilnius, Lithuania, 2017 – 10 – 04..06, page 182.
6. I. Anusca, S. Balciunas, P. Gemeiner, S. Svirskas, M. Sanlialp, G. Lackner, C. Fettkenhauer, J. Belovickis, V. Samulionis, M. Simena, E. Tornau, M. Ivanov, B. Dkhil, J. Banys, V. V. Shvartsman and D. C. Lupascu, „Dielectric and Ultrasonic studies of the Methylammonium Lead Halide Solar Cell Absorbers“, ISAF-FMA-AMF-AMEC-PFM, Hiroshima, Japan, 2018 – 05–27..01, 30am-H07.
7. Sergejus Balčiūnas, Mantas Šimėnas, Šarūnas Svirskas, Jaroslavas Belovickis, Vytautas Samulionis, Maksim Ivanov, Jūras Banys, Irina Anusca, Mehmet Sanlialp, Gerhard Lackner, Christian Fettkenhauer, Vladimir V. Shvartsman, Doru C. Lupascu, Pascale Gemeiner, Brahim Dkhil, „Dielectric Response of the Methylammonium Lead Halide Solar Cell Absorbers“, UPL – 2018, Ukraine, Uzhgorod, 2018-09-18....20, page
8. A.Sieradzki, M.Mączka, M. Šimėnas, A. Ciupa, M.Ptak, J.K.Zaręba, A.Gągor, S. Balčiūnas, M. Kinka, M. Nyk, V. Samulionis, J. Banys, M.Palush, S.Pawlus, Ferroelectricity in Perovskite-Like Metal – Organic – formates, UPL – 2018, Ukraine, Uzhgorod, 2018-09-18....20, page 12.
9. R. Grigalaitis, D. Pavlovaitė, S. Balčiūnas, M. Šimėnas, M. Kinka, J. Banys, F.-K. Shieh, and K. C.-W. Wu, “Dielectric response of ZIF-90 and UiO-66 metal-organic frameworks under different gas atmospheres”, FMNT – 2018, Latvia, Ryga, 2018-10-2....5, PO-82.

10. R. Grigalaitis, D. Pavlovaitė, S. Balčiūnas, M. Šimėnas, M. Kinka, J. Banys, F.-K. Shieh, and K. C.-W. Wu, Satoshi Wada, „Water Dynamics in ZIF-90 and UiO-66 Metal-Organic Frameworks", EMF – 2019, Switzerland, Lausanne, 2019-07-14…19, ThPOiiPosters.6.
11. Diana Pavlovaite, Sergejus Balčiūnas, Mantas Šimėnas, Martynas Kinka, Fa-Kuen S, Kevin C.-W Wu, Jūras Banys and Robertas Grigalaitis, „Low frequency dielectric properties and atmosferic effect of ZIF-90 metal-organic framework", 43-oji Lietuvos Nacionalinė Fizikos Konferencija, Vilnius, Lithuania, 2019 – 10 – 03..05, page 186.
12. Augustas Karpavičius, Sergejus Balčiūnas, Maksim Ivanov, Satoshi Wada, Jūras Banys, Dielectric Properties of BT-BT and BF-BT composites, 43-oji Lietuvos Nacionalinė Fizikos Konferencija, Vilnius, Lithuania, 2019 – 10 – 03..05, page 189.
13. Rytis Šalaševičius, Sergejus Balčiūnas, Jūras Banys, Satoshi Wada, „Broadband dielectric spectroscopy of nanocomposite materials", 43-oji Lietuvos Nacionalinė Fizikos Konferencija, Vilnius, Lithuania, 2019 – 10 – 03..05, page 214.
14. J. Banys, S.Svirkas, R. Grigalaitis, D. Adamchuk, J.Macutkevic S.Balciunas, D.Jablonkas, „What is common between relaxors and dipolar glasses? Are they different?", Electronic Materials and Applications 2020, Orlando, USA, 2020 – 01 – 22 ... 24, page 22.

2. Overview

This chapter is for less experienced users in the broadband spectroscopy field to introduce necessary understanding in fundamental physics. Here we will discuss the basics of phase transitions, ferroelectricity, perovskite structure and dielectric spectra. Also, in this chapter readers will find necessary information about sample preparations, measurement techniques.

2.1 Structural phase transitions

According to principal of minimal energy a system at equilibrium will have the lowest possible energy values. The particular value is strongly dependant on configuration or position of the atoms. Thus, we could imagine a lot of different atom configurations but during equilibrium condition only one configuration is stable. Further each configuration is effected by external factors such as pressure, temperature, or even electric and magnetic fields. Also, for each atom arrangement the effect of external factor to the minimal energy values are different. This means different external condition may deliver various atom structures. A particular arrangement of atoms is called a phase and a phenomenon during which one phase changes to another phase is called a phase transition. It is possible to calculate lowest possible energies using Gibs free energy potential. A simple case is when external factors are pressure and temperature:

$$G(T,p) = U + pV - TS \tag{2.1}$$

here G is Gibs free energy, T – temperature, p – pressure, U – internal energy, V – volume, S – entropy. When two different Gibs potential curves intersect a phase transition is observed and the stable phase is the phase with lowest energy (Figure 2.1) [6], [7].

Compared to liquid and gaseous phases solids can be arranged in many more ordered ways. For example, a crystal phase based on space group symmetry elements has 230 different possibilities. Thus most solids can have several crystal phases and the stability of the specific phase is based on external factors [7]. During a phase transition one phase changes to another this means we have a symmetry breaking point. Close to this point it is usual to observe anomalous behaviour of physical properties.

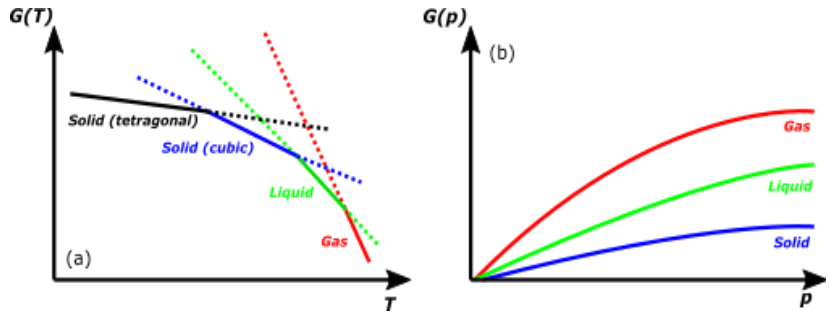

Figure 2.1 Temperature (a) and pressure (b) dependence of Gibs free energy.

The structural phase transitions are classified in several groups: ferro-distortive or anti-distortive, order-disorder or displacive, first-order or second-order. A distortive phase transition is such phase transition during which atoms move from one position to the other. In other words, if atoms change their location during phase transition, we call this phenomenon distortive phase transition. During ferro-distortive phase transition atom position change in a way that the number of atoms in the unit cells remain the same. If the number of atoms in the cell size increases it means we have an anti-distortive phase transition (Figure 2.2 [7]).

Also some crystals during ferro-distortive phase transition show the appearance of spontaneous polarization, such crystals are called pyroelectrics (e.g. TGS [8], $LiTaO_3$ [9], SBN [10]) and the temperature at which this phase transition occurs is called Curie temperature T_c. A pyroelectric crystal is a ferroelectric, if it is possible to change the direction of spontaneous polarization with external electrical field. Examples of ferroelectric crystals would be barium titanate [11], Rochelle salt [12], lead titanate [13]. Anti-polar phase transition is such phase transition during which spontaneous polarization is cancelled by opposite dipoles in each sub-lattice. For certain anti-polar crystals is possible to induce ferroelectric phase by high external

electrical field. Those crystals are called anti-ferroelectric crystals (e.g. $PbZnO_3$ [14], $NaNbO_3$ [15], $NH_4H_2PO_4$ [16]) [7].

Furthermore, phase transitions can be classified into order-disorder or displacive types. During order-disorder phase transition we can imagine that atom have two potential wells. At high temperatures, above phase transition atoms can move easily between those positions, so statistically the average position is in the middle. Below Curie temperature the barrier between the

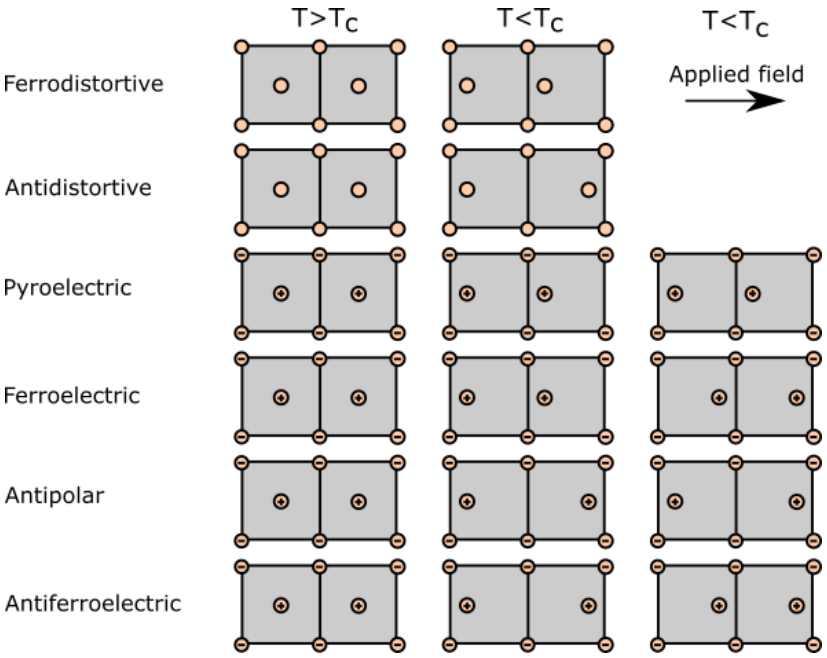

Figure 2.2 Classification of structural phase transition.

wells is too high so atoms are forced to stay in one random well. During displacive structural phase transition high temperature phase has only one potential well this means atoms positions doesn't change. Lower temperature phase has two potential wells. Similarly, as in order-disorder type atoms are force to stay in a well. It is possible to force atoms from one potential minima to another using external forces. For example it is possible polarize (force atom to particular well) ferroelectric materials using high electrical fields [7].

Lastly phase transition can be categorized by first or second order phase transition. It is typical that in the vicinity of a phase transition we observe anomalous behaviour of physical properties such as volume, dielectric permittivity, conductivity, heat capacity and etc. [7], [17], [18]. A sudden and

abrupt change of physical properties usually suggest that we have first-order phase transition. From thermodynamic point of view first order phase transitions are those that either absorbs or releases a fixed amount of latent heat. During phase change temperature of the system will stay the same, we will observe a mix phase regime, where parts of a system are still in other phase. A very sharp peak is observed during calorimetric measurements, which is significant fingerprint of the first-order phase transition [19]–[21]. In addition to this a temperature hysteresis could be observed during thermal cycling. Due to sharp changes in physical properties first-order phase transition are often called discontinuous phase transitions. A second-order phase transition also called continuous phase transition that display a slow change of physical properties over wide temperature range. One of the main characteristic is infinite correlation length this means a small change in physical properties is observed over whole system thus a mix phase regime or temperature hysteresis is impossible [17]. A second-order and partly first-order phase transitions can be mathematically describe using Landau theory which is covered in the next section.

2.2 Ferroelectricity

Ferroelectricity is a phenomenon that is similar to ferromagnetism. At temperature below T_c we observe an appearance of spontaneous polarization. Although this not sufficient condition to describe ferroelectric material and only describes pyroelectric materials. Typically, ferroelectric crystals are divided into regions with the same polarization direction. Those regions are called domains and they are separated by domain walls. Ferroelectricity is purely engineering term and in order to classify ferroelectric materials we have to be able to change and control polarization direction by applying external electrical field [22]. The ferroelectric phase transitions can be characterized by Landau phenomenological theory. Central point of the theory is order parameter η, which measures the degree of order in a system (we can imagine order parameter as the distance particular atom is displaced from his position). In ferroelectric case order parameter has to be couple with spontaneous polarization. Furthermore, in a vicinity of a phase transition order parameter grows. The growth depends on the type of a phase transition which is depicted in figure 2.3 [7].

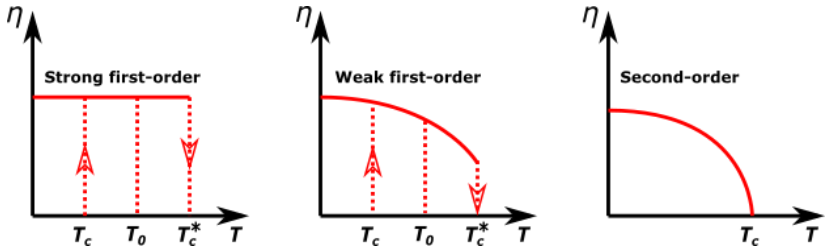

Figure 2.3 Temperature dependence of the order parameter: first-order phase transition left, second order phase transition right, and first order close tom second order in the middle.

We will treat order parameter η as the variable of incomplete thermodynamic potential. In a vicinity of second-order phase transition we will limit our self with small lattice distortions thus we can expand Gibs potential in series:

$$G(T,\eta) = G_0 + a\eta + A\eta^2 + b\eta^3 + B\eta^4 + \cdots. \qquad (2.2)$$

Also, it should be said that the sign of the order parameter depends on the choice of the coordinates but Gibb's function cannot depend on the

coordinates. This means our order parameter from the point of view of thermodynamic potential has to be invariant:

$$G(\eta) = G(\eta^*). \tag{2.3}$$

Thus, we can ignore odd members and Gibs potential assumes the following form:

$$G(T,\eta) = G_0 + A(T)\eta^2 + B(T)\eta^4. \tag{2.4}$$

In a vicinity of T_c coefficient A(T) has to change sign to satisfy non-symmetry phase condition $\eta \neq 0$. Thus, we expand A(T) in series:

$$A(T) = A(T_C) + A'(T - T_c) + A''(T - T_C)^2 + \cdots. \tag{2.5}$$

Note that $A(T_c)$ is equal to zero at phase transition temperature, thus if we limit our self with limited number of members:

$$G(T,\eta) = G_0 + \frac{1}{2}\alpha(T - T_c)\eta^2 + \frac{1}{4}\beta\eta^4 + \cdots. \tag{2.6}$$

Here $\alpha = 2A$, and $\beta = 4B$ (just for convenience). Further we can find temperature dependence of order parameter η_0 from conditions:

$$\frac{\partial G}{\partial \eta} = 0, \qquad \frac{\partial^2 G}{\partial \eta^2} > 0. \tag{2.7}$$

Thus:

$$\eta = \begin{cases} \eta_0 = 0 & T > T_C \\ \eta_0 = \left(\frac{\alpha(T_c - T)}{\beta}\right)^{1/2} & T < T_C \end{cases}. \tag{2.8}$$

As in second-order phase transition case Landau phenomenological theory can calculate order parameter dependence for weak first-order phase transition. Here thermodynamic potential has to be expanded up to the sixth term:

$$G(T,\eta) = G_0 + \frac{1}{2}\alpha(T - T_c)\eta^2 + \frac{1}{4}\beta\eta^4 + \frac{1}{6}\gamma\eta^6 + \cdots. \tag{2.9}$$

It should be noted that β coefficient has to be negate otherwise the case of second order phase transition will be observed. The temperature dependence of the order parameter for the weak first order phase transition can be described with:

$$\eta = \begin{cases} \eta_0 = 0 & T > T_C \\ \eta_0 = \frac{\beta}{2\gamma}\left[1 \pm \left(1 - \frac{4\alpha(T_c - T)\gamma}{\beta^2}\right)^{1/2}\right] & T < T_C \end{cases}. \tag{2.10}$$

The comparison of thermodynamic potential on η between first and second order phase transition is shown in figure 2.4. Here it is observed that during second-order phase transition the transition between phases is smooth and

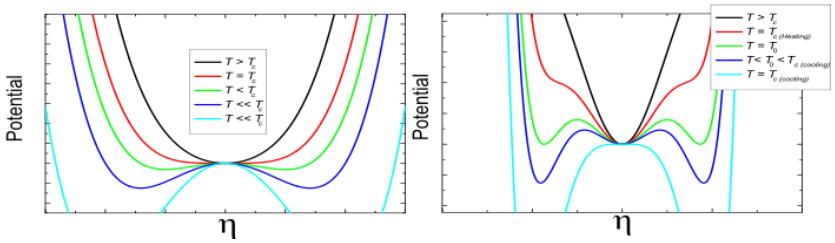

Figure 2.4 Thermodynamic potential dependence of order parameter for first-order (right) and second-order (left) phase transitions.

continuous and at the Curie point one phase changes to another. The situation for the other case is a bit more complicated. There is a temperature range where order parameter can have values: $\eta = 0$ and $\eta \neq 0$. This means that a symmetrical phase and non-symmetrical phase can coexist, respectively. Phase transition occurs at T_0 (figure 2.3) temperature if the duration of the experiment is infinite also T_0 is the temperature when the depths of all potential wells are equal. During a cooling cycle a phase transition will be observed when minimum at $\eta = 0$ fades and during heating cycle when minimum's at $\eta \neq 0$ disappears. Hence this is the nature for temperature hysteresis for first-order phase transitions.

One of the main features of ferroelectric materials is high dielectric constant value. Landau phenomenological theory allows us to predict the behaviour of static dielectric permittivity values. The expression of the thermodynamic potential for ferroelectric materials follows:

$$G(T,\eta) = G_0 + \frac{1}{2}\alpha(T - T_c)\eta^2 + \frac{1}{4}\beta\eta^4 + \cdots - a\eta\text{E}. \qquad (2.11)$$

We should note that spontaneous polarization for ferroelectric materials is couple with order parameter, thus $P = a\eta$. From equation 2.11 we can calculate the relationship of static dielectric permittivity versus temperature which is the second derivative with respect to an electrical field:

$$\varepsilon = \frac{C_{CW}}{T - T_C} \qquad (2.12)$$

Here ε – is static dielectric permittivity C_{cw} – Curie Weiss constant. Curie Weiss law is applicable for ferroelectric and ferromagnetic materials and can provide extra information about the nature of the phase transitions. Therefore

very high Curie-Weiss constant values can suggest about displacive type phase transition ($BaTiO_3$ $C_{cw} = 1.73x10^5$ [23]), and low values – suggest about order-disorder type phase transition (Rochelle salt C_{cw} =178 [24]). Furthermore, it is possible to distinguish first-order and second-order phase transition from the ratio of Curie Weiss constants of paraelectric and ferroelectric phases. This ratio for the second-order phase transition can be calculated from Landau theory and is equal to 2 and for first order phase transition this number is a lot higher. [7], [17], [18].

2.3 Perovskite Oxides

Perovskite is a material which has a crystal structure of the mineral calcium titanium oxide also called perovskite [25]. The ideal structure is cubic and formula of the perovskite is ABX_3. Here A cation is 12-fold coordinated and B cation 6 fold coordinated with X anion. One of the most famous perovskite ferroelectrics is barium titanate which is depicted in figure 2.5. Here Barium with valence of +2 is in the middle of the unit cell. Furthermore, we have titanium with valence of +4 surrounded by oxygen atoms forming an octahedral shape. Oxygen has the valence of -2 thus charge neutrality condition is satisfied.

Perovskite structure is very versatile over 90% metallic elements in the periodic table can be used to synthesize a stable perovskite structure [26]. The main restriction in atom selection process is the radius of the atoms. In an ideal perovskite structure, A cation is always larger then B cation. Furthermore, the distance between centers of B-X atoms is half of a unit cell a and the distance between A-X is $a/\sqrt{2}$. As measure of deviation from the perfect structure Goldschmidt introduced a perovskite tolerance factor t [27]:

$$t = \frac{r_A + r_X}{\sqrt{2}(r_B + r_X)}. \tag{2.13}$$

Here r_A, r_B and r_X is radii of A and B cations and X anion, respectively. The perovskite structure is stable if Goldschmid factor values are in between of $0.75 < t < 1$ [27]. Due to distortions perovskite crystals can have wide variety of phases such as tetragonal, orthorhombic, rhombohedral, monoclinic and triclinic. The structure usually depends on the radii of the cations. Moreover a large ion in the center of the anion octahedra can lead to octahedral tilting [28].

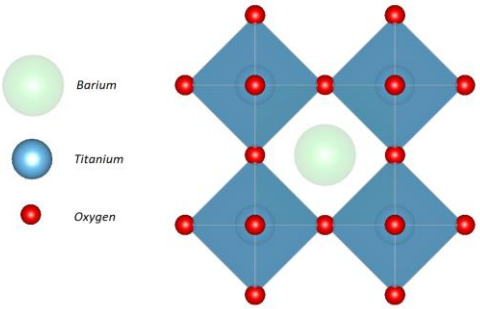

Figure 2.5 Schematic representation of barium titanate perovskite structure.

Apart from ionic radius there is a second condition which is electro-neutrality. The sum of cation charges has to be the same as anion charge. This can be attained using appropriate ions, for example: $A^{1+}B^{5+}X$, $A^{2+}B^{4+}X$ or $A^{3+}B^{+3}X$. Further there is possibility to produce mix systems. It's possible to partially substitute A or B cations with another as long as cation sizes are similar. One of the best examples of a mix system in ferroelectric community is PZT. A mixture of anti-ferroelectric $PbZnO_3$ and ferroelectric $PbTiO_3$, where Zinc is substituted by lead. It's important to note that there is no restriction of compositional ratio, thus there is possibility to tune physical properties in a wide range. The particular composition of 50/50 has exceptional piezoelectric properties [29].

Perovskite are not only limited by single ions cations and anions. Recently, considerable attention has been paid to metal-organic systems. This means some or even all cations and anions can be replaced by organic counterparts. One of the most popular systems currently is methylammonium lead iodide ($CH_3NH_3PbI_3$) due to perspectives in solar cell industry [30]. In the position of A cation sits a CH_3NH_3 molecule. An example of even more complicated system could be given as dimethylammonium zinc formate $[(CH_3)_2NH_2]$ [Zn] $[(HCOO)_3]$, here each cation and anion is separated by square brackets.

A high verity in the family of perovskites lead to many different physical properties. Perovskites can be constructed like LEGO blocks and their properties can be tuned using different ions. As long as the charge neutrality and ion size conditions are satisfied. For instance, titanium ion placed in the B - site, tend to shift from the ideal central position. This is the cause of the

spontaneous polarization in $BaTiO_3$, $PbTiO_3$. Other drastically different properties like large thermal conductivity in $LaCoO_3$ [31], ferromagnetism in $SrRuO_3$ [32], semi-conductivity in $LaCrO_3$ [26] and anti-ferroelectricity in $PbZnO_3$ [14] can be observed in perovskites.

2.4 Broadband dielectric spectroscopy

In order to speak about dielectric spectroscopy, it's necessary to introduce the concept of dielectric permittivity. One of most popular descriptions of dielectric permittivity is the ability of at substance to hold electrical charge. This description doesn't offer a lot of information about the nature of dielectric permittivity. Dielectric permittivity can also be described as a property which defines the degree of electrical polarization a material experiences under the influence of external electrical field. This electrical polarization is related to reorientation of dipoles. It should be noted that dipoles have inertia thus not all dipoles can follow fast alternating electrical fields. This means at high frequency field's dielectric response or just dielectric permittivity values are much lower. For example, in the visible light range dielectric permittivity values are rarely higher than 3 - 4.

Dipoles based on the physical nature can be categorized in several groups: Maxwell - Wagner, dipolar, atomic and electronic polarization [33]. Maxwell – Wagner polarization is typically visible at the lowest frequencies ranges (10^{-5}-10^{4} Hz) of a dielectric spectra. This polarization can be described as a charge separation over a considerable distance in heterogeneous medium at the interfaces of two mediums having different dielectric permittivity or electrical conductivity values. Dipolar polarization (visible in 10^{2}-10^{11} Hz) is a polarization that usually arises from any polar molecules. Also, domain wall movement which is typical for ferroelectric materials can be assigned to this group. Further on the list is atomic polarization that appears from ion vibration. One can image a case of movement of ion in local potential minima. Often this type of polarization is called phonon polarization and normally visible in 10^{12} - 10^{15} Hz frequency range. And lastly, in the visible light frequency range (10^{14} - 10^{16} Hz) electronic polarization is observed. A phenomenon that occurs when high frequency electrical field distorts electrical cloud around positive atom nucleus, this creates a slight separation of charges opposite to the external electrical field. On the whole every process give a slight contribution to low frequency dielectric permittivity values [18]. A typical dielectric permittivity values at low frequencies (10^{3} Hz) for ferroelectric and non - ferroelectric materials are $\varepsilon \sim 10^{3}$ to 10^{4} and $\varepsilon \sim 10$ to 100, respectively.

In a frequency dependence graph Maxwell – Wagner or dipolar processes are visible as relaxations and atomic or electronic processes – as resonances.

Dielectric permittivity constant for resonance systems can be described by the following equation:

$$\varepsilon(\omega) = \varepsilon' - i\varepsilon'' = \varepsilon_\infty + \frac{\Delta\varepsilon\omega_0^2}{\omega_0^2 - \omega^2 + i\gamma\omega}. \quad (2.14)$$

Here ε' – real and ε'' – imaginary parts of dielectric permittivity. Real part of dielectric permittivity defines medium ability to interact with an external electrical field and imaginary part defines medium ability to dissipate or absorb electrical field (imaginary numbers are just for mathematical convenience). $\Delta\varepsilon$ – Is the contribution to dielectric permittivity value or dielectric strength of the process and ε_∞ – is the sum of all dielectric contributions of high frequency processes often referred as high frequency dielectric permittivity value. And lastly, ω_0 – is the angular resonance frequency, ω – angular frequency of external electrical field and γ – resonance damping factor [18].

Dielectric permittivity for simple relaxations for non-interactive dipole systems can be described by Debye law:

$$\varepsilon(\omega) = \varepsilon_\infty + \frac{\Delta\varepsilon}{1 + i\omega\tau}. \quad (2.15)$$

here τ – is the relaxation time of the dipoles. It should be pointed out that a resonance like dispersion can be seen as relaxation like dispersion if we have high γ damping factor. Thus, a diminishing resonance and a shift to the lower frequencies is observed (figure 2.6).

Usually more complicated systems with a distribution of relaxation times are investigated in those cases experimental data is approximated by Cole – Cole [34] law:

$$\varepsilon(\omega) = \varepsilon_\infty + \frac{\Delta\varepsilon}{1 + (i\omega\tau)^{1-\alpha}}. \quad (2.16)$$

Here α – is a parameter that describes the width of the distribution of relaxation times. In some cases this distribution of relaxation times is asymetrical then a more general Havriliak-Negami [35] law is used:

$$\varepsilon(\omega) = \varepsilon_\infty + \frac{\Delta\varepsilon}{(1 + (i\omega\tau)^{1-\alpha})^\beta}. \quad (2.17)$$

Here β is the parameter that defines the asymmetry of the distribution of relaxation times.

Further information about dipolar nature of the processes can be generally obtained from temperature dependence of relaxation times which usually follow Arrhenius law:

$$\tau = \tau_0 e^{-E_A/k_B T}. \quad (2.18)$$

Here τ_0 – is attempt time, k_B – Boltzmann constant, T – temperature, E_A – process activation energy which define potential barrier size for the process to occur. For more complicated systems when interaction between several dipoles is possible a dipole may stay in a frustrated state by interacting with several different orientation dipoles. Such materials are called dipolar glasses and can be model by Vogel-Fulcher-Tamman law [36]:

$$\tau = \tau_0 e^{-E_A/k_B(T-T_0)}. \quad (2.19)$$

Here T_0 – is dipole freeing temperature below which a reorientation of a dipole can no longer be thermally activated.

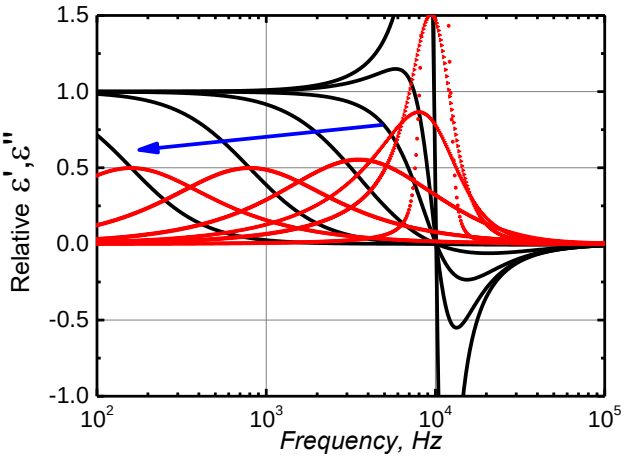

Figure 2.6 Frequency dependence of dielectric permittivity for resonance like dispersion. As damping factor grows the process tends to shift to lower frequencies and the resonance diminishes.

2.5 Lichtenecker model

Generally, combination of several materials will result in material with different dielectric properties. The difference is related to the structure of composite material. The simplest case is where put two crystals horizontally next to each other and call it a composite. The properties of such system will have linier relationship between the composition amounts. Of course, usually the situation is more complex and the end result of dielectric properties highly depends on distribution of electrical fields in separate composite parts. There are several models that can estimate dielectric properties if the structure is known such as core – shell [37] or brick layer [38] model. In our work the structure of the composite is not clear. Thus a different and more general model is used called Lichtenecker model [39], [40]. This model relies on a parameter β to describe the structure of the system. This parameter can be found using several different compositions with the same structure:

$$\varepsilon^{*\beta} = X\varepsilon_1^{\beta} + (1-X)\varepsilon_2^{\beta}, \quad -1 \le \beta \le 1. \tag{2.20}$$

here, ε^* – complex dielectric permittivity, X – volume fraction of one medium, ε_1, ε_2 – dielectric permittivity of medium one and two, respectively, and β – parameter describing the structure of the system if β = -1 the system

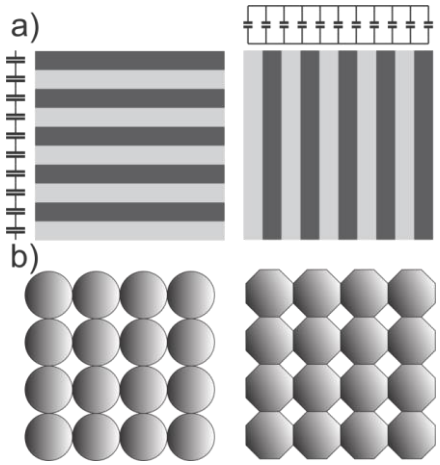

Figure 2.7 Schematic representation of Lichtenecker model, (a) represent boundary conditions of β parameter, (b) represent unbaked and baked ceramics, where baked ceramic has pillar like structure and is more similar to β = 1 condition.

is made of plates connected in series and if β = 1 – is made of parallel pillars (Figure 2.7). In should be noted that a low density composite system with baked grains has higher β coefficient than a system with unbaked grains. This is due to the fact that more interconnected grains represents parallel capacitor structure and unbacked grains represent parallel and capacitors in series equally. Furthermore in this model if β coefficient is higher than zero this means that all phases in the composite percolates [40].

2.6 Frustrated compounds

A frustrated state is a term that refers to a system where a dipole has two energetically equivalent opposite positions, up or down (Figure 2.8). The frustrated dipole cannot minimize its interactions with both simultaneously. This phenomenon is observed in materials called dipolar glasses and relaxor ferroelectrics. Both systems are very similar in their physical properties and often can be misinterpreted [41].

From a microscopic point relaxor ferroelectrics are compounds with

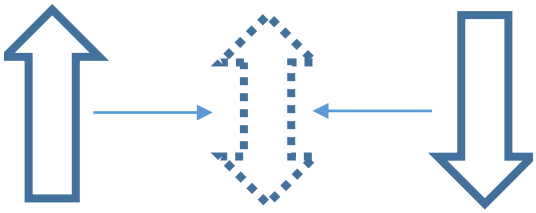

Figure 2.8 An example of frustrated dipole.

chemically disordered polar nano regions (PNRs). In the case of dipolar glasses, the frustrated states are between individual molecules. Although in some cases they may be some clustering but compared to PNRs, those regions are very small which are in the order of few lattice constants [41].

Macroscopic parameters for both systems are very similar. One of the main characteristics is that both systems experience collective freezing. This means at particular temperature all dipolar movements stop. Relaxations time of such phenomena can be approximated using Vogel Fulcher law (2.19). Also, for both systems relaxation width increases as the temperature decreases. Although there is a slight difference in the distribution of the relaxation times f(τ) [42], [43]. In the case of dipolar glasses only one maxima is visible, and in the case of relaxor ferroelectric at low temperatures a second maxima

can be visible which may be related to flipping a breathing modes of PNRs [44], [45]. Other similarities and differences can be seen in the temperature dependence of the complex dielectric permittivity. In both cases the maxima of the real part of dielectric permittivity shifts to the higher temperatures as the frequency increase, such phenomena in the older literature was called diffusive phase transition. However dielectric permittivity value for relaxor ferroelectric is usually a lot higher (values are about 10^3-10^4).

The main differences can be seen in the behaviour of the imaginary part. In the case of relaxor ferroelectric the curves of the imaginary part do not intersect each other and at the low temperature imaginary curves combine into one curve. In the case of the dipolar glasses imaginary part of dielectric permittivity show intersecting "half circles". One of the more reliable ways to distinguish relaxor ferroelectrics from dipolar glasses is polarization measurement experiment. At low fields in both cases a very thin nonlinear hysteresis loop is observed. However relaxor ferroelectric ground state is very close to ferroelectric state and at high fields ferroelectric state can be induced [46], [47]. Also, it should be noted that if the ferroelectric state is induced in the vicinity of the maxima of dielectric permittivity at low frequencies the ferroelectric state persists. Relaxor phenomena is usually observed in the chemically disorder systems like PMN ($Pb(Mg_{1/3}Nb_{2/3})O_3$) [48] and dipolar glasses state usually can be seen in system with highly interacting dipoles [49], [50].

2.7 Measurement techniques

In the thesis dielectric measurements were performed in a broad 10^2-10^{11} Hz frequency range. The temperature measurements were done in 100 – 500 K temperature range using Keithley Integra 2700 multimeter with 100 Ω platinum resistor or T type thermocouple sensors. Temperature was controlled with a DC power supply and a heater and low temperature were achieved using liquid nitrogen. Due to broad frequency measurement range several experimental setups were used to cover the whole range. A schematic representation of dielectric permittivity measurement equipment in the Laboratory of Microwave Spectroscopy is shown in figure 2.9. Further in this chapter experimental setups from lowest to highest frequencies will be discussed.

The lowest frequencies (20 Hz - 1 MHz) were measured using Hewlett Packard A4284 precision LCR meter. The experiment setup is shown in figure 2.10. Sample is placed between two parallel capacitor plates, then capacity and loss tangent is measured. Complex dielectric permittivity values can be extracted from flat capacitor model:

$$\varepsilon' = \frac{Cd}{\varepsilon_0 S}, \qquad \varepsilon'' = \varepsilon' tg(\delta). \tag{2.21}$$

Here C – is the capacitance, ε_0 – vacuum or free space dielectric permittivity

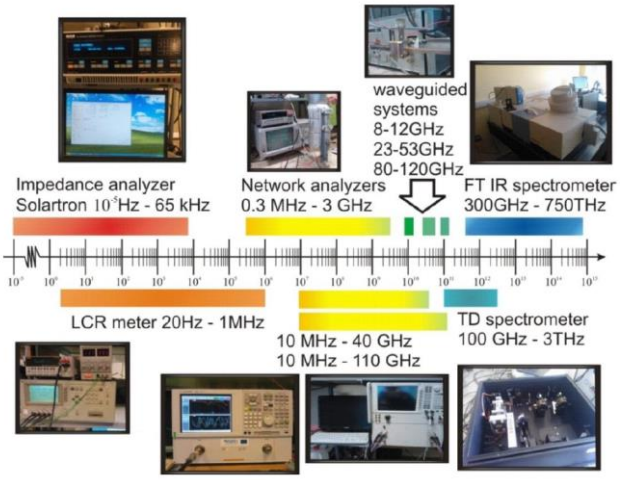

Figure 2.9 Dielectric measurement equipment in the Laboratory of Microwave Spectroscopy.

value, S – is the area of the sample, d – is the thickness of the sample and

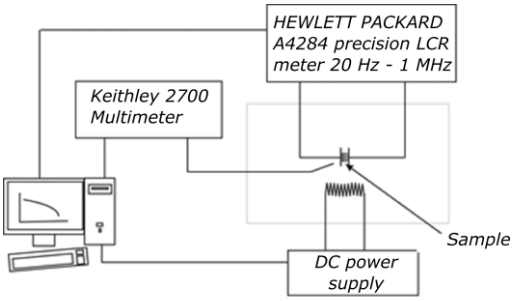

Figure 2.10 A schematic representation of a flat capacitance measurement setup.

$tg(\delta)$ is the loss tangent. During calibration process cryostat capacitance and loss tangent is subtracted from the measurement results.

At the higher frequencies (1 MHz - 3 GHz) a simple flat capacitance model is invalid as the cables in the measurement system have significant contribution to samples impedance values. Furthermore at even higher frequencies (above 100 MHz) a standing wave may arise thus failing impedance measurement completely [18], [51]. This can be avoided by taking into account the whole measurement line therefore a vector analyser is required (in our case Agilent 8714ET was used). Although the calibration of such system is more complicated and scattering matrix has to be obtained. This can be done by using three calibration loads: open coaxial line, a loaded coaxial line (in our case 50 Ω load) and short circuit coaxial line.

Further the measurement line is terminated by a flat capacitor (sample) and complex reflection coefficients is measured. The impedance can be calculated by the following formulas:

$$R^* = \frac{(Z^* - Z_0)}{(Z^* + z_0)}, \qquad z^* = \frac{1}{i\omega C^*}. \tag{2.22}$$

Here R^* – complex reflection coefficient, Z_0 – the impedance of the transmission line, in our case it is equal to 50 Ω. Z^* and C^* – complex impedance and capacitance of the sample, respectively. Additionally, dielectric permittivity can be calculated using a flat capacitor model. A schematic representation of coaxial line system is shown in figure 2.11.

It is important to stress that this model works well with relatively low dielectric permittivity samples as in those samples electrical field is homogeneous. With the increase of dielectric permittivity values the size of the wavelength of electromagnetic wave is similar to the specimen dimensions

thus a distribution of electric field in the sample becomes inhomogeneous. This means several different modes can be exited in the sample. This can be corrected using multi-mode capacitor model developed in our laboratory by Lapinskas [52].

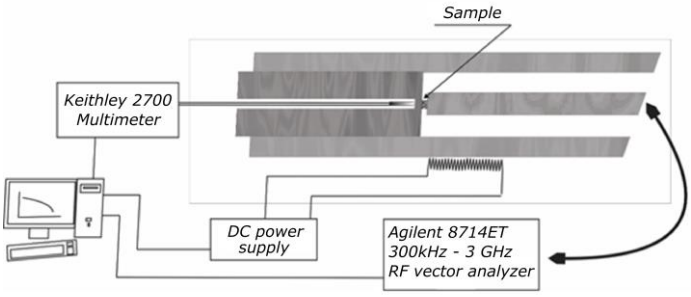

Figure 2.11 schematic representation of a coaxial line measurement setup.

The highest frequencies (8 GHz – 55 GHz) in this work were measured using waveguide systems (Figure 2.12). Waveguide measurements are time consuming as several different size rectangular waveguides are used (8 – 12 GHz, 24 – 40 GHz, 36 – 55 GHz) due to the requirement that only the main mode TE_{10} could propagate. A needle shape sample is placed in the middle of the waveguide system perpendicular to the wider wall where the electrical field of the main mode TE_{10} is the strongest. This way we can minimize or eliminated the effect of magnetic field.

The reflection and transmission coefficients are measured by Elmika R2400 scalar network analyser. Complex dielectric permittivity values can only be obtain by solving nonlinear equations [53]. Nevertheless, the exact expression for our case is unknown. Thus, a different (reversed) method is used. Dielectric permittivity is obtained by solving reflection and transmission optimisation problem:

$$\begin{cases} R = f_1(\varepsilon'\varepsilon'') \\ T = f_2(\varepsilon'\varepsilon'') \end{cases}. \tag{2.23}$$

Here R and T – reflection and transmission, respectively. The whole reflection and transmission expressions are quite overwhelming and can be found in [53]. Optimisation problem is solved by a program developed in microwave spectroscopy laboratory. This program is based on modified Newton optimization method.

In addition to dielectric measurements a ferroelectric and pyroelectric characterization was performed. Pyroelectric current was measuring using

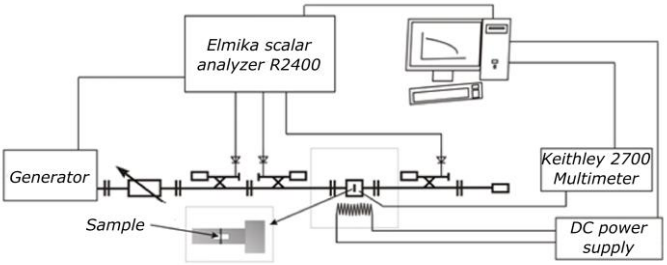

Figure 2.12 A schematic representation of a waveguide setup.

Keithley 6514 electrometer. The sample was poled with 300 V DC power supple. At the end of the cooling cycle specimen was short circuited with 10 kΩ resistor for 10 – 15 minutes. Then during a heating cycle with 3-5 K/min heating rate current measurement was performed. Polarization values were calculated using following formulas:

$$Q = \int_{t_0}^{t_{end}} I\, dt,\ P = \frac{Q}{S} \tag{2.24}$$

Here Q – charge, I – current, P – polarization, S – sample area, t – time, t_0 and t_{end} – start and end time of a measurement, respectively.

Ferroelectric measurements were performed with AixACCT TF2000 analyser with a DC power supply TREK 609E-6 which is capable of supplying voltage up to 4 kV. Polarization hysteresis measurements were performed with a triangular voltage signal of 111 Hz. The odd frequency was chosen to avoid any contribution from harmonic that could arrive from the power circuit. The polarization hysteresis curves can be calculated by following expression:

$$P = \int_{E_1}^{E_2} \frac{I}{S} \alpha\, dE,\ dt = \alpha dE \tag{2.25}$$

Here E – is electrical field in the sample, α – a coefficient that describes relationship of electric field and time during triangular signal.

Ultrasonic wave velocity and attenuation measurements were done at a frequency of 10 MHz in the temperature range 140–340 K by the automatic pulse-echo method. [54] The samples were placed between two ultrasonic waveguides lubricated with silicone oil to ensure acoustic contact for propagation of longitudinal waves between the sample and the waveguides. The thickness of the samples was 1–1.5 mm. Z-cut $LiNbO_3$ acoustic wave transducers placed at the end of the quartz buffers were used for transmitting

and receiving the longitudinal acoustic wave. The relative velocity and attenuation of the US longitudinal wave were calculated from the variation of the delay time and amplitude of transmitted radio frequency pulse after monitoring this pulse on the screen of a digital oscilloscope. Ultrasound measurements for $MAPbX_3$ (I, Br, Cl) system were performed under supervision of V. Samulionis and measurements for mix $MA_{1-x}DMA_xPbBr_3$ system were performed by M. Kinka.

The FTIR (Fourier Transform Infrared) measurements were performed with Bruker Vertex v80 spectrometer (30 – 3000 cm^{-1}) at room temperature in the reflection mode. The mercury lamp was used to generate FIR. The signal is separated into two identical signals with the beam-splitter, where one part reflects from the fixed calibrational mirror or from the polished sample, and other reflects from the moving mirror. Then the signal is collected on the detector where interferogram is formed. The FIR spectra is obtained by performing Fourier transformation on the interferogram. The spectrometer is controlled by OPUS program.

2.8 Sample preparation

Samples for this work were received from Japan, Poland and Germany. Samples from Japan, Satoshi Wada group, has a core – shell composite structure and includes pure barium titanate ($BaTiO_3$), several samples with barium titanate core and potassium niobate ($KNbO_3$) shell depicted as xKNBT and lastly two samples with barium titanate and bismuth ferrite ($BiFeO_3$) core and barium titanate shell. Furthermore, from Poland, Mirosław Mączka group, and Germany, Doru Lupascu group, we have received two different batches of methylammonium (MA) lead halides (I, Br, Cl). Also, Mirosław Mączka provided us with mix MA/dimethylammonium (DMA) lead halides samples. Specimens from Japan were in the form of ceramics and samples from Poland and Germany were in the form of crystals. The syntheses of the samples and the preparation of the specimens for dielectric measurements can be found in the following sections.

2.8.1 Core-shell BT/KN, BT/BT and BF/BT samples

In this study, BT, 0.22BTKN and 0.25BTKN (the number refers to KN/BT ($KNbO_3/BaTiO_3$) molar ratio) samples were prepared in the following steps. The tetragonal BT powders (particle size of approximately 300 nm, Sakai Chemical Industry) were used. The $BaTiO_3$ powders were mixed with ethanol

and an organic binder, poly(vinyl butyral) (the average polymerization degree of 1000, Wako Pure Chemical Industries) (2 wt% of $BaTiO_3$ powders), and dried at room temperature. The resultant powders were sieved and pressed into a green compact using a uniaxial press at 250 MPa. The binder was burned out at 600 °C for 10 h. To promote necking structure of $BaTiO_3$ particles (Figure 2.13), these compacts were sintered at 1000 °C for 2 h in air.

$BaTiO_3$ compacts with a necking structure were immersed in 5.2 M niobium pentaethoxide (Nb(OC2H5)5; 99.99%, Kojundo Chemical Laboratory) ethanol (EL grade, Kanto Chemical) solution in N_2 atmosphere. These compacts were then immersed in water at 20 °C for 6 h to facilitate hydrolysis and condensation of $Nb(OC_2H_5)_5$ and niobium hydroxide gels were formed inside the $BaTiO_3$ compacts. After drying at room temperature, the $BaTiO_3$ compacts with niobium hydroxide gels were heated at 600 °C for 5 h. the amount of the Nb source added to the $BaTiO_3$ compacts was controlled by the number of cycles of the immersion and the subsequent heating procedures. The resultant niobium oxide/BT compact was placed in a Teflon container

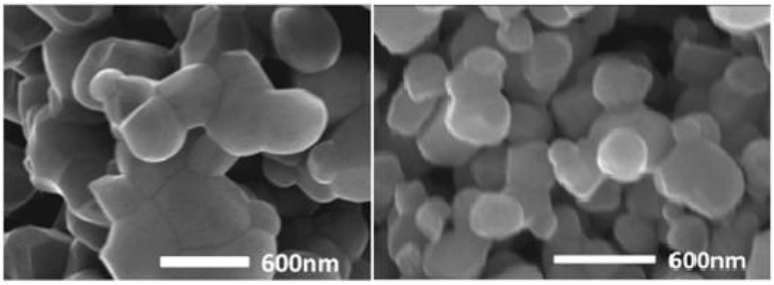

Figure 2.13 Scanning electron microscope image of necking $BaTiO_3$ structure provided by Satoshi Wada group.

filled with KOH (UGR grade, Kanoto Chemical) and K_2CO_3 (UGR grade, Rare Metallic) ethanolic solution (KOH/K2CO3=0.22, [K+]=1.0 M). The K/Nb atomic ratio was fixed to 10. Then, the solvothermal treatment was carried out at 230 °C for 20 h in an autoclave. After the solvothermal treatment, the compacts were washed with ethanol and dried at 200 °C for 5 h. The composition ratio of the obtained KN/BT complex ceramics was calculated based on mass changes due to the complete conversion reaction of Nb_2O_5 into KN. In this study, we prepared the KN/BT complex ceramics with the composition ratio of KN/BT=0.22 and KN/BT=0.25, which were obtained

by repeating for 3 and 5 cycles of the immersion and the subsequent heating procedures. Additional information can be found elsewhere [55], [56].

BT nanoparticles (particle size around 300 nm, Sakai Chemical Industry) or BF (synthesizedby a hydrothermal method) and TiO_2 were mixed using ball mill; then, anorganic binder poly(vinyl butyral) (2 wt%) was added. The mixture was compressed into cylindrical pellets with uniaxial press at 250 MPa pressure and dried at 600 C for BT and 400 C for BF temperature for 10 h. Further, disk-shape pellets were submerged into barium hydroxide ($Ba(OH)_2$, Ube Material Industries, >99.9%) solution at 175 C temperature for 18 h for solvothermal solidification (synthesis of the second BT phase). In the end we obtain BT – BT and BT – BF composites. Addition information about preparation and structure (XRD and TEM) can be found elsewhere [57], [58].

2.8.2 Methylammonium lead halide samples

Organolead trihalide perovskite samples, $CH_3NH_3PbX_3$ (X = Cl, Br, I), were synthesized in two steps according to the procedure reported by Im et al. [59] with small modifications. The precursors CH_3NH_3X were synthesized by the reaction of stoichiometric amounts of methylamine, CH_3-NH_2, solution (33 wt% in absolute ethanol, Sigma Aldrich) and the corresponding halogen acid, HBr (48 wt% in H2O), HI (57 wt% in H2O), or HCl (>37 wt% in H2O) (all Sigma Aldrich), under stirring in an ice bath for 3 h. The solvent was subsequently removed under vacuum in a rotary evaporator. The resulting salts were washed with absolute ethanol and absolute diethyl ether several times and finally dried in a vacuum oven at 60 °C for 12 h. In a second step, the synthesized salts CH_3NH_3X were mixed with PbX_2 (Sigma Aldrich) (X = Br, Cl) in molar ratios 1:1 in N,N-dimethylformamide (Acros Organics) at room temperature overnight. CH_3NH_3I was mixed with PbI_2 (Sigma Aldrich) in γ-butyrolactone (Extra Dry over Molecular Sieves, Acro Seal) at 60 °C overnight. After vacuum evaporation of the solvents, a mixture of crystallites was obtained. The crystallites are black for the iodide, orange for the bromide, and colorless for the chloride samples.

2.8.3 Mixed $MA_{1-x}DMA_xPbBr_3$ samples

Single crystals of $MA_{1-x}DMA_xPbBr_3$ were grown using antisolvent vapor-assisted crystallization, in which the appropriate antisolvent is slowly diffused into a solution containing the crystal precursors. In the typical synthesis, 2 mmol of hydrobromic acid was added to appropriate amounts of methanol solutions containing methylamine and dimethylamine (2 mmol). Then 3 mL of dimethyl sulfoxide (DMSO), 5 mL of acetonitrile and 2 mmol of $PbBr_2$ were added to the prepared amine hydrobromide solution under stirring. The clear solution obtained after 1 h was transferred into a glass vial and this vial was placed in a second larger glass vial containing methyl acetate. The lid of the outer vial was thoroughly sealed, but the lid of the inner vial was loosened to allow diffusion of the methyl acetate into the precursor solution. Orange crystals were harvested after 5 days, washed with acetonitrile and dried at room temperature.

2.8.4 $[(CH_3)_2NH_2][Zn][(HCOO)_3]$ samples

$ZnCl_2$ (99%, Fluka), 2.0 M solution of $(CH_3)_2NH$ in methanol (Sigma-Aldrich), methanol (99.8%, Sigma-Aldrich) and formic acid (98%, Fluka) were commercially available and used without further purification. Single crystals of DMAZn were obtained by a slow diffusion method. In a typical experiment, 16 mL methanol solution containing 12.8 mmol of $(CH_3)_2NH$ and 12.8 mmol of formic acid was placed at the bottom of a glass tube (9 mm inner diameter). 16 mL methanol solution containing 1.6 mmol of $ZnCl_2$ was gently added to this solution. The tube was sealed, and after 5 days colourless crystals were harvested.

3. Results and discussion

In this chapter broadband dielectric spectroscopy results in a frequency range of 10^{-2}-10^{11} Hz and 30-500 K temperature for perovskite systems will be presented. This work is mainly focus on structural phase transition and dipolar relaxation in mid-high frequency region. Result will be discussed in the order of the structure complexity, thus we will start our chapter with simple $BaTiO_3$ and $KNbO_3$ and end with $[(CH_3)_2NH_2][Zn][(HCOO)_3]$.

3.1 Core – shell BT/KN, BT/BT and BF/BT

Piezoelectric materials play an important role in our everyday electronic devices. $Pb(Zr_xTi_{1-x})O_3$ (PZT) is one of the most widely used piezoelectric materials due to its high dielectric and piezoelectric constant and ability to operate in a wide temperature range [60]. In last several decades no new cheap and viable compounds that can replace PZT were found. As a result, a lot of research on piezoelectric solid solutions such as NBT, KNN, BNT, BNT-BT, BZT – BCT [61]–[65] has been done. Yet, compared to PZT solid solutions, their dielectric and piezoelectric properties are still poor. As reported by others [66], [67] the nature of PZT exceptional properties is related to the morphotropic phase boundary (MBP). MPB is a structural phase transition due to change of chemical composition. In this region increase in piezoelectric properties is often observed. Current research on piezoelectric materials is focused on preparing systems with MPB. In this case both compositions must dissolve in each other in order to create a solid solution, and not all MPBs exhibit superior piezoelectric properties. However, a different approach can be used, which allows a much broader selection in compositions. It is possible to create similar conditions as in MPB by forming a bulk hetero-epitaxial interphase [55], [56]. In this chapter we show composite structure, where the „core" phase is stressed by the "shell" phase (a layer, deposited onto the structure formed by "core" material). Our study is focused on electrical properties of Barium titanate (BT) "core" and potassium niobate (KN) "shell" systems and similarly BT and bismuth ferrite (BF) "core" and BT shell.

3.1.1 Dielectric spectroscopy of BT/KN

Dielectric measurements of BT ($BaTiO_3$), 0.22BT/KN ($0.78BaTiO_3$ – $0.22KNbO_3$) and 0.25BT/KN ($0.75BaTiO_3$ – $0.25KNbO_3$) systems were performed. Temperature dependences of 0.22BT/KN and 0.25BT/KN at different frequencies are shown in figure 3.1 [1]. Here, 3 anomalies are observed; those anomalies coincide with phase transitions in barium titanate at temperatures of 203 K, 278 K and 393 K [11]. However, the same results show no sign of potassium niobate (KN) phase transitions at temperature 263 K and 481 K, although infrared measurements showed evidence of KN phase.

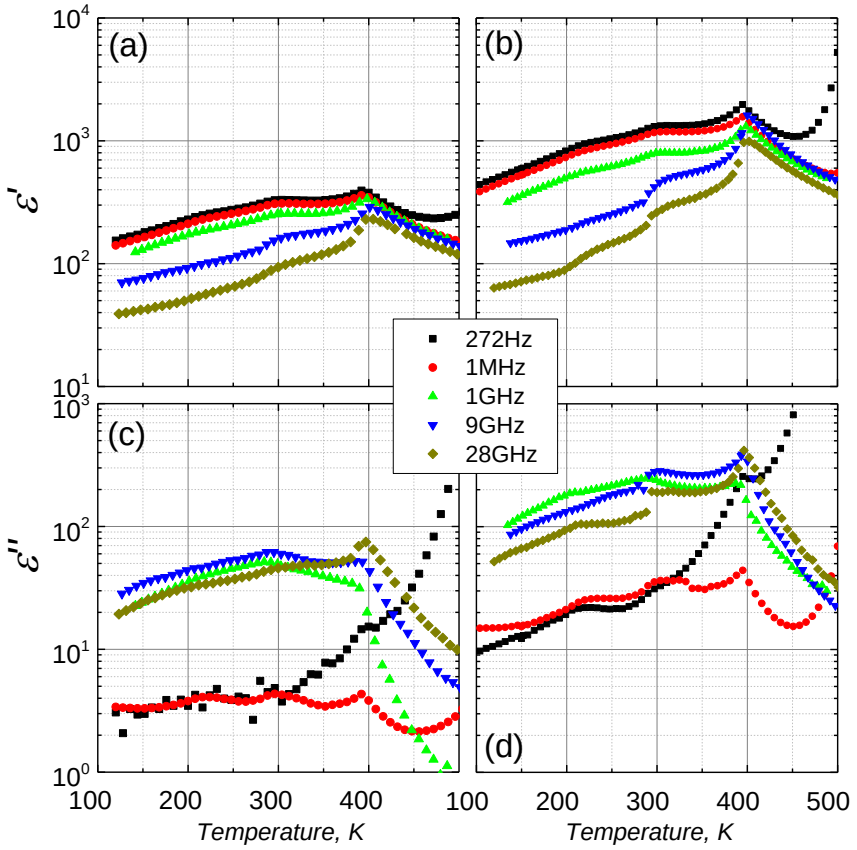

Figure 3.1 Temperature dependence of the real (a and b) and imaginary (c and d) parts of dielectric permittivity for composites 0.22BT/KN [1] (left) and 0.25BT/KN (right).

This can be seen in figure 3.2. The red curve represents pure barium titanate (BT) samples. The frequencies of all phonon modes coincide well with works published earlier [68]. The black curve shows one additional phonon mode which represents KN phonon mode at 430 cm^{-1} [69]. Small gradual reflection intensity decrease at higher frequencies is due to the porosity of the samples.

There could be several reasons why we have low contribution to dielectric

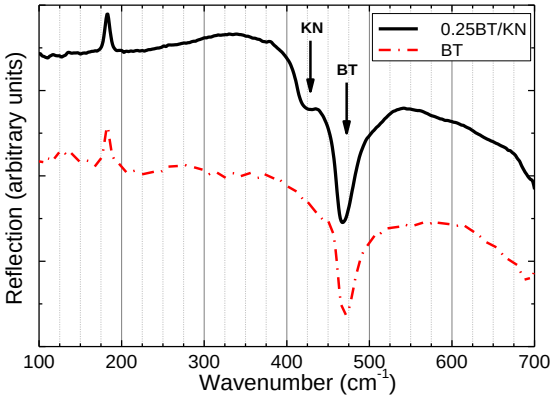

Figure 3.2 Infrared reflection spectra for 0.25BT/KN and BT at room temperature.

permittivity from KN phase. First of all, KN phase could have a high concentration of defects as it was sintered during solvothermal reaction [57]; secondly, KN crystallite sizes are around 50 nm and considering the size effect, dielectric permittivity should be very low [70]. Thus, the phase transitions might be screened by extrinsic effects.

Furthermore, frequency dependences of complex dielectric permittivity show one clear relaxation which was approximated using Cole – Cole law. Relaxation times for 0.22BT/KN and 0.25BT/KN are 30±12 ps and 60±14 ps respectively (Figure 3.3) [1]. This relaxation gives the main contribution to dielectric permittivity. The fact that this relaxation time hardly depends on temperature strongly suggest that the nature is related to acoustic resonance. In short: as ferroelectric domain wall moves, it emits Barkhausen acoustic noise [71], which can resonate in the grain or in a grain cluster; as BT is piezoelectric, the response can be seen in dielectric spectra. Alternatively, a uniformly polarized grain can contribute to the dielectric permittivity via the electromechanical coupling, with contribution determined by the characteristics of the acoustic resonance of the whole grain. This also explains

the slight difference in relaxations times as the grain clusters for 0.22BT/KN are smaller and the resonance frequency is higher than in 0.25BT/KN (Figure 2.13 left picture show the structure of BT for 0.25BT/KN and right one – for 0.22BT/KN.) .

Assuming the electromechanical mechanism, it is possible to calculate acoustic wavelength from the experimental data:

$$2d = \lambda = \frac{V}{f} \rightarrow d = \frac{V}{2f}. \qquad (3.1)$$

Here d – cluster average diameter, f – frequency, λ and f - acoustic wave length and speed, respectively. It is reported that velocity of acoustic waves in BT is around 5.5 km/s [72], [73]. Calculated half wavelength is 1030±200 nm which is in a good agreement with BT cluster size in 0.25KNBT system.

Interestingly, this contribution disappears at temperatures above the Curie point, as can be seen from figure 3.1 (only relaxation due to Maxwell-Wagner polarisation remains above 400 K). The same happens with the broad relaxation in frequencies of 10^3-10^6 Hz. This could indicate that the source of the latter relaxation is domain wall motion in BT grains. Similar measurements were done with core shell samples where BT was replaced with

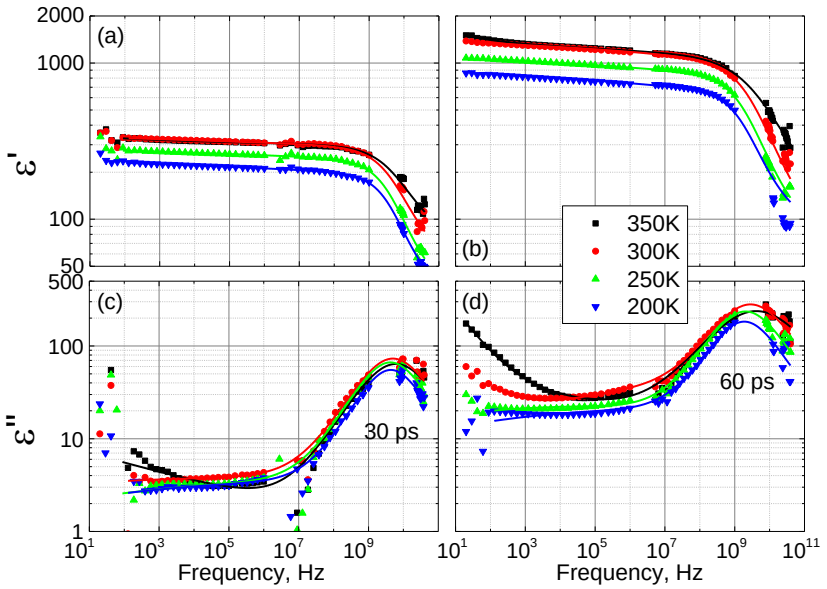

Figure 3.3 Frequency dependence of the real (a and b) and imaginary (c and d) parts of dielectric permittivity for composites 0.22BT/KN [1] (left) and 0.25BT/KN (right)

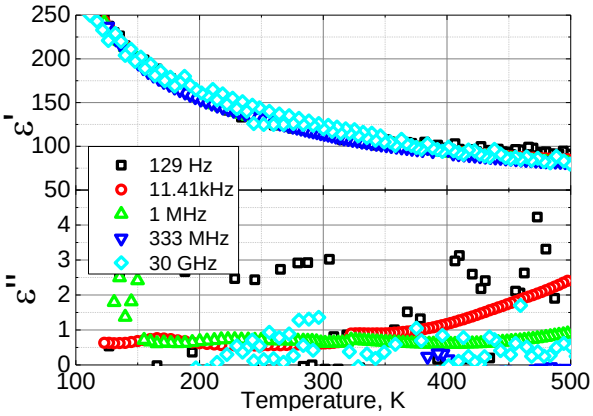

Figure 3.4 Temperature dependences of real (a) and imaginary (b) parts of dielectric permittivity for ST/KN sample.

ST ($SrTiO_3$) (Figure 3.4). It was observed that all temperature dependences of the real part of the dielectric permittivity are on the same curve. Thus dielectric data showed no dispersions up to 30 GHz. This further supports our idea of electromechanical origin of this microwave process, which is observed in BT/KN composites.

Moreover, BT and 0.25BT/KN composites have similar dielectric permittivity, although the densities are quite different (BT 59.53% and 0.25KNBT 78.67%). This fact further supports our assumption, that KN gives almost no contribution to dielectric permittivity, as the core structure of 0.25BT/KN was similar to the pure BT pellet. The main difference between experimental data is higher conductivity for 0.25BT/KN system at high (above 450K) temperatures which could be due to defects in KN structure. Also, significantly lower dielectric permittivity was observed in 0.22KNBT system, which cannot be explained by lower density or low KN contribution (figure 3.5).

It is important to note 0.22BT/KN and 0.25BT/KN have different BT topology (Figure 2.13). 0.22KNBT composite has a necking connection between grains, and composite 0.25KNBT grains are merged into bigger clusters. Lower dielectric permittivity can be explained using effective medium approach, i.e. Lichtenecker model [39], [40] In a system 0.22KNBT and 0.25KNBT both phases percolate, this means $0 < \beta$ [40]. Also, longer calcination time results in systems with larger interconnections between grains and represent more pillar like structure than a necking system, this means

parameter β is higher for 0.25KNBT than for 0.22KNBT. It can be mathematically shown that for smaller β values lower dielectric permittivity phase becomes more dominant.

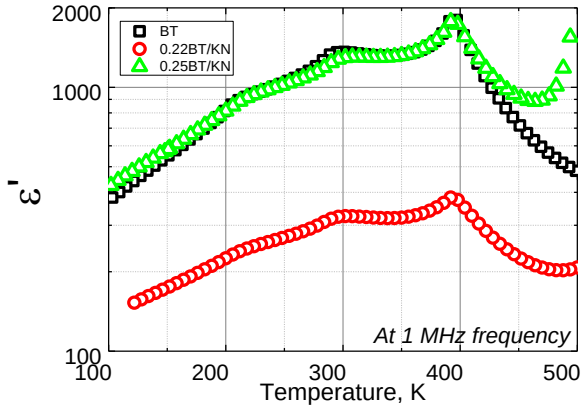

Figure 3.5 Temperature dependence of the real part of dielectric permittivity for BT, 0.22KNBT [1] and 0.25KNBT at 1MHz frequency.

3.1.2 Polarization of BT/KN system

The acoustic resonance causes a change in polarization, which gives a rise in dielectric permittivity. Arlt has calculated the relationship between spontaneous polarization and contribution to dielectric permittivity in the presence of ferro-elastic domains with the following equation [74]:

$$\Delta\varepsilon_r = \frac{P_0^2}{2C_{55}\varepsilon_0 S_0^2}, \quad f_c = \frac{\sqrt{C_{55}/\rho}}{\pi d} \tag{3.2}$$

here, P_0– spontaneous polarization, C_{55} – (shear) elastic constant, ε_0 – vacuum dielectric constant S_0 – spontaneous deformation, ρ – density, f_c – mean relaxation frequency. Effective contribution to dielectric permittivity Δε was obtained from Cole – Cole approximations (Figure 3.3). To obtain real dielectric permittivity $\Delta\varepsilon_r$ values (in our case due to low density dielectric permittivty of pure BT is lower) from the experimental effective ones, we applied Lichtenecker model, with β = 0.4 [75]. It is worth noting that the permittivity ε_1 ($\Delta\varepsilon_r = \varepsilon_1$) of the first phase (BT) is a lot higher than that of the second (Air or composite of air and KN). In this case we can assume that dielectric permittivity of the second phase is infinitesimal and can be neglected:

$$\varepsilon_1 = \left(\frac{\varepsilon^{*\beta} - (1-X)\varepsilon_2^{\beta}}{X}\right)^{\frac{1}{\beta}} \cong \frac{\varepsilon^{*\beta}}{X^{1/\beta}} \tag{3.3}$$

The obtained evaluation of the real permittivity of the core material allows us to apply eq. (3.3). In our work we replace elastic constant C_{55} with more general Young modulus as in case we have homogeneous ceramic and resonance occur in grain clusters which are randomly orientated. Temperature dependence of Young modules was taken from [76]. Electrostriction coefficient Q taken from [77], [78] and spontaneous deformation can be written as $S_0 = P_0^2 Q$ [74]. Using Arlt's model [74] we have managed to obtain spontaneous polarization temperature dependence curve that is similar to experimental curve found in literature [79] (Figure 3.6).

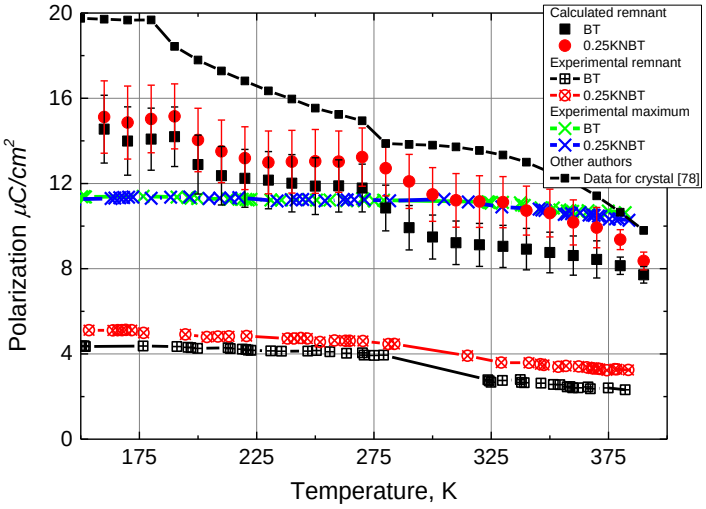

Figure 3.6 Calculated and measured spontaneous polarization values for BT and 0.25BT/KN systems. The error bars for measured systems are smaller than experimental points.

However, in our case calculations were based on ceramic measurements and due to random rotation orientation of grains, the calculated polarization should be around two times lower than in crystals:

$$\langle P \rangle = 2\int_0^{\pi/2}\int_0^{2\pi} \frac{P_0}{4\pi} sin\theta cos\theta d\varphi d\theta = \int_0^{2\pi} P_0 sin\theta ds in\theta = \frac{P_0}{2}. \tag{3.4}$$

It is reported that at room temperature pure, high quality BT crystals have polarization values up to 26-27 μC/cm^2 [74], [80], [81], which is still higher than what was obtained here by around 15-30 % (the double value of the obtained polarization at room temperature is 19 – 23 μC/cm2).

In order to verify our calculations, hysteresis loops measurements were performed in vacuum (pressure $<10^{-4}$ hPa) with 100 kV/cm field for 0.25KNBT and BT systems (Figure 3.7), which possess the same structure of the core material. Both structures show similar saturation polarization values at room temperature which are around 11.3μC/cm^2. Also slim hysteresis loops with high back switching is observed which is typical for fine grain ceramics

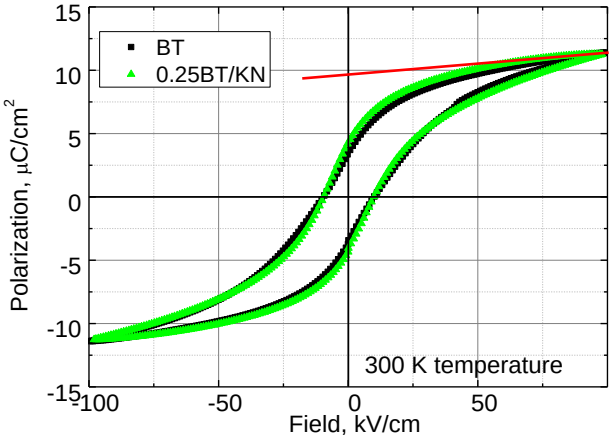

Figure 3.7 Dielectric hysteresis for pure BT and 0.25BT/KN structures at 300 K temperature.

[82], [83]. Alternative high back switching could occur due to large amount of defects [57]. Furthermore, we observed that samples with KN have higher remnant polarization value which are around 4.4μC/cm^2 and values for pure BT – 3.2μC/cm^2.

Furthermore, P(E) measurements showed high coercive field up to 10 kV/cm, this suggests about high number of deep defects in BT structure, which may pin the domain walls. This could explain different results obtained from calculation and P(E) measurements. Dielectric measurements are done with a small amplitude signals, this means domain wall moves just slightly and if the domain wall is pinned at one-point, other points of the wall can still move. We can image domain wall as membrane. The mobile sections of the domain walls have small chance to move far enough to encounter a new pinning defect. On the other hand for P(E) measurements high fields are applied, in this case domain walls has to move huge distances; and if a domain wall is pinned, deep defects forces domain wall to move back after removal of electrical field, resulting in low apparent remnant polarization [83]. In such case very large fields, which are enough to unpin domain walls are needed to estimate the true

spontaneous polarization. Thus, the indirect method to estimate the switchable polarization based on dielectric spectroscopy has and advantage of being less sensitive to pinning defects.

In addition, we observe higher spontaneous polarization values for 0.25BT/KN system in both cases. There could be several explanations. First of all, our calculation shows lower polarization value than found in literature; this could mean that there are some domains wall that can't move at all, for instance domain wall can be fixed to BT grain boundary surface. If we deposit a film of KN on BT grain we decrease surface tension on BT grains; also, KN could remove absorbed matter on BT. All in all, we change grain boundary condition on the BT surface and some domain walls could be unpinned. This theory works for results obtained from P(E) measurements as remnant polarization is increased by a fixed amount in all temperature range. Although for calculated polarization results, it is observed that spontaneous polarization of 0.25BT/KN at temperatures up to 278 K is equal to that of BT in the margin of error, but above that temperature spontaneous polarization of 0.25BT/KN is higher. At 278 K temperature a phase transition, from orthorhombic (lower temperature phase) to tetragonal, occurs in pure BT. Thus the second explanation could follow: epitaxial KN on BT surface stresses BT microscopic structure (especially in tetragonal phase), leading to increase in domain wall count and spontaneous polarization, similarly as in systems with morphotropic phase boundary [56]. Possibly, the third explanation should be considered: according to [84], enhanced non-180° switching was observed in the KN-BT composites, which could be the reason to easy movement of the domain walls in low signal regime. Thus, we obtain higher contribution to dielectric permittivity and from equation (3.2) – higher switchable spontaneous polarization. This explanation seems favorable also due to the fact that at high fields' polarization is the same in both 0.25BT/KN and pure BT, meaning that the value of the spontaneous polarization has not changed. Interestingly, the high-field value is very similar to what was obtained from dielectric data, so the estimate is correct. However, the KN shell improves mobility of the domain walls, which should lead to an enhanced electromechanical response. This, in a sense, is the artificial MPB.

3.1.3 Dielectric spectroscopy of BT/BT and BF/BT

Temperature dependence of the dielectric permittivity of BT-BT is displayed in figure 3.8 (a and c) [3]. As in previous BT/KN system three anomalies are observed at temperatures of 199 K, 287 K and 400 K that coincide with classical phase transitions in BT [11]. Still, it is worth noting that the value of dielectric permittivity is a few times lower than the previously reported values of dense BT ceramics with 300 nm grains size [85]. Although the densities are similar, the lower dielectric permittivity, as it was reported in [86], could be due to high concentration of defects in BT obtained by solvothermal reaction method. Another reason could be related to the fact that

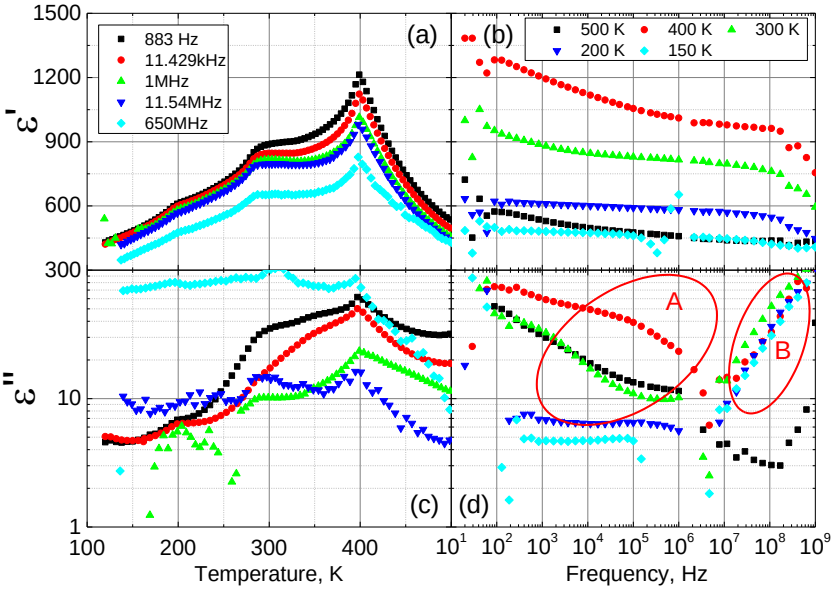

Figure 3.8. Temperature (left) and frequency (right) dependence of the real (a and b) and imaginary (c and d) parts of dielectric permittivity for BT/BT core-shell composite [3].

the crystallite sizes obtained in solvothermal reaction are a lot smaller than 300 nm (less than 100 nm) which would reduce dielectric permittivity due to size effect [87], [88]. At those sizes phase transition become obscured and hardly visible [89]. For smaller grains we can expect (extrapolate) that dielectric permittivity will be even lower as relative volume of grain shell increases.

Furthermore, two relaxations can be found in BT/BT composite (Figure 3.8 b and d). Low frequency relaxation (region A) could be due to domain wall movement as it disappears at temperatures above Curie temperature T_C = 400 K. Second relaxation (region B) similarly as BT/KN has electromechanical nature. Even though we observe only a tail part, it can be observed, that the high frequency relaxation does not depend on temperature. It means that the relaxation is influenced by mechanical properties of our sample. It is assumed that the main contribution to dielectric permittivity comes from 300 nm BT grains, and a relaxation at 10-20 GHz range should be visible (the fundamental mode would correspond to $\lambda/2$ resonator). Furthermore, as was noted in chapter 2.4 resonance dispersion can exhibit relaxation-like shape if we have a broad distribution of resonance frequencies, or if the oscillator is strongly over-damped. Similar resonances were visible in earlier works [1], [90]. Unexpectedly, the high frequency relaxation is still visible above phase transition at temperature above 400 K, but the strength of the relaxation is decreasing as the temperature increases. The explanation could follow that phase transition in different grains could occur at different temperatures due to surface effects. Similarly, it was recently reported in [91] that second harmonic was generated in barium titanate ceramics above Curie point, means absence of inversion symmetry.

Temperature dependence of BF/BT dielectric permittivity is displayed in figure 3.9 [3]. The first thing we notice is the absence of anomalies due to barium titanate phase transitions. As it was mentioned earlier, barium titante crystallites obtain by solvothermal reaction are around 50 nm. At those crystallite sizes the barium titanate phase transition are highly obscured and barely visible [89]. Nonetheless, the values of dielectric permittivity are similar at room temperature with conventional dense BF ceramics [92]. It is important to mention that BF/BT density is significantly lower in our case (BT – BF 70 % vs. BF 90% density in [92]). On the one hand, we should have lower values of dielectric permittivity due to lower density; on the other hand the values could have increased due to BT, which has higher dielectric constant; alternatively, from the HR-TEM shown in [93] we observe epitaxial BT grown on BF grains, thus dielectric properties could be increased due to stressed BF surface, similarly as in MPB compounds. Also, at temperatures below 300 K glassy behaviour is observed in BF/BT composite, which could be attributed to structural disorder, which is usually inherent to cold-pressed powders [94]. And lastly it is worth to mention that BF/BT has stable values of dielectric permittivity in broad temperature region and relatively high

dielectric permittivity values at high frequencies, which are great properties for microwave applications.

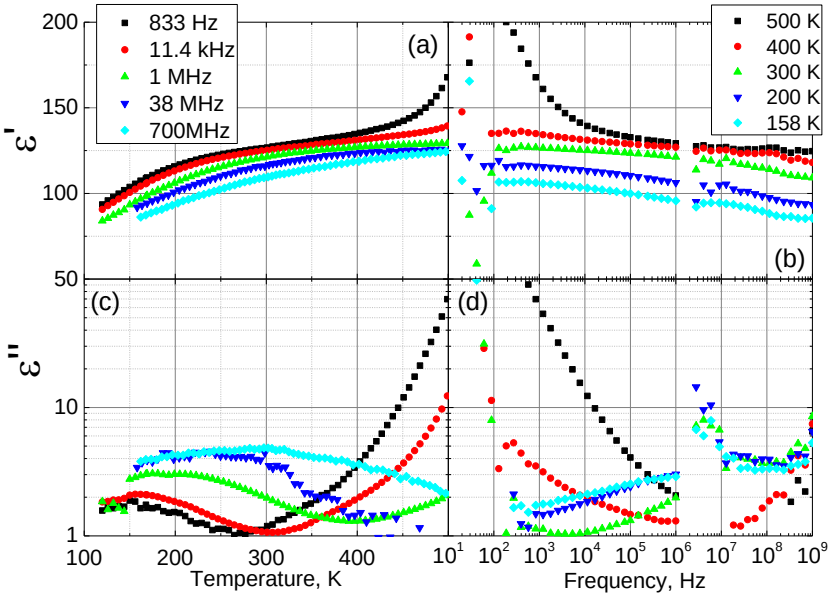

Figure 3.9. Temperature (left) and frequency (right) dependence of the real (a and b) and imaginary (c and d) parts of dielectric permittivity for BF/BT core-shell composite [3].

3.1.4 Summary

Based on the dielectric spectroscopy results in BT/KN system, it can be concluded that the main contribution to dielectric permittivity in microwave region comes from electro – mechanical resonance in BT clusters. Lower dielectric permittivity values in 0.22BT/KN system were observed due to different BT structure topology. Thus, controlling BT structure sizes and topology in the sample during preparation stage allows us to tune dielectric response of our system. Also, the same results show almost no contribution to dielectric permittivity values from KN in 0.25BT/KN composite.

Further, remnant polarization values for 0.25BT/KN composite are higher than for pure BT. Several reasons could follow. Firstly, KN on BT grains reduces surface tension or absorbed matter and reduces deep defect count which allows easier domain wall movement. Secondly, KN stresses BT microscopic structure, thus increasing domain wall count similarly as at the

morphotropic phase boundary. Even though the first explanation cannot be excluded, it is not sufficient. Thus, the second mechanism is needed to explain some of the observed experimental results. This can be considered an indication of an artificial MPB.

And lastly, we have measured dielectric properties of BT/ BT and BF/BT composites. In the case of BT/BT, frequency dependences showed two relaxations, which are due to domain wall motion (low frequencies) and electro-mechanical resonance in BT grains. Further, we have measured lower dielectric permittivity values in BT/BT due to defects and size effect in the solvothermally-derived phase. Lastly, BF/BT exhibited large values of dielectric permittivity, which can be explained by addition of BT to the BF structure, or, alternatively, due to stressed BF structure at hetero – epitaxial BF/BT interfaces. Furthermore, we have observed a glassy behaviour at temperatures below 300K.

3.2 Methylammonium Lead Halides (I, Br, Cl)

Hybrid perovskites in the recent decade attracted overwhelming attention due to their high photovoltaic performance yielding power conversion efficiency (PCE) of 21.9% [95]–[98]. The high solar cell performance was related to properties like: the exceptionally large diffusion length [99]–[101], long charge carrier lifetime [102], [103], high carrier motility [104], [105], large absorption coefficient [106], [107], and direct band gap [108] [109]. Methylammonium lead halides crystals, $CH_3NH_3PbX_3$, are the forerunners in solar cell industry.

$MAPbI_3$ undergoes cubic (P m3m) to tetragonal (P 4/mmm) and tetragonal to orthorhombic (P 222_1) phase transitions at 327 and 162 K, respectively. [110] Similar transitions from the cubic (P m3m) to tetragonal (I4/mcm) at 236 K temperature, and to the orthorhombic phase (P na21 [111] or P nma [112]) at 149 K are observed in $MAPbBr_3$ system. It is important to note that an intermediate phase between 154 and 149 K was reported, being either tetragonal P4/mmm [110] or incommensurate phase [113]. In the case of $MAPbCl_3$ a phase transitions at 179 K and 173 K from cubic (P m3m [110]) to tetragonal (P 4/mmm [110]) to orthorhombic (P nma [114]) phases are reported. The crystal phases were checked and confirmed by X-ray diffraction (XRD) and differential scanning calorimetry (DSC) Doru Lupascu group [2]. The sequence of phase transitions in $MAPbX_3$ has been suggested to be due to a consecutive removal of the disorder of the MA+ ions [115] which is still

discussed [116]. It is supposed to yield ferroelectric order at room temperature already [117], [118]. It was stated that ferroelectricity is the main reason for enhanced performance of solar cells using $MAPbI_3$ absorber [119], [120]. It was speculated that ferroelectric domain walls can act as p–n junctions separation of photoexcited electron–hole pairs thus reducing recombination of charge carriers [120]. Information about ordering of polar MA molecule and dipolar dynamics near phase transition can be obtained from dielectric spectroscopy measurements across wide frequency and temperature ranges, sadly only limited experimental data exist. Low frequencies up 1 MHz were measured by ONODA-Yamamumo et al., although dielectric dispersion related to dipoles was not observed [121]. At lower frequencies it was reported that dielectric permittivity increases due to ionic transport of halide anions [122]–[124] and charge separation at grain boundaries [125]. Poglitch and Weber [110] showed dielectric measurement for several frequencies in gigahertz range and Lin et al. [123] reported measurements in optical range. Yet, the frequency range (1MHz – 100GHz) where dipolar dispersion should be observed was not unexplored. In this chapter we will address the key role of the MA dipoles. We will show that a relatively high dielectric permittivity values exist across a wide 10^2 - 10^{11} Hz frequency range. Also we will show that the nature of high performance of $MAPbX_3$ solar cells are not due to ferroelectric domains as $MAPbX_3$ is not ferroelectric [2], [4].

3.2.1 Dielectric spectroscopy of $MAPbX_3$ (I, Br, Cl)

Temperature dependences of dielectric permittivity on cooling and heating cycles at 1 MHz for $MAPbI_3$ and $MAPbBr_3$ crystals and $MAPbCl_3$ polycrystalline are shown in Figure 3.10. A temperature hysteresis of 8 K, 7 K and 9 K is observed in I, Br are Cl compounds, respectively. During cooling cycle dielectric permittivity maxima arise at 148 K for $MAPbBr_3$, at 162 K for $MAPbI_3$, and lastly at 176 for $MAPBCl_3$. The maximums are related to tetragonal - orthorhombic phase transition for $MAPbI_3$ and $MAPbBr_3$, and to the cubic – tetragonal phase for $MAPbCl_3$. Furthermore, the crystalline compound $MAPbCl_3$ exhibits another anomaly at 168 k temperature, which can be associated with tetragonal - orthorhombic phase transition. Moreover, dielectric anomalies due to phase transitions between cubic and tetragonal phases for $MAPbI_3$ (At 327 K) and $MAPbBr_3$ (At 236 K) are not observed. It

is important to note that during ferroelectric phase transition a huge dielectric anomaly is usually seen [17], [18].

Additionally, dielectric permittivity in frequency range of 20MHz to 30 GHz was measured (Figure 3.11 (a)). It is observed that by increasing frequency the maxima of the real part of dielectric permittivity broadens and shift to the higher temperature range likewise the imaginary part increases and broadens. This suggest about a strong dipole related relaxation. Frequency dependences of dielectric permittivity were approximated using Cole – Cole (2.16) model (figure 3.11 (b)). Temperature dependences of the relaxation strength $\Delta\varepsilon$, the width of the relaxation α and high frequency dielectric permittivity ε_∞ are shown in figure 3.12 (a,b and c). It is observed that relaxation is getting stronger in the vicinity of the phase transition. Further

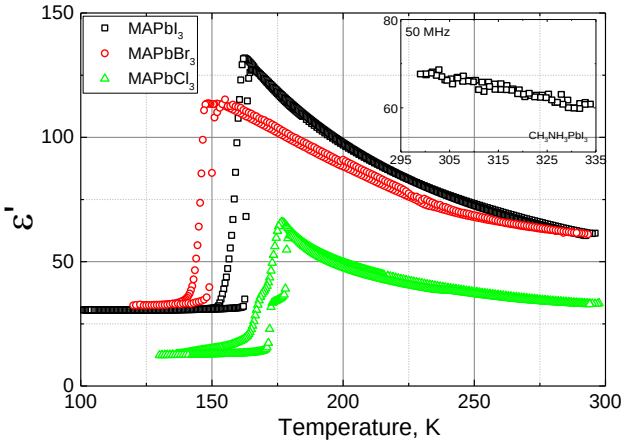

Figure 3.10. Temperature dependence of real part of dielectric permittivity for $MAPbI_3$ and $MAPbBr_3$ crystals and $MAPbCl_3$ polycrystalline [2].

from the alfa parameter it is possible to tell that the relaxation is very narrow and broadens in the vicinity of the phase transition. Also it can be seen that relaxation times increases and after the phase transition decreases (Figure 3.12 e, f and g), such phenomena is called critical slowing down. All of the above is typical features of the order - disorder phase transition [7].

Usually during a phase transition a softening of the elastic constant C [126] from the high temperature side is observed. Elastic constant is highly dependent on acoustic velocity v and attenuation α_{us}:

$$v^2 = \frac{1}{\rho} Re(C^*) \tag{3.5}$$

$$\alpha_{us} = \frac{1}{2\rho v^3} \omega Im(C^*) \tag{3.6}$$

Here, ρ – is the density and ω – angular frequency. Thus, with the supervision of V. Samulionis ultrasonic velocity and attenuation was measured (Figure

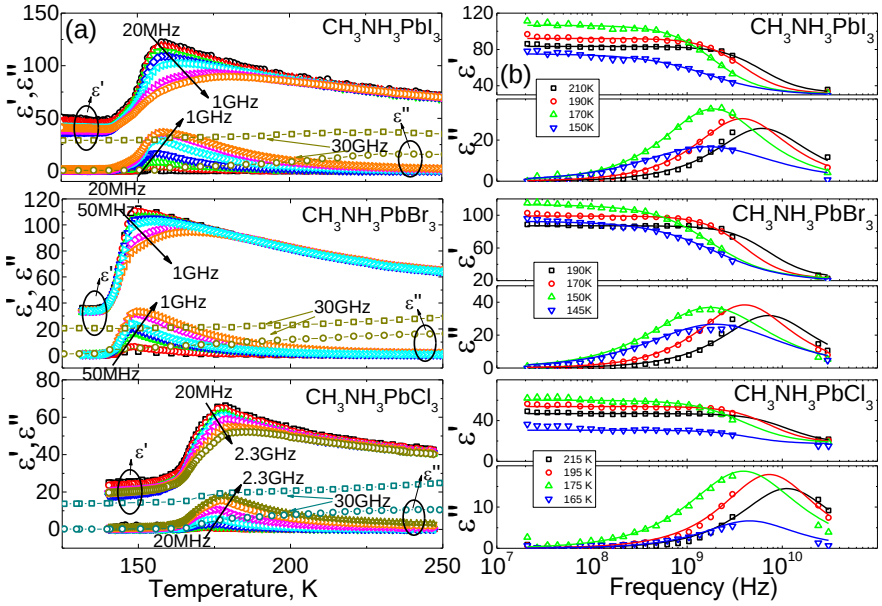

Figure 3.11 Temperature (a) and frequency (b) dependence of real and imaginary parts of dielectric permittivity for $MAPbI_3$ and $MAPbBr_3$ crystals, and $MAPbCl_3$ polycrystalline [2].

3.13). Similarly, as in dielectric results a step like acoustic anomalies at temperatures of 160 K and 148 K are observed in $MAPbI_3$ and $MAPbBr_3$ respectively. In the case of $MAPbCl_3$ polycrystalline two anomalies at temperatures of 179 K and 171 k were obtained. It should be noted that a slightly thinner temperature hysteresis of 2-5 K was observer in all three compounds.

Notable, in contrast to the results of the dielectric measurements the ultrasound velocity does show a clear minimum corresponding to the high temperature cubic to tetragonal phase transition at temperatures of 329 and 236 K for both $MAPbI_3$ and $MAPbBr_3$ crystals, respectively. Similar softening of elastic constants of $MAPbBr_3$ single crystal at the cubic to tetragonal phase

transition was reported by A. Letoublon et al. in the Brillouin scattering experiment [127]. Also overall softness of the system has been reported in static mechanical tests [128].

The main relaxation seen in dielectric spectra (Figure 3.11) is related to orientation of electrical dipoles under applied electrical field. The dipole moments in $MAPbX_3$ compounds are carried out by a MA^+ molecule. To match the overall cubic crystalline symmetry, orientation disorder of MA dipolar cations is required. The C-N bond of the MA cation was calculated by Jong et al. [129] to lie along <110> direction in order to satisfy the – 12 fold coordination of the lattice site. Another degree of disorder can be introduced by the possibility for MA molecule to rotate around its C-N axis. According to nuclear magnetic resonance results, the reorientation of C-N axis and rotation around this axis have activation energies of 120 and 50 meV, respectively [130]. The values of activation energy for $MAPbI_3$, $MAPbBr_3$ $MAPbCl_3$ obtained from dielectric spectroscopy data by applying Arrhenius law on relaxation times of dipolar relaxation are 100 meV, 79 meV and 75 meV, respectively. The obtained values are in between, therefore, we assume that both, reorientation of dipole moments and rotation around the C-N axis, contribute to the dynamics.

It was suggested that the sequence of phase transitions in $MAPbX_3$ corresponds to a progressive removal of certain degrees of freedom [110], [115]. According to ref. [115] the cubic to tetragonal phase transition is due to removing rotational disorder, while the orientation disorder is preserved, so the low-temperature phase remains non-polar. Partially lost orientation disorder, namely, polar or antipolar orders, has been discussed [131]–[133] allowing for a ferroelectric state in the case of polar order. This contradicts the centrosymmetric nature of the I4/mmm space group. A comparison between the values of the activation energy for the dielectric relaxation and the results of NMR measurements [130] indicates the plausibility of the model by Onoda-Yamamuro. Both reorientation of the dipole moments and rotation around the C-N axis contribute to the dielectric response in the paraelectric phase of $MAPbCl_3$, while only reorientation of the dipole moments happens in tetragonal $MAPbI_3$.

The transition into either a polar or an antipolar state should be accompanied by an anomaly of the dielectric permittivity. The absence of such anomalies shows that the transition from the cubic to the tetragonal phases does not have polar behaviour for $MAPbI_3$ and $MAPbBr_3$. Only for the low-temperature phase transition, we observe signatures of slowing down of the dipolar relaxation dynamics. The tetragonal phase is still characterized by polar disorder. The distinct anomalies of the ultrasonic wave velocity and attenuation allow to classify this transition as a ferro-elastic (or improper ferro-elastic [134]) one. The non-ferroelectric character of the tetragonal I4/mcm phase of both $MAPbI_3$ and $MAPbBr_3$ is further confirmed by the absence of ferroelectric P(E) hysteresis, which were done Doru Lupascu group [2].

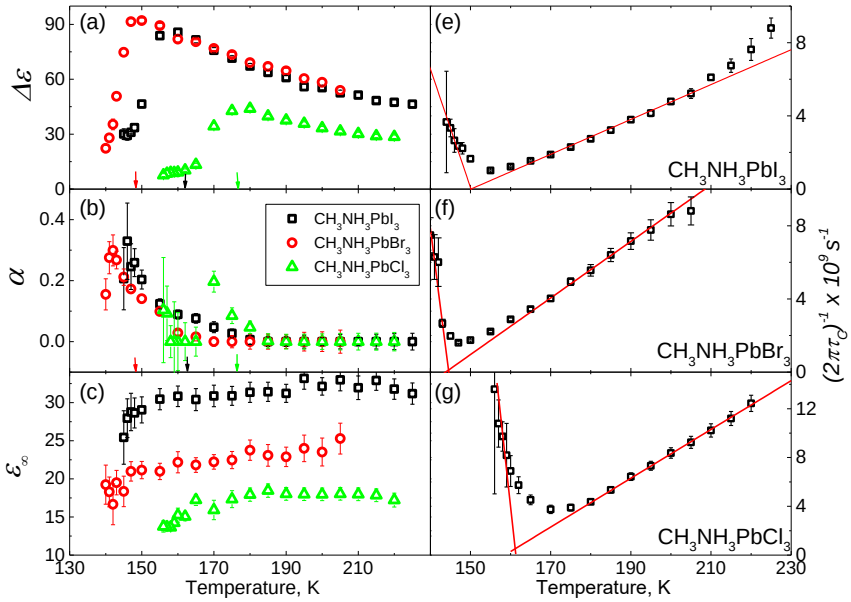

Figure 3.12 Temperature dependence of the best Cole – Cole fit parameters, (a) – relaxation strength, (b) – the width of the relaxation (c) – high frequency dielectric permittivity value. Figures from e – g show inverse relaxation time (frequency) for $MAPbI_3$ and $MAPbBr_3$ crystals and $MAPbCl_3$ polycrystalline [2].

In the literature low temperature phase has been classified either as a polar (ferroelectric)[135] or antipolar [111], [136], [137] phase, or domains made of both [138]. Our results favour the anti-polar option. The shape of the dielectric anomaly and its low value are similar to those observed for anti - ferroelectric phase transitions [7], [139], [140]. The Curie–Weiss approximation of the high temperature dependence of ε′(T) yields negative Curie–Weiss temperatures (shown in appendix A figure 3) this is typical for anti - ferroelectric phase transitions [139].

Although a small current was obtained during pyro-current measurements (Figure 3.14). For $MAPbI_3$ compound, we observed an anomaly at 163 K,

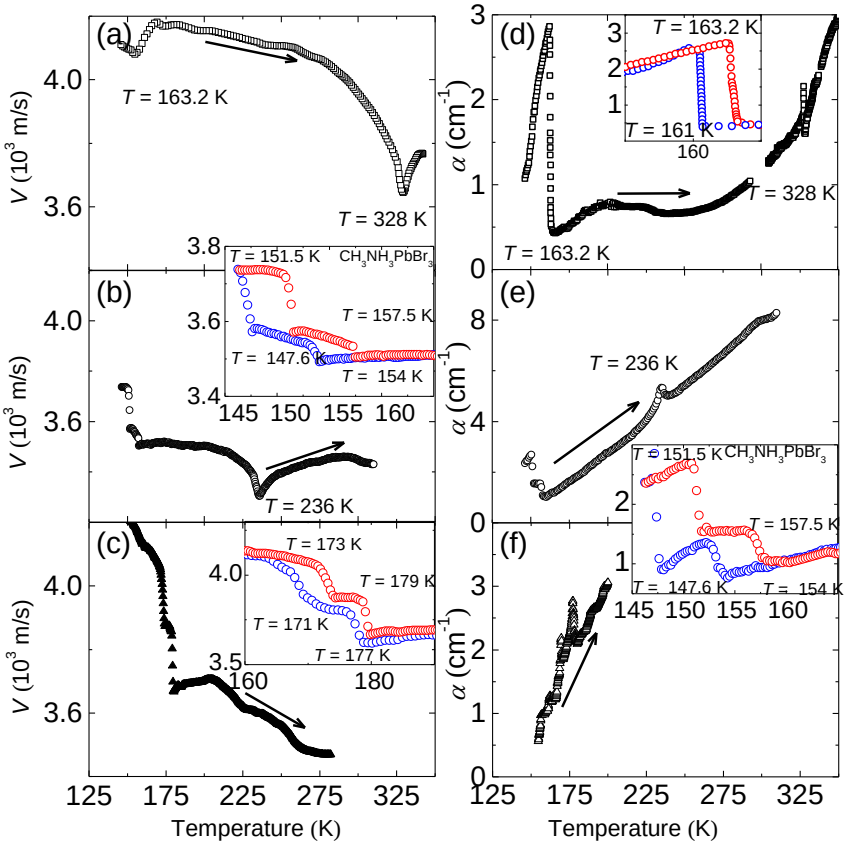

Figure 3.13 Temperature dependence of ultrasonic velocity (a-c) and attenuation (d-f) for $MAPbI_3$ (a,d), $MAPbBr_3$ (b,e) and $MAPbCl_3$ (c,f). The inserts show cooling/heating cycles in the vicinity of phase transition [2].

which corresponds to the tetragonal orthorhombic phase transition. No anomaly was observed at the cubic tetragonal transformation temperature. The pyro current of $MAPbCl_3$ exhibits two anomalies at 172 and 177 K which are related to the tetragonal orthorhombic and cubic tetragonal phase transitions. Two anomalies are also observed for $MAPbBr_3$ at 146 and 153 K which are in agreement with the low temperature phase transition temperatures. There could be several sources of the observed current such as occurrence of the electric polarization or formation of charged defects during the phase transitions. If we assume that the current has the former origin, we can use it to determine the temperature dependence of the electric polarization. In this way obtained saturation polarization is very small (around 0.2 $\mu C/cm^2$) for all halides compared to the proper ferroelectrics such as inorganic $BaTiO_3$ [7] or hybrid $[NH_4][Zn(HCOO)_3]$ [141]. Such a miniature polarization might arise from the ferro-elastic domains that disturb the long-range order of the MA+ cations.

Nevertheless our results are in contrast to theoretical calculations [120], [131], [142] and some piezo-response force microscopy (PFM) studies revealing a signal associated with ferroelectric domains of different polarity, seemingly being switchable by an electric field. [96], [117], [119], [143], [144] This slow frequency reversal of the PFM signal is actually not related to spontaneous polarization, but is due to a voltage induced charge separation that decays slowly after the electric field is switched off [145], [146]. Regular domain patterns attributed to ferro-elastic twins were reported for $MAPbI_3$ [117], [147], but no polarization switching [147] and no macroscopic polarization hysteresis [146], [148] necessary for ferroelectricity could be observed. The I4/mcm point group of $MAPbI_3$ is centrosymmetric and hence excludes ferroelectricity.

Poglitsch and Weber suggested that the low temperature orthorhombic state of $MAPbI_3$ can be ferroelectric, but later refinement of the structure showed that the correct point group is centrosymmetric Pnma [114] which can only be anti-polar [112], [136]. Similar results were calculated by M. Šimėnas that showed antipolar planes in (110) dirrection.

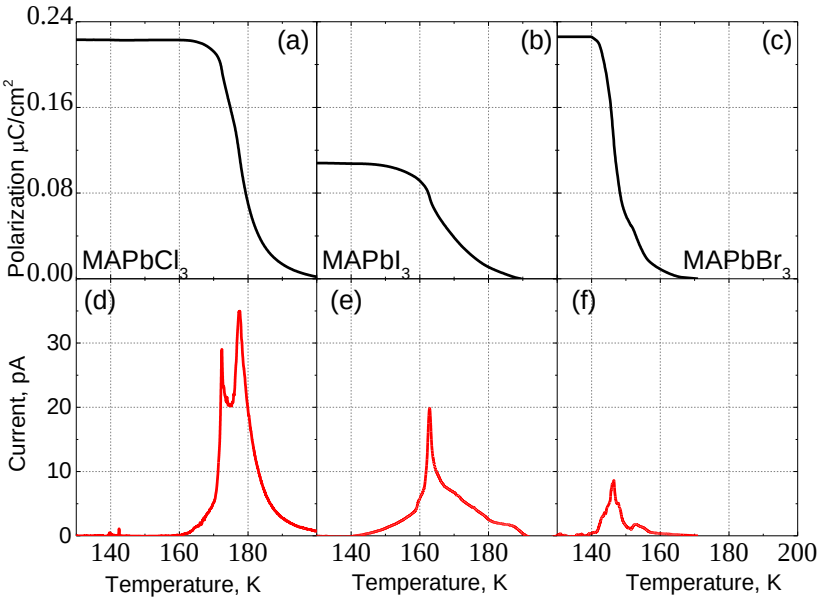

Figure 3.14. Temperature dependence of polarization (a-c) and current (d-f) for $MAPbX_3$ (I, Br, Cl) crystals. It should be noted that current depends on the measurement speed and sample size thus cannot be compered directly [4].

3.2.2 Summary

The phase transitions of all three compositions display the same sequence: cubic – tetragonal – orthorhombic. At high temperature rotation and reorientation around C - N axis of the methylammonium molecule is observed. Rotational disorder disappears at cubic to tetragonal phase transition and reorientational disorder at tetragonal to orthorhombic phase transition.

Low temperature dielectric anomalies were observed for all three compounds at temperatures of 162, 148 and 171 K for $MAPbI_3$, $MAPbBr_3$ and $MAPbCl_3$, respectively. Temperature dependence of relaxations times showed a critical slowing down phenomena which indicates order – disorder phase transition. Also a negative Curie-Weiss temperature was obtained suggesting about anti-polar nature of low temperature phase.

Although dielectric spectroscopy results show no evidence of high temperature cubic to tetragonal phase transition while acoustic result show a sharp anomaly suggesting about ferro-elastic phase.

A small current was observed during orthorhombic – tetragonal phase transition which can be explained by ferro-elastic domains that disturb the long-range order of the MA+ cations. We found no indication of ferroelectric phase for $MAPbI_3$, $MAPbBr_3$ and $MAPbCl_3$ compounds.

3.3 Mixed Lead Halides

In the last chapter we have investigated pure methylammonium lead halides ($MAPbX_3$) due to their remarkable success in solar cell scientific industry. However, further success in the commercial market is hampered by their poor thermal and water stability[149], [150] as well as lead toxicity[151]. Recently progress and efficiency of perovskite solar cells is addressed to the compositional change of perovskite crystals. By careful tuning of perovskites A - side cells with formamidium (FA), methylammonium (MA) and cesium (Cs) the mixed perovskites are more durable against exposure to heat and moisture [152]–[154]. An investigation of a complicated system of $Cs_x(FA_{0.83}MA_{0.17})_{(1-x)}Pb(I_{0.83}Br_{0.17})_3$ by Trilok Singh et al. showed high performance (up to 20% PCE) against long exposure to the ambient atmosphere [155]. Although there is still a lot of research need to be done to understand the effects of individual cations. Currently several topics on FA/MA and Cs effects are being investigate in our laboratory, sadly results are very new and won't be included in this work.

In this chapter we will discuss the effect of DMA cation in $MAPbBr_3$ crystals as recently it was reported that during certain synthesis methods relatively high amount of DMA cations can be unintentionally introduced in the MAPbBr3 structure [156]–[158]. Further studies showed that small amount of DMA may lead to enhanced solar cell performance and water stability at room temperature [159]–[161]. Although according to Anelli [162] maximal DMA solubility is around 30 % and higher amount may lead to structural instabilities. It is reported that pure $DMAPbBr_3$ has two-dimensional hexagonal structure and is unsuitable as solar cell absorber [163]–[165]. In case of classical inorganic perovskites mixing cations usually leads to obscure phase transitions [166] or frustrated phases such as relaxors [167] or dipolar glasses [50], [168]. This can strongly effect dielectric permittivity value. Having high dielectric permittivity value results in high defect tolerance

and low exciton binding energies, which further results in exceptional solar cell performance [2], [169], [170].

3.3.1 Dielectric spectroscopy of $MA_{1-x}DMA_xPbBr_3$

Temperature dependences of dielectric permittivity in a broad 20 Hz to 50 GHz frequency range for $MA_{1-x}DMA_xPbBr_3$ crystals are shown in Figure 3.17. The pure $MAPbBr_3$ exhibit the same dielectric behaviour as reported in previous chapter. A sharp dielectric anomaly is observed at 147 K temperature, which is related to first – order, anti-polar phase transition due to MA cation ordering in orthorhombic phase. A small amount of DMA content around 4 % slightly broadens and shifts the phase transition to the lower temperature (140 K). Further increase of DMA content results in very broad and highly frequency dependant anomaly. The temperatures of dielectric maximum at 129 Hz frequency are 125 K and 113 K for $x = 0.14$ and $x = 0.21$, respectively. The highest dielectric permittivity value of 251 was observed for 0.14 compound. It should be noted that from XRD data (not shown due to copyright restriction) down to 50 K temperature no structure phase transition for 0.14 and 0.21 compositions was observed. A comparison can be done with classical inorganic compounds. In the inorganic case such broad and highly frequency dependant dielectric anomalies occur due to frustration of electrical dipoles. This is usually the evidence of relaxor or a glassy state [50], [167], [171]. In our case we strongly lean to dipolar glass phase as imaginary parts of dielectric permittivity in the figure 3.15 (d and h) intersect each other especially in higher frequencies [7]. Further analyses of the frequency dependence data (Figure 3.16), for $x = 0$ and $x= 0.04$ crystal, show relaxation in the GHz frequency range related to the MA cation dynamics [169]. This relaxation disappears at tetragonal – orthorhombic phase transition when long range order is established. Nonetheless in the case of 0.14 and 0.21 compounds dipolar relaxation persist down to the lowest measured temperatures and can be seen over nine orders of magnitude, which may also imply a glassy disorder phase.

The frequency dependences of complex dielectric permittivity were approximated using superposition of several Cole – Cole model (2.16). Fitting parameters for the dipolar relaxation are shown in figures 3.17 and 3.18. For x = 0 and x = 0.04 compounds the calculated α parameter value is close to zero and slightly increases in the vicinity of the phase transition where dipolar relaxation is abruptly cut off by the tetragonal – orthorhombic phase transition. Meanwhile regarding x = 0.14 and 0.21 cases, dipolar relaxation is visible in the whole temperature range and the α parameter increases up to the value of

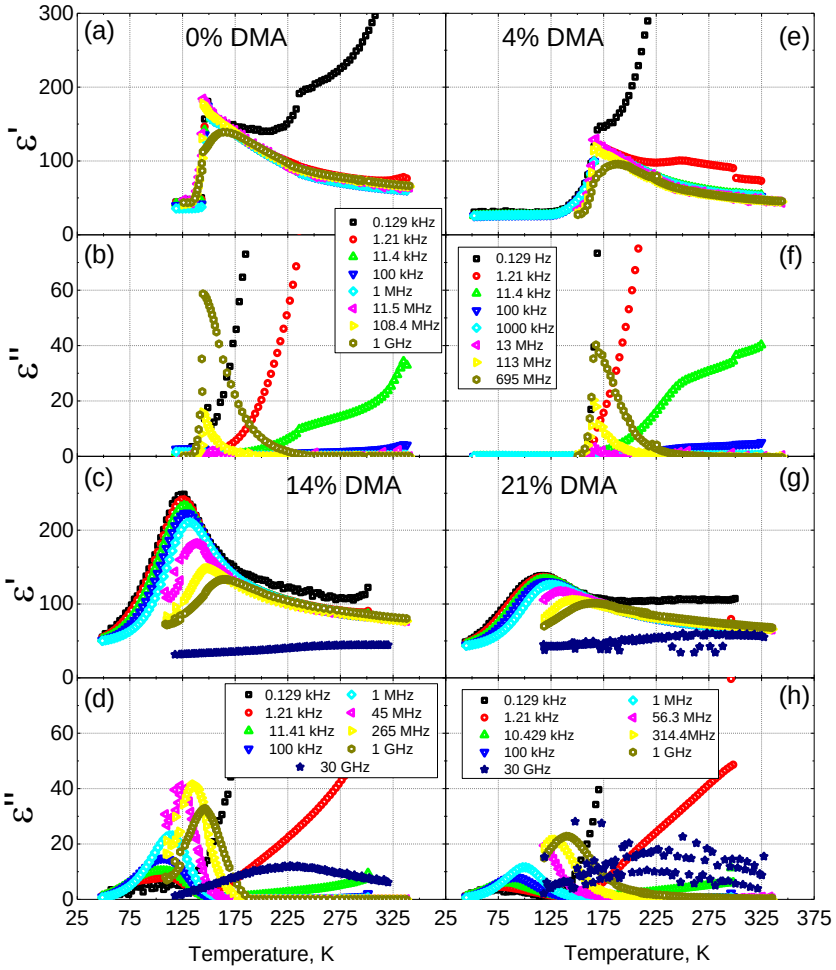

Figure 3.15. Temperature dependence of the real (a,e,c,g) and imaginary (b,f,d,h) parts of dielectric permittivity for $MA_{1-x}DMA_xPbBr_3$

0.8 at 50 K temperature. Such relaxation broadening is typical for frustrated systems [7], [18]. Moreover, the relaxation strength $\Delta\varepsilon$ gradually increases in the vicinity of the phase transition for x = 0 and x=0.04 and in the cases with higher concentration of DMA a maximum at around 100 K temperature is observed. High frequency dielectric permittivity values ε_∞ were around 30 for all compositions in the whole temperature range. The obtained temperature dependence of relaxation times for main dipolar process are shown in the

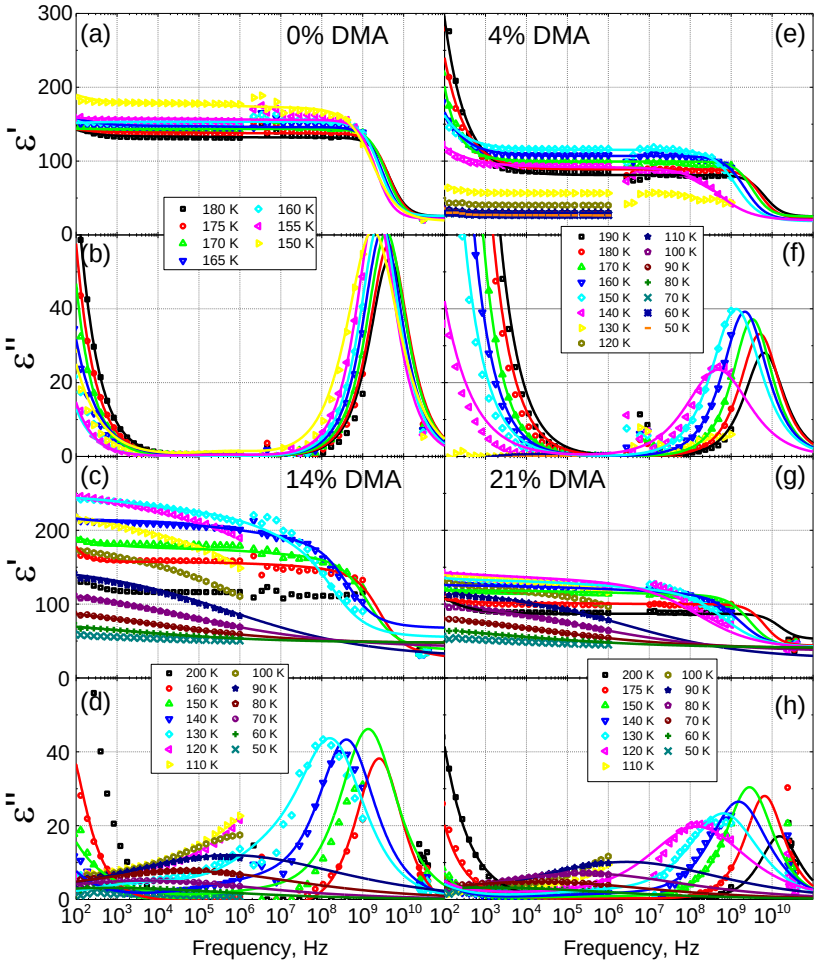

Figure 3.16 Frequency dependence of the real (a,e,c,g) and imaginary (b,f,d,h) parts of dielectric permittivity for $MA_{1-x}DMA_xPbBr_3$ crystals. Solid lines are the best fits of the Cole – Cole law.

figure 3.18. Strangely, the relaxation times follows Arrhenius law with activation energies of 80 ±5, 113 ±7, 143 ±7 and 130 ±7 meV for x=0, 0.04, 0.14 and 0.21 respectively. The absence of Vogel-Fulcher behaviour in the relaxation times for 0.14 and 0.21 composition may indicate that dipolar freezing can be found at very low temperatures as other experimental data indicates frustrated state. The obtained increase of activation energies with the increase of DMA concentration show a gradual rise of the rotational barrier for MA cation motion. Also, dielectric permittivity values at room temperature are highest for 0.14 concentration and lowest for 0.21 concentration which demonstrates the ability to tune dielectric permittivity up 50 % by changing DMA concentration.

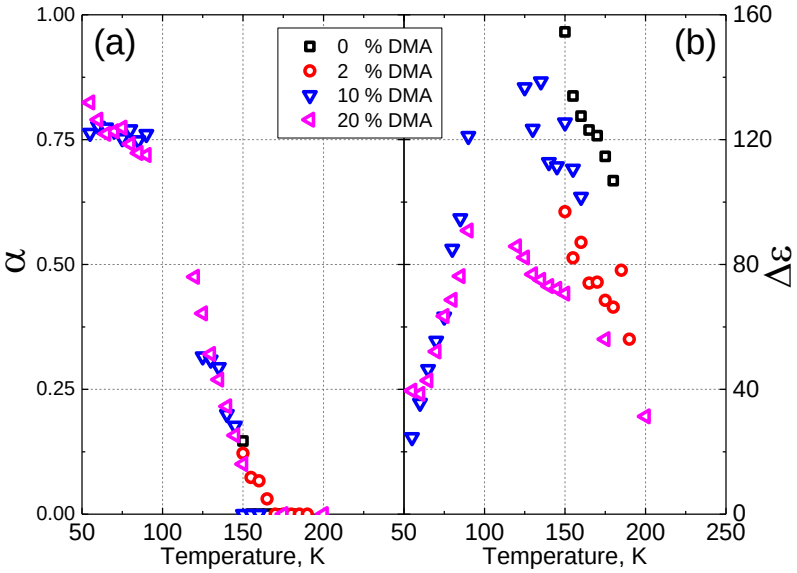

Figure 3.17 Temperature dependence of α (a) and Δε (b) fitting parameters from Cole-Cole functions.

Lastly it should be noted that temperature dependence of complex dielectric permittivity for pure $DMAPbBr_3$ is shown in Appendix B. A sharp anomaly at 251 K temperature is observed, which according to Geselle [163] is due to hexagonal to monoclinic first order phase transition. Unfortunately, $DMAPbBr_3$ crystals were too fragile and high frequency data was not obtained thus DMA dipole relaxation was not investigated. Additionally, in appendix B with permission of M. Kinka temperature dependence of acoustic velocity

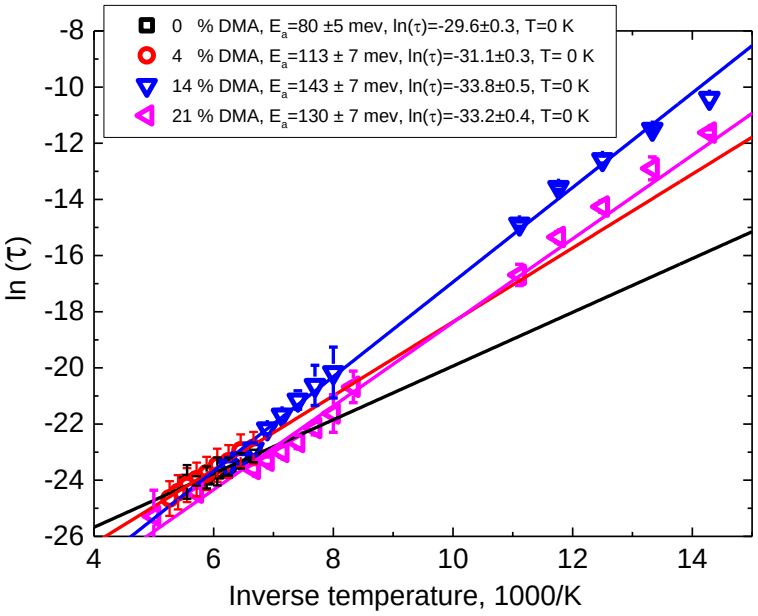

Figure 3.18 Temperature dependence of mean relaxation times for dipolar MA/DMA relaxation.

and attenuation can be found. Acoustic results revealed high temperature anomalies for crystals with 0 and 0.04 DMA cations at temperature of 234 K and 215 K, which can be attributed to cubic to tetragonal phase transitions. Also, in both cases similarly as in dielectric data an anomaly due to tetragonal orthorhombic phase transition is visible. In the case of 0.14 and 0.21 DMA compounds only one very broad anomaly below 200 K temperature can be seen. Acoustic result shows a clear suppression of the phase transition with the increase of DMA content. Also similar ultrasonic behaviour is usually observed in relaxors and dipolar glasses [172], [173] which support our earlier claim.

3.3.2 Summary

To summarize an extensive study of complex dielectric permittivity for $MA_{1-x}DMA_xPbBr_3$ crystals over wide temperature and frequency range was performed. A small amount of DMA cation leads to the phase transition broadening and a shift from 147 K to 140 K temperature. Although structural phase transitions and long-range MA cations order is still preserved. Crystals with higher amount of DMA cations concentration show significant

broadening of the dielectric anomaly. Temperatures dependence of relaxation times showed Arrhenius like behaviour despite the glassy behaviour of dielectric data. Also, with the increase of DMA concentration notable increase of activation energy from 80 to 140 meV was observed which may indicate the rise of MA cation rotational barrier. The fact that dielectric data show dipolar glass like behaviour and with supplementation of XRD and acoustic data it was concluded that significant suppression of tetragonal phase occurs due to frustrated dipolar interaction between molecular cations and Arrhenius like behaviour is observed due to very low Vogel-Fulcher freezing temperatures. It is worth mention that currently work with $MA_{x-1}FA_xPbBr_3$ is being done and preliminary results show similar behaviour.

3.4 Hybrid perovskite framework

In the recent decade considerable attention was given to perovskite like structures: metal – organic frameworks MOF. It was shown that such perovskites can exhibit ferroelectric and ferromagnetic properties [174]–[178]. Dimethylammonium zinc - formate $[(CH_3)_2NH_2][Zn][(HCOO)_3]$ has a perovskite structure where metal center Zn^{2+} sits in the middle of six formate ($HCOO^-$) linkers forming an octahedral. In the perovskite A site a DMA^+ molecule can be found that forms hydrogen bonds with the rest of the framework [179]. Similar MOFs only with different metal centres usually display the same phase transition (trigonal – monoclinic [180]). The main difference is that depending on the metal center, the temperature of the phase transition may vary from 155 K to 190 K [175], [181], [182]. The nature of the particular phase transition is due to the ordering of molecular cations and deformation of the framework. It is reported that in the high temperature phase DMA molecule can freely move between three positions and at low temperatures DMA molecule freezes and long range order is formed [180].

Previous dielectric studies of $DMAZn(HCOO)_3$ crystal suggested that spontaneous polarization appears during trigonal – monoclinic phase transition. Although no evidence of the polarization switching was provided [183]–[187]. Also the same studies argue that observed dipolar relaxation is due to relaxor behaviour. It should be noted relaxor phase is usually seen in chemically disordered systems, like PMN ($Pb(Mg_{1/2}Nb_{2/3})O_3$) [188] or BTZ ($Ba(Ti_{0.7}Zr_{0.3})O_3$) [189]. Nevertheless, in the previous studies the measured frequency range of 10 Hz to 1 MHz was too narrow to draw reliable conclusions.

3.4.1 Dielectric spectroscopy of $DMAZn(HCOO)_3$

In order to investigate dipolar dynamics of $DMAZn(HCOO)_3$ compounds a broadband dielectric spectroscopy in the frequency range of 10^{-2} to 10^{9} Hz was performed. The temperature dependence of real and imaginary parts of dielectric permittivity is shown in the figure 3.19. A sharp anomaly at 155 K temperature in the real part of dielectric permittivity is observed due to first order phase transition from trigonal to monoclinic phase and is in a good agreement with earlier works [183]–[187]. In the higher temperature phase, complex dielectric permittivity shows dipolar relaxation. This relaxation is cut off at phase transition temperature as long-range order is established.

Further frequency dependant of the complex dielectric permittivity at different temperatures is presented in the figure 3.20. A clear relaxation in the high temperature phase is visible. This relaxation moves from GHz to kilohertz range as temperature decreases from the room temperature. Additionally, at the low temperature phase a weak relaxation is visible.

Frequency dependences were approximated using Cole – Cole model (2.16) for one process. Alfa parameter (α) that describes the width of the

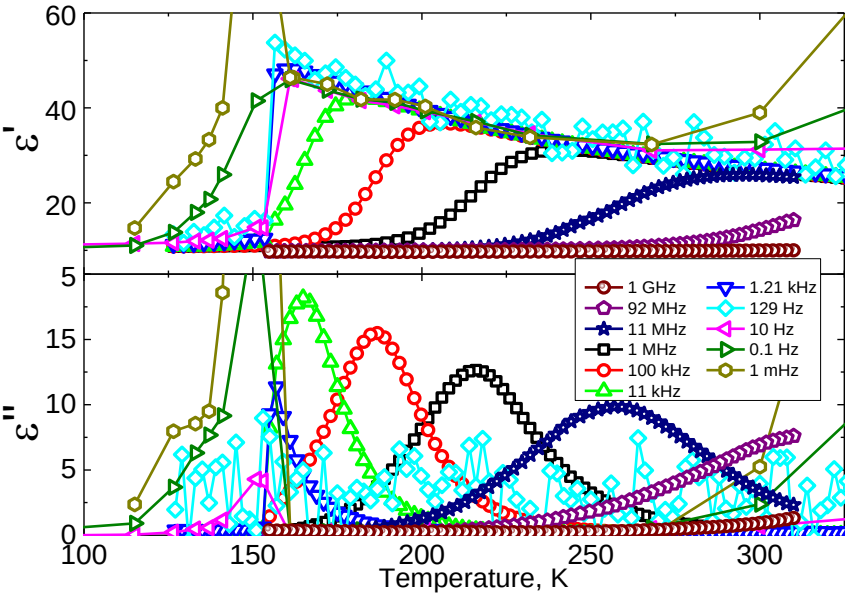

Figure 3.19 Temperature dependence of real (top) and imaginary (bottom) parts of dielectric permittivity for $DMAZn(HCOO)_3$ crystal in [012] direction [5].

relaxation is less than 0.05 in the whole temperature range. This indicates that our relaxation is very close to Debye like relaxation where dipoles do not interact with each other and thermal fluctuation is the dominant force in the interaction. Also, inverse temperature dependence of relaxation times (Figure 3.21) shown Arrhenius like behaviour (2.18) with the activation energy (E_a) of 270 ± 10 meV. Interestingly, our value obtained from dielectric spectroscopy is very close to the value obtained by T. Asaji in his NMR experiments with activation energy of 240 meV. He relates this process to 120^0 reorientation of DMA cation around C – C axis [190], [191]. Such

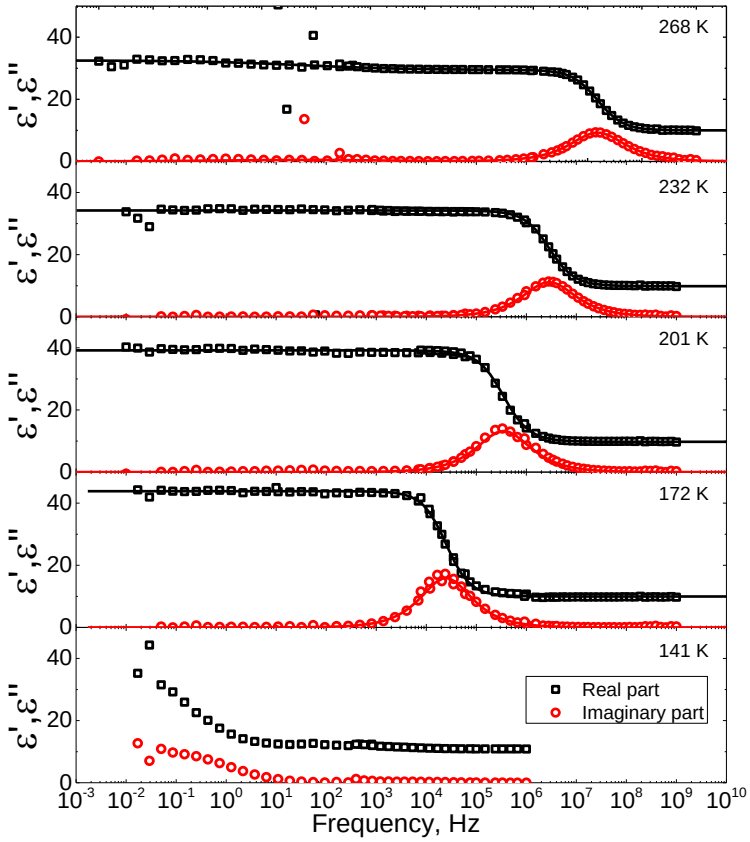

Figure 3.20 Frequency dependence of real (top) and imaginary (bottom) parts of dielectric permittivity for DMAZn(HCOO)$_3$ crystal in [012] direction [5]. At different temperatures.

rotations significantly changes the dipolar moment of DMA molecule thus should appear in the dielectric spectra.

Further to determine the origin of the relaxation at low temperature phase, the relaxation times were extracted from the maxima of imaginary part of dielectric permittivity. Results were approximated using Arrhenius law (Appendix C, Figure 1). The obtained activation energy of 290 ± 20 meV is very close to the value of DMA cation hopping at high temperature phase. This may indicate that this motion also persists even in the low temperature phase as discussed by Yadav et al [187]. Although the precise nature of the relaxation is still not clear.

Our linier Arrhenius – type behaviour of mean relaxation times for DMA molecule indicates a simple thermally activated process[18]. This can be seen over whole high temperature phase. Thus our result are in clear conflict with widely discussed idea that $DMAZn(HCOO)_3$ are relaxors or exhibit relaxor like behaviour [183]–[187]. In the case of relaxors, the temperature dependence deviate from Arrhenius law and follow Vogel – Fulcher law (2.19) [167]. Also in the relaxor phase the temperature dependence of the

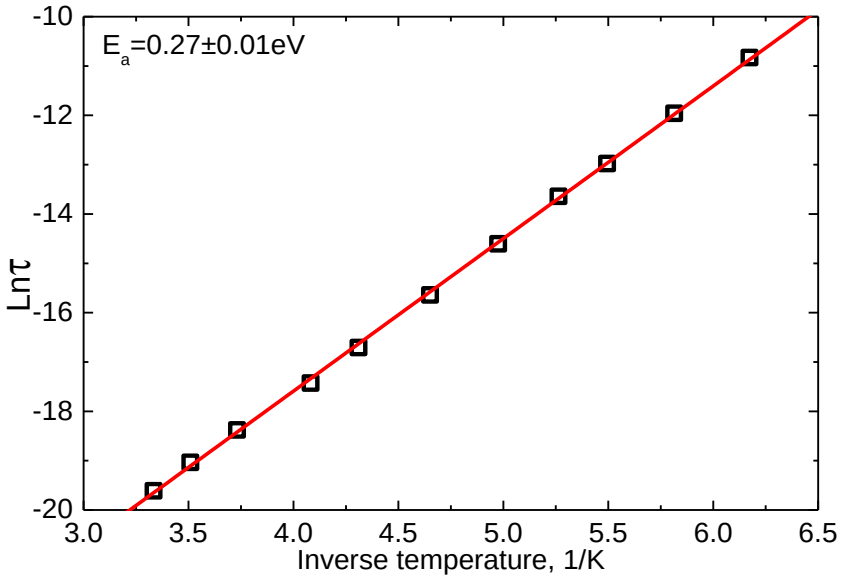

Figure 3.21 Inverse temperature dependence of the relaxation times for DMA cations reorientation of 120^0 around C – C axis. The solid line represent the best Arrhenius fit [5].

complex dielectric permittivity is slightly different and most noticeable is the imaginary part, where at low temperature dielectric curves combine into one curve [192]. In our case dielectric data is more similar to dipolar glass phase [193], [194]. Although similarly as in relaxors case relaxation times have to follow Vogel – Fulcher law. Also I would like to note that relaxor like behaviour is usually observed in chemically disordered systems [166], while $DMAZn(HCOO)_3$ compound is ordered and clearly has no frustrated states. Furthermore, I would like to address a question that may arise due to previous chapter about $DMA_xMA_{x-1}PbBr_3$. In that chapter temperature dependence of relaxation time with high amount of DMA cation followed Arrhenius law nevertheless we claimed that we have a frustrated state. One of the key points was that dielectric results were complimented with other data, but I want to address the key difference in dielectric behaviour, mainly the width (α) of relaxation. In the case of $DMAZn(HCOO)_3$ the relaxation width was close to 0 and it didn't change in the whole temperature range and in case of $DMA_xMA_{x-1}PbBr_3$ the relaxation width increased as the temperature decreased, which is typical behaviour for frustrated system like relaxors or dipolar glasses [7].

Lastly in order to confirm non-ferroelectric origin electrical polarization and high field dielectric permittivity measurements were performed (Figure 3.22 a and b). At the temperature of 162 K a slightly open polarization curve was observed, which is typical for lossy dielectric [195], this was also confirmed during measurement by checking the current which showed no indication of switching. Considering other temperatures, all curves are closed and slight change in the slope of the curve is due to change in the dielectric permittivity value. We also did not observe any electric field influence on the real part of the dielectric permittivity (tunability effect [196]) This supports the non-ferroelectric or improper ferroelectric origin of this compound and indicates that the DMA cation motion is not hindered by an electric field of up to 14 kV cm^{-1}.

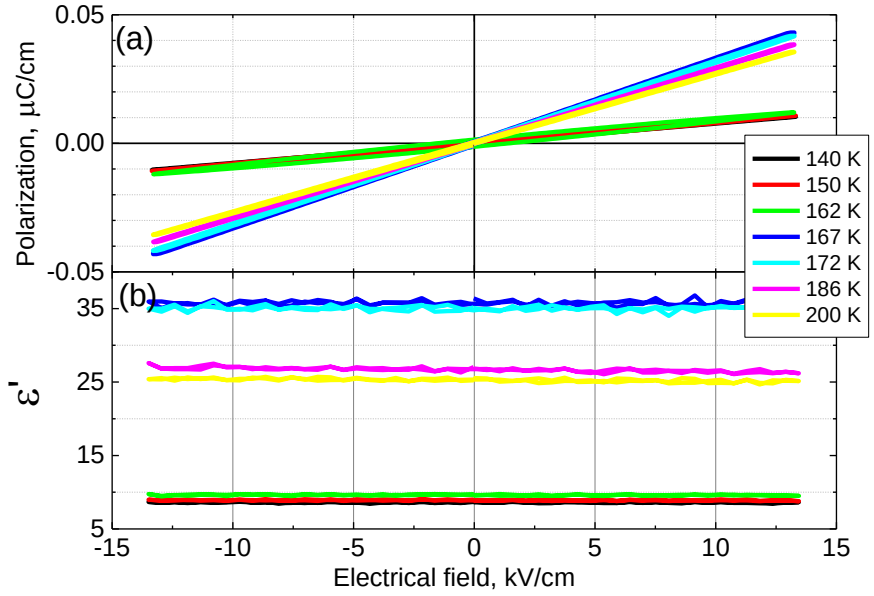

Figure 3.22 Polarization measurement (a) and electrical field dependence of real part of dielectric permittivity (b) at different

3.4.2 Summary

To summarize we have performed broadband dielectric spectroscopy on $DMAZn(HCOO)_3$ crystals. Temperature dependence of dielectric permittivity revealed an anomaly at 155 K temperature due to first order phase transition. Also, in the high temperature phase dipolar dynamics of DMA molecule was observed. The temperature dependence of the mean relaxation time of this process strictly follows the Arrhenius law over ten orders of magnitude, ruling out the widely discussed incorrect notion of relaxor behaviour of this compound. Also, our obtained activation energy value of 270 meV is in good agreement with NMR result indicating that observed dipolar relaxation is due to reorientation of DMA molecule around C – C axis. And lastly non-ferroelectric behaviour was further confirmed by the electric field dependent electric polarization and dielectric permittivity measurements.

4. Conclusions

The following conclusion can be drawn by accomplishing our tasks:

1. The largest contribution to dielectric permittivity in microwave region in BT/KN, BT/BT "core – shell" systems come from electro – mechanical resonance in BT grains. Increased spontaneous polarization value in 0.25BT/KN system and increased dielectric permittivity value for BF/BT system can be attributed to the fact that the lattice of the "core" part of the composite is stressed by the outer "shell". This can be considered as an indication of an artificial MPB.

2. Broadband dielectric spectroscopy result revealed first – order, order – disorder, anti-polar phase transition at low temperature for all three $MAPbX_3$ (I, Br, Cl) compounds. Also, the same results reveal a dipolar relaxation which is related to rotation and reorientation of MA cation around C – N axis. We found no indication of ferroelectric phase for any one of the three compounds.

3. A small amount of DMA cation in the $MA_{1-x}DMA_xPbBr_3$ crystals leads to the phase transition broadening and a shift to the lower temperatures. Although structural phase transitions and long-range MA cations order is still preserved. Crystals with higher amount of DMA cations concentration show significant broadening and suppression of tetragonal phase, which may be related frustrated state. Also, with the increase of DMA concentration a rise of MA cation rotational barrier is observed.

4. Broadband dielectric spectroscopy revealed a first order phase transition at 155 K temperature for $DMAZn(HCOO)_3$ crystal. At the high temperature phase, a simple dipolar DMA molecule dynamic was revealed that follow Arrhenius law. Also, non-ferroelectric behaviour was further confirmed by the electric field dependent of electric polarization and dielectric permittivity measurements.

Literature

[1] S. Balčiūnas, M. Ivanov, J. Banys, and S. Wada, “Dielectric Properties of BaTiO3-KNbO3 Composites,” *Ferroelectrics*, vol. 512, no. 1, pp. 8–13, 2017.

[2] I. Anusca *et al.*, “Dielectric Response: Answer to Many Questions in the Methylammonium Lead Halide Solar Cell Absorbers,” *Adv. Energy Mater.*, vol. 7, no. 19, p. 1700600, 2017, doi: 10.1002/aenm.201700600.

[3] S. Balčiūnas *et al.*, “Dielectric properties of BT-BT and BF-BT composites,” *Ferroelectrics*, vol. 533, no. 1, pp. 145–150, Sep. 2018, doi: 10.1080/00150193.2018.1470830.

[4] M. Šimėnas, S. Balčiūnas, M. Mączka, J. Banys, and E. E. Tornau, “Exploring the Antipolar Nature of Methylammonium Lead Halides: A Monte Carlo and Pyrocurrent Study,” *J. Phys. Chem. Lett.*, vol. 8, no. 19, pp. 4906–4911, Oct. 2017, doi: 10.1021/acs.jpclett.7b02239.

[5] M. Simenas *et al.*, “Elucidation of dipolar dynamics and nature of structural phases in [(CH3)2NH2][Zn(HCOO)3] hybrid perovskite framework,” *J. Mater. Chem. C*, May 2019, doi: 10.1039/C9TC01275C.

[6] R. E. Sonntag, C. Borgnakke, and G. J. Van Wylen, *Fundamentals of Thermodynamics*. Wiley, 2003.

[7] M. E. Lines and A. M. Glass, *Principles and Applications of Ferroelectrics and Related Materials*. OUP Oxford, 2001.

[8] R. Watton, C. Smith, and G. Jones, “Pyroelectric materials: Operation and performance in the pyroelectric camera tube,” *Ferroelectrics*, vol. 14, no. 1, pp. 719–721, 1976.

[9] H. Iwasaki, N. Uchida, and T. Yamada, “Pyroelectricity and Spontaneous Polarization in LiTaO3,” *Jpn. J. Appl. Phys.*, vol. 6, no. 11, p. 1336, 1967.

[10] S. Porter, “A brief guide to pyroelectric detectors,” *Ferroelectrics*, vol. 33, no. 1, pp. 193–206, 1981.

[11] A. Von Hippel, “Ferroelectricity, domain structure, and phase transitions of barium titanate,” *Rev. Mod. Phys.*, vol. 22, no. 3, p. 221, 1950.

[12] J. Valasek, “Piezo-electric and allied phenomena in Rochelle salt,” *Phys. Rev.*, vol. 17, no. 4, p. 475, 1921.

[13] G. Shirane, J. Axe, J. Harada, and J. Remeika, “Soft ferroelectric modes in lead titanate,” *Phys. Rev. B*, vol. 2, no. 1, p. 155, 1970.

[14] A. Tagantsev *et al.*, “The origin of antiferroelectricity in PbZrO 3,” *Nat. Commun.*, vol. 4, no. 1, pp. 1–8, 2013.

[15] C. Darlington, “The primary order parameter in antiferroelectric NaNbO3,” *Solid State Commun.*, vol. 29, no. 3, pp. 307–311, 1979.
[16] W. Mason and B. Matthias, “The Piezoelectric, Dielectric, and Elastic Properties of N D 4 D 2 P O 4 (Deuterated ADP),” *Phys. Rev.*, vol. 88, no. 3, p. 477, 1952.
[17] B. A. Strukov and A. P. Levanyuk, *Ferroelectric Phenomena in Crystals: Physical Foundations*. Springer Science & Business Media, 2012.
[18] F. Kremer and A. Schönhals, *Broadband Dielectric Spectroscopy*. Springer Science & Business Media, 2012.
[19] Y. Imry and M. Wortis, “Influence of quenched impurities on first-order phase transitions,” *Phys. Rev. B*, vol. 19, no. 7, pp. 3580–3585, Apr. 1979, doi: 10.1103/PhysRevB.19.3580.
[20] A. Faghri and Y. Zhang, *Fundamentals of Multiphase Heat Transfer and Flow*. Springer International Publishing, 2020.
[21] B. Strukov, A. Sigov, V. Fedorikhin, and S. Taraskin, “Heat capacity anomalies in}-irradiated triglycin sulfate crystals,” *JETP Lett*, vol. 31, no. 3, 1980.
[22] N. Setter, “What is a ferroelectric–a materials designer perspective,” *Ferroelectrics*, vol. 500, no. 1, pp. 164–182, 2016.
[23] M. Drougard and D. Young, “Dielectric Constant Behavior of Single-Domain, Single Crystals of Barium Titanate in the Vicinity of the Curie Point,” *Phys. Rev.*, vol. 95, no. 5, p. 1152, 1954.
[24] H. Mueller, “Properties of Rochelle salt,” *Phys. Rev.*, vol. 47, no. 2, p. 175, 1935.
[25] V. M. Goldschmidt, “Die gesetze der krystallochemie,” *Naturwissenschaften*, vol. 14, no. 21, pp. 477–485, 1926.
[26] M. Pena and J. Fierro, “Chemical structures and performance of perovskite oxides,” *Chem. Rev.*, vol. 101, no. 7, pp. 1981–2018, 2001.
[27] V. Goldschmidt, “The laws of crystal chemistry,” *Naturwissenschaften*, vol. 14, no. 21, pp. 477–485, 1926.
[28] A. Glazer, “The classification of tilted octahedra in perovskites,” *Acta Crystallogr. B*, vol. 28, no. 11, pp. 3384–3392, 1972.
[29] N. Zhang *et al.*, “The missing boundary in the phase diagram of PbZr 1− x Ti x O 3,” *Nat. Commun.*, vol. 5, no. 1, pp. 1–9, 2014.
[30] N.-G. Park, M. Grätzel, T. Miyasaka, K. Zhu, and K. Emery, “Towards stable and commercially available perovskite solar cells,” *Nat. Energy*, vol. 1, no. 11, pp. 1–8, 2016.

[31] C. Pillai and A. George, “Thermal conductivity of LaCoO 3,” *Int. J. Thermophys.*, vol. 4, no. 2, pp. 183–188, 1983.
[32] J. Longo, P. Raccah, and J. B. Goodenough, “Magnetic properties of SrRuO3 and CaRuO3,” *J. Appl. Phys.*, vol. 39, no. 2, pp. 1327–1328, 1968.
[33] K. C. Kao, *Dielectric phenomena in solids*. Elsevier, 2004.
[34] K. S. Cole and R. H. Cole, “Dispersion and absorption in dielectrics I. Alternating current characteristics,” *J. Chem. Phys.*, vol. 9, no. 4, pp. 341–351, 1941.
[35] S. Havriliak and S. Negami, “A complex plane representation of dielectric and mechanical relaxation processes in some polymers,” *Polymer*, vol. 8, pp. 161–210, 1967.
[36] S. Shtrikman and E. Wohlfarth, “The theory of the Vogel-Fulcher law of spin glasses,” *Phys. Lett. A*, vol. 85, no. 8–9, pp. 467–470, 1981.
[37] Z. Hashin and S. Shtrikman, “A variational approach to the theory of the effective magnetic permeability of multiphase materials,” *J. Appl. Phys.*, vol. 33, no. 10, pp. 3125–3131, 1962.
[38] N. J. Kidner, N. H. Perry, T. O. Mason, and E. J. Garboczi, “The brick layer model revisited: introducing the nano-grain composite model,” *J. Am. Ceram. Soc.*, vol. 91, no. 6, pp. 1733–1746, 2008.
[39] K. Lichtenecker, “Die dielektrizitatskonstante naturlicher und kunstlicher mischkorper,” *Phys. Z.*, vol. 27, pp. 115–158, 1926.
[40] A. Goncharenko, V. Lozovski, and E. Venger, “Lichtenecker’s equation: applicability and limitations,” *Opt. Commun.*, vol. 174, no. 1–4, pp. 19–32, 2000.
[41] R. Blinc, *Advanced ferroelectricity*, vol. 151. Oxford University Press, 2011.
[42] J. Macutkevic, J. Banys, R. Grigalaitis, and Y. Vysochanskii, “Asymmetric phase diagram of mixed CuInP 2 (S x Se 1− x) 6 crystals,” *Phys. Rev. B*, vol. 78, no. 6, p. 064101, 2008.
[43] J. Banys, R. Grigalaitis, A. Mikonis, J. Macutkevic, and P. Keburis, “Distribution of relaxation times of relaxors: comparison with dipolar glasses,” *Phys. Status Solidi C*, vol. 6, no. 12, pp. 2725–2730, 2009.
[44] A. Bishop, A. Bussmann-Holder, S. Kamba, and M. Maglione, “Common characteristics of displacive and relaxor ferroelectrics,” *Phys. Rev. B*, vol. 81, no. 6, p. 064106, 2010.

[45] A. Bussmann-Holder, “The polarizability model for ferroelectricity in perovskite oxides,” *J. Phys. Condens. Matter*, vol. 24, no. 27, p. 273202, 2012.
[46] Z. Ye, “Relaxor ferroelectric complex perovskites: structure, properties and phase transitions,” 1998, vol. 155, pp. 81–122.
[47] G. Xu, Z. Zhong, Y. Bing, Z.-G. Ye, and G. Shirane, “Electric-field-induced redistribution of polar nano-regions in a relaxor ferroelectric,” *Nat. Mater.*, vol. 5, no. 2, pp. 134–140, 2006.
[48] A. Levstik, Z. Kutnjak, C. Filipič, and R. Pirc, “Glassy freezing in relaxor ferroelectric lead magnesium niobate,” *Phys. Rev. B*, vol. 57, no. 18, p. 11204, 1998.
[49] F. Ladieu, J. Le Cochec, P. Pari, P. Trouslard, and P. Ailloud, “Dielectric constant of glasses: evidence for dipole-dipole interactions,” *Phys. Rev. Lett.*, vol. 90, no. 20, p. 205501, 2003.
[50] U. Höchli, K. Knorr, and A. Loidl, “Orientational glasses,” *Adv. Phys.*, vol. 39, no. 5, pp. 405–615, 1990.
[51] R. Böhmer, M. Maglione, P. Lunkenheimer, and A. Loidl, “Radio-frequency dielectric measurements at temperatures from 10 to 450 K,” *J. Appl. Phys.*, vol. 65, no. 3, pp. 901–904, 1989.
[52] J. Banys, S. Lapinskas, S. Rudys, S. Greicius, and R. Grigalaitis, “High frequency measurements of ferroelecrics and related materials in coaxial line,” *Ferroelectrics*, vol. 414, no. 1, pp. 64–69, 2011.
[53] J. Grigas, *Microwave dielectric spectroscopy of ferroelectrics and related materials*. Routledge, 2019.
[54] V. Valevichius, V. Samulionis, and J. Banys, “Ultrasonic dispersion in the phase transition region of ferroelectric materials,” *J. Alloys Compd.*, vol. 211, pp. 369–373, 1994.
[55] I. Fujii *et al.*, “Enhanced piezoelectric response of BaTiO3–KNbO3 composites,” *Appl. Phys. Lett.*, vol. 99, no. 20, p. 202902, 2011.
[56] S. Wada *et al.*, “Preparation of barium titanate–potassium niobate nanostructured ceramics with artificial morphotropic phase boundary structure by solvothermal method,” *Jpn. J. Appl. Phys.*, vol. 50, no. 9S2, p. 09NC08, 2011.
[57] Y. Hirose, S. Ueno, K. Nakashima, and S. Wada, “Preparation of BaTiO3 nano-structured ceramics by solvothermal solidification method,” *Trans. Mater. Res. Soc. Jpn.*, vol. 40, no. 3, pp. 239–242, 2015.

[58] Y. Hirose, S. Ueno, K. Nakashima, and S. Wada, “Fabrication of BaTiO3/BiFeO3 nano-complex ceramics by hydrothermal method,” *Trans. Mater. Res. Soc. Jpn.*, vol. 39, no. 2, pp. 105–108, 2014.

[59] J.-H. Im, C.-R. Lee, J.-W. Lee, S.-W. Park, and N.-G. Park, “6.5% efficient perovskite quantum-dot-sensitized solar cell,” *Nanoscale*, vol. 3, no. 10, pp. 4088–4093, 2011.

[60] D. Berlincourt, C. Cmolik, and H. Jaffe, “Piezoelectric properties of polycrystalline lead titanate zirconate compositions,” *Proc. IRE*, vol. 48, no. 2, pp. 220–229, 1960.

[61] Y. Qin, S. Zhang, Y. Wu, C. Lu, and J. Zhang, “Impacts of acceptor doping on the piezoelectric properties and domain structure in NBT-based lead-free ceramics,” *J. Eur. Ceram. Soc.*, vol. 37, no. 11, pp. 3493–3500, 2017.

[62] G. Viola, R. McKinnon, V. Koval, A. Adomkevicius, S. Dunn, and H. Yan, “Lithium-induced phase transitions in lead-free Bi0. 5Na0. 5TiO3 based ceramics,” *J. Phys. Chem. C*, vol. 118, no. 16, pp. 8564–8570, 2014.

[63] W. Bai, P. Li, L. Li, J. Zhang, B. Shen, and J. Zhai, “Structure evolution and large strain response in BNT–BT lead-free piezoceramics modified with Bi (Ni0. 5Ti0. 5) O3,” *J. Alloys Compd.*, vol. 649, pp. 772–781, 2015.

[64] P. Berik, W.-Y. Chang, and X. Jiang, “Piezoelectric d 36 in-plane shear-mode of lead-free BZT-BCT single crystals for torsion actuation,” *Appl. Phys. Lett.*, vol. 110, no. 5, p. 052902, 2017.

[65] T. Zheng *et al.*, “The structural origin of enhanced piezoelectric performance and stability in lead free ceramics,” *Energy Environ. Sci.*, vol. 10, no. 2, pp. 528–537, 2017.

[66] B. Jaffe, *Piezoelectric ceramics*, vol. 3. Elsevier, 2012.

[67] R. Guo, L. Cross, S. Park, B. Noheda, D. Cox, and G. Shirane, “Origin of the high piezoelectric response in PbZr 1− x Ti x O 3,” *Phys. Rev. Lett.*, vol. 84, no. 23, p. 5423, 2000.

[68] T. Ostapchuk *et al.*, “Infrared and THz soft-mode spectroscopy of (Ba, Sr) TiO3 ceramics,” *Ferroelectrics*, vol. 367, no. 1, pp. 139–148, 2008.

[69] M. Fontana, G. Metrat, J. Servoin, and F. Gervais, “Infrared spectroscopy in KNbO3 through the successive ferroelectric phase transitions,” *J. Phys. C Solid State Phys.*, vol. 17, no. 3, p. 483, 1984.

[70] Z. Zhao *et al.*, “Grain-size effects on the ferroelectric behavior of dense nanocrystalline BaTiO 3 ceramics,” *Phys. Rev. B*, vol. 70, no. 2, p. 024107, 2004.
[71] R. Newton, A. Ahearn, and K. McKay, “Observation of the ferro-electric Barkhausen effect in barium titanate,” *Phys. Rev.*, vol. 75, no. 1, p. 103, 1949.
[72] S. Kashida, I. Hatta, A. Ikushima, and Y. Yamada, “Ultrasonic velocities in BaTiO3,” *J. Phys. Soc. Jpn.*, vol. 34, no. 4, pp. 997–1001, 1973.
[73] H. Huntington and R. Southwick, “Ultrasonic velocities in polarized barium titanate ceramics,” *J. Acoust. Soc. Am.*, vol. 27, no. 4, pp. 677–679, 1955.
[74] G. Arlt, U. Böttger, and S. Witte, “Dielectric dispersion of ferroelectric ceramics and single crystals at microwave frequencies,” *Ann. Phys.*, vol. 506, no. 7-8, pp. 578–588, 1994.
[75] D. Nuzhnyy *et al.*, “Percolation in the dielectric function of Pb (Zr, Ti) O3–Pb2Ru2O6. 5 ferroelectric–metal composites,” *J. Phys. Appl. Phys.*, vol. 47, no. 49, p. 495301, 2014.
[76] B. Cheng, M. Gabbay, W. Duffy, and G. Fantozzi, “Mechanical loss and Young’s modulus associated with phase transitions in barium titanate based ceramics,” *J. Mater. Sci.*, vol. 31, no. 18, pp. 4951–4955, 1996.
[77] J. Wang, F. Meng, X. Ma, M. Xu, and L. Chen, “Lattice, elastic, polarization, and electrostrictive properties of BaTiO 3 from first-principles,” *J. Appl. Phys.*, vol. 108, no. 3, p. 034107, 2010.
[78] A. J. Bell, “Phenomenologically derived electric field-temperature phase diagrams and piezoelectric coefficients for single crystal barium titanate under fields along different axes,” *J. Appl. Phys.*, vol. 89, no. 7, pp. 3907–3914, 2001.
[79] H. F. Kay and P. Vousden, “XCV. Symmetry changes in barium titanate at low temperatures and their relation to its ferroelectric properties,” *Lond. Edinb. Dublin Philos. Mag. J. Sci.*, vol. 40, no. 309, pp. 1019–1040, 1949.
[80] J. Shieh, J. Yeh, Y. Shu, and J. Yen, “Hysteresis behaviors of barium titanate single crystals based on the operation of multiple 90 switching systems,” *Mater. Sci. Eng. B*, vol. 161, no. 1–3, pp. 50–54, 2009.
[81] H. Wieder, “Electrical behavior of barium titanatge single crystals at low temperatures,” *Phys. Rev.*, vol. 99, no. 4, p. 1161, 1955.
[82] T. Schenk *et al.*, “About the deformation of ferroelectric hystereses,” *Appl. Phys. Rev.*, vol. 1, no. 4, p. 041103, 2014.

[83] L. Jin, F. Li, and S. Zhang, “Decoding the fingerprint of ferroelectric loops: comprehension of the material properties and structures,” *J. Am. Ceram. Soc.*, vol. 97, no. 1, pp. 1–27, 2014.

[84] N. H. Khansur, H. Kawashima, S. Wada, J. M. Hudspeth, and J. Daniels, “Enhanced extrinsic domain switching strain in core–shell structured BaTiO3–KNbO3 ceramics,” *Acta Mater.*, vol. 98, pp. 182–189, 2015.

[85] Z. Zhao *et al.*, “Grain-size effects on the ferroelectric behavior of dense nanocrystalline BaTiO 3 ceramics,” *Phys. Rev. B*, vol. 70, no. 2, p. 024107, 2004.

[86] Y. Hirose, S. Ueno, K. Nakashima, and S. Wada, “Preparation of BaTiO3 Nano-structured Ceramics by Solvothermal Solidification Method,” *Trans. Mater. Res. Soc. Jpn.*, vol. 40, no. 3, pp. 239–242, 2015.

[87] T. Hoshina, K. Takizawa, J. Li, T. Kasama, H. Kakemoto, and T. Tsurumi, “Domain size effect on dielectric properties of barium titanate ceramics,” *Jpn. J. Appl. Phys.*, vol. 47, no. 9S, p. 7607, 2008.

[88] T. Hoshina *et al.*, “Size Effect of Nanograined BaTiO3 Ceramics Fabricated by Aerosol Deposition Method,” *Jpn. J. Appl. Phys.*, vol. 49, no. 9S, p. 09MC02, Sep. 2010, doi: 10.1143/JJAP.49.09MC02.

[89] M. Frey, Z. Xu, P. Han, and D. Payne, “The role of interfaces on an apparent grain size effect on the dielectric properties for ferroelectric barium titanate ceramics,” *Ferroelectrics*, vol. 206, no. 1, pp. 337–353, 1998.

[90] G. Arlt, U. Böttger, and S. Witte, “Dielectric dispersion of ferroelectric ceramics and single crystals at microwave frequencies,” *Ann. Phys.*, vol. 506, no. 7-8, pp. 578–588, 1994.

[91] A. Pugachev *et al.*, “Broken local symmetry in paraelectric BaTiO 3 proved by second harmonic generation,” *Phys. Rev. Lett.*, vol. 108, no. 24, p. 247601, 2012.

[92] R. Mazumder, D. Chakravarty, D. Bhattacharya, and A. Sen, “Spark plasma sintering of BiFeO 3,” *Mater. Res. Bull.*, vol. 44, no. 3, pp. 555–559, 2009.

[93] Y. Hirose, S. Ueno, K. Nakashima, and S. Wada, “Fabrication of BaTiO3/BiFeO3 Nano-complex Ceramics by Hydrothermal Method,” *Trans. Mater. Res. Soc. Jpn.*, vol. 39, no. 2, pp. 105–108, 2014.

[94] M. Ivanov, K. Klemkaite, A. Khinsky, A. Kareiva, and J. Banys, “Dielectric and Conductive Properties of Hydrotalcite,” *Ferroelectrics*, vol. 417, no. 1, pp. 136–142, 2011.

[95] A. Y. Alsalloum *et al.*, "Low-Temperature Crystallization Enables 21.9% Efficient Single-Crystal MAPbI3 Inverted Perovskite Solar Cells," *ACS Energy Lett.*, vol. 5, no. 2, pp. 657–662, 2020.
[96] Z. Chen *et al.*, "Single-crystal MAPbI3 perovskite solar cells exceeding 21% power conversion efficiency," *ACS Energy Lett.*, vol. 4, no. 6, pp. 1258–1259, 2019.
[97] M. Grätzel, "The light and shade of perovskite solar cells," *Nat. Mater.*, vol. 13, no. 9, p. 838, 2014.
[98] M. A. Green, A. Ho-Baillie, and H. J. Snaith, "The emergence of perovskite solar cells," *Nat. Photonics*, vol. 8, no. 7, p. 506, 2014.
[99] Q. Dong *et al.*, "Electron-hole diffusion lengths> 175 μm in solution-grown CH3NH3PbI3 single crystals," *Science*, vol. 347, no. 6225, pp. 967–970, 2015.
[100] D. Shi *et al.*, "Low trap-state density and long carrier diffusion in organolead trihalide perovskite single crystals," *Science*, vol. 347, no. 6221, pp. 519–522, 2015.
[101] S. D. Stranks *et al.*, "Electron-hole diffusion lengths exceeding 1 micrometer in an organometal trihalide perovskite absorber," *Science*, vol. 342, no. 6156, pp. 341–344, 2013.
[102] C. Wehrenfennig, G. E. Eperon, M. B. Johnston, H. J. Snaith, and L. M. Herz, "High charge carrier mobilities and lifetimes in organolead trihalide perovskites," *Adv. Mater.*, vol. 26, no. 10, pp. 1584–1589, 2014.
[103] Y. Bi, E. M. Hutter, Y. Fang, Q. Dong, J. Huang, and T. J. Savenije, "Charge carrier lifetimes exceeding 15 μs in methylammonium lead iodide single crystals," *J. Phys. Chem. Lett.*, vol. 7, no. 5, pp. 923–928, 2016.
[104] Y. Zhang, Y. Liu, Z. Yang, and S. F. Liu, "High-quality perovskite MAPbI3 single crystals for broad-spectrum and rapid response integrate photodetector," *J. Energy Chem.*, vol. 27, no. 3, pp. 722–727, 2018.
[105] T. Baikie *et al.*, "A combined single crystal neutron/X-ray diffraction and solid-state nuclear magnetic resonance study of the hybrid perovskites CH 3 NH 3 PbX 3 (X= I, Br and Cl)," *J. Mater. Chem. A*, vol. 3, no. 17, pp. 9298–9307, 2015.
[106] Z. Lian *et al.*, "High-performance planar-type photodetector on (100) facet of MAPbI 3 single crystal," *Sci. Rep.*, vol. 5, p. 16563, 2015.
[107] S. Sun *et al.*, "The origin of high efficiency in low-temperature solution-processable bilayer organometal halide hybrid solar cells," *Energy Environ. Sci.*, vol. 7, no. 1, pp. 399–407, 2014.

[108] A. Kojima, K. Teshima, Y. Shirai, and T. Miyasaka, “Organometal halide perovskites as visible-light sensitizers for photovoltaic cells,” *J. Am. Chem. Soc.*, vol. 131, no. 17, pp. 6050–6051, 2009.

[109] W. S. Yang *et al.*, “High-performance photovoltaic perovskite layers fabricated through intramolecular exchange,” *Science*, vol. 348, no. 6240, pp. 1234–1237, 2015.

[110] A. Poglitsch and D. Weber, “Dynamic disorder in methylammoniumtrihalogenoplumbates (II) observed by millimeter-wave spectroscopy,” *J. Chem. Phys.*, vol. 87, no. 11, pp. 6373–6378, 1987.

[111] H. Mashiyama, Y. Kawamura, H. Kasano, T. Asahi, Y. Noda, and H. Kimura, “Disordered configuration of methylammonium of CH3NH3PbBr3 determined by single crystal neutron diffractometry,” *Ferroelectrics*, vol. 348, no. 1, pp. 182–186, 2007.

[112] H. Mashiyama, Y. Kawamura, and Y. Kubota, “The Anti-Polar Structure of CH~ 3NH~ 3PbBr~ 3,” *J.-KOREAN Phys. Soc.*, vol. 51, no. 2, p. 850, 2007.

[113] H. Mashiyama, Y. Kurihara, and T. Azetsu, “Disordered Cubic Perovskite Structure of CH~ 3 NH~ 3PbX~ 3 (X= CI, Br, I),” *J.-KOREAN Phys. Soc.*, vol. 32, pp. S156–S158, 1998.

[114] T. Baikie *et al.*, “Synthesis and crystal chemistry of the hybrid perovskite (CH 3 NH 3) PbI 3 for solid-state sensitised solar cell applications,” *J. Mater. Chem. A*, vol. 1, no. 18, pp. 5628–5641, 2013.

[115] N. Onoda-Yamamuro, T. Matsuo, and H. Suga, “Calorimetric and IR spectroscopic studies of phase transitions in methylammonium trihalogenoplumbates (II),” *J. Phys. Chem. Solids*, vol. 51, no. 12, pp. 1383–1395, 1990.

[116] L. Chi, I. Swainson, L. Cranswick, J.-H. Her, P. Stephens, and O. Knop, “The ordered phase of methylammonium lead chloride CH3ND3PbCl3,” *J. Solid State Chem.*, vol. 178, no. 5, pp. 1376–1385, 2005.

[117] H. Röhm, T. Leonhard, M. Hoffmann, and A. Colsmann, “Energy Environ. Sci. 10, 950 (2017).”

[118] Y. Rakita *et al.*, “Tetragonal CH3NH3PbI3 is ferroelectric,” *Proc. Natl. Acad. Sci.*, vol. 114, no. 28, pp. E5504–E5512, 2017.

[119] Y. Kutes, L. Ye, Y. Zhou, S. Pang, B. D. Huey, and N. P. Padture, “Direct observation of ferroelectric domains in solution-processed CH3NH3PbI3 perovskite thin films,” *J. Phys. Chem. Lett.*, vol. 5, no. 19, pp. 3335–3339, 2014.

[120] J. M. Frost, K. T. Butler, F. Brivio, C. H. Hendon, M. Van Schilfgaarde, and A. Walsh, "Atomistic origins of high-performance in hybrid halide perovskite solar cells," *Nano Lett.*, vol. 14, no. 5, pp. 2584–2590, 2014.

[121] N. Onoda-Yamamuro, T. Matsuo, and H. Suga, "Dielectric study of CH3NH3PbX3 (X= Cl, Br, I)," *J. Phys. Chem. Solids*, vol. 53, no. 7, pp. 935–939, 1992.

[122] Q. Lin, A. Armin, R. C. R. Nagiri, P. L. Burn, and P. Meredith, "Electro-optics of perovskite solar cells," *Nat. Photonics*, vol. 9, no. 2, p. 106, 2015.

[123] J. G. Labram *et al.*, "Temperature-dependent polarization in field-effect transport and photovoltaic measurements of methylammonium lead iodide," *J. Phys. Chem. Lett.*, vol. 6, no. 18, pp. 3565–3571, 2015.

[124] J. M. Frost and A. Walsh, "What is moving in hybrid halide perovskite solar cells?," *Acc. Chem. Res.*, vol. 49, no. 3, pp. 528–535, 2016.

[125] J. R. MacDonald, "Impedence Spectroscopy--Emphasizing Solid Materials and Systems," *Wiley-Intersci. John Wiley Sons*, pp. 1–346, 1987.

[126] R. Truell, C. Elbaum, and B. B. Chick, *Ultrasonic methods in solid state physics*. Academic press, 2013.

[127] A. Létoublon *et al.*, "Elastic constants, optical phonons, and molecular relaxations in the high temperature plastic phase of the CH3NH3PbBr3 hybrid perovskite," *J. Phys. Chem. Lett.*, vol. 7, no. 19, pp. 3776–3784, 2016.

[128] Y. Rakita, S. R. Cohen, N. K. Kedem, G. Hodes, and D. Cahen, "Mechanical properties of APbX 3 (A= Cs or CH 3 NH 3; X= I or Br) perovskite single crystals," *MRS Commun.*, vol. 5, no. 4, pp. 623–629, 2015.

[129] U.-G. Jong, C.-J. Yu, J.-S. Ri, N.-H. Kim, and G.-C. Ri, "Influence of halide composition on the structural, electronic, and optical properties of mixed CH 3 NH 3 Pb (I 1− x Br x) 3 perovskites calculated using the virtual crystal approximation method," *Phys. Rev. B*, vol. 94, no. 12, p. 125139, 2016.

[130] R. E. Wasylishen, O. Knop, and J. B. Macdonald, "Cation rotation in methylammonium lead halides," *Solid State Commun.*, vol. 56, no. 7, pp. 581–582, 1985.

[131] C. Quarti, E. Mosconi, and F. De Angelis, "Interplay of orientational order and electronic structure in methylammonium lead iodide:

implications for solar cell operation," *Chem. Mater.*, vol. 26, no. 22, pp. 6557–6569, 2014.

[132] C. Carabatos-Nédelec and P. Becker, "Order–disorder and structural phase transitions in solid-state materials by Raman scattering analysis," *J. Raman Spectrosc.*, vol. 28, no. 9, pp. 663–671, 1997.

[133] M. T. Weller, O. J. Weber, P. F. Henry, A. M. Di Pumpo, and T. C. Hansen, "Complete structure and cation orientation in the perovskite photovoltaic methylammonium lead iodide between 100 and 352 K," *Chem. Commun.*, vol. 51, no. 20, pp. 4180–4183, 2015.

[134] J. Even, M. Carignano, and C. Katan, "Molecular disorder and translation/rotation coupling in the plastic crystal phase of hybrid perovskites," *Nanoscale*, vol. 8, no. 12, pp. 6222–6236, 2016.

[135] R. L. Milot, G. E. Eperon, H. J. Snaith, M. B. Johnston, and L. M. Herz, "Temperature-dependent charge-carrier dynamics in CH3NH3PbI3 perovskite thin films," *Adv. Funct. Mater.*, vol. 25, no. 39, pp. 6218–6227, 2015.

[136] I. Swainson, R. Hammond, C. Soulliere, O. Knop, and W. Massa, "Phase transitions in the perovskite methylammonium lead bromide, CH3ND3PbBr3," *J. Solid State Chem.*, vol. 176, no. 1, pp. 97–104, 2003.

[137] G. A. Sewvandi, K. Kodera, H. Ma, S. Nakanishi, and Q. Feng, "Antiferroelectric Nature of CH 3 NH 3 PbI 3− x Cl x Perovskite and Its Implication for Charge Separation in Perovskite Solar Cells," *Sci. Rep.*, vol. 6, no. 1, pp. 1–6, 2016.

[138] R. Ohmann *et al.*, "Real-space imaging of the atomic structure of organic–inorganic perovskite," *J. Am. Chem. Soc.*, vol. 137, no. 51, pp. 16049–16054, 2015.

[139] L. Korotkov and T. Korotkova, "Order parameter behavior in the vicinity of antiferroelectric phase transition in K1− x (NH4) xH2PO4 mixed crystals," *Solid State Commun.*, vol. 115, no. 8, pp. 453–455, 2000.

[140] A. Dziaugys, V. Shvartsman, J. Macutkevic, J. Banys, Y. Vysochanskii, and W. Kleemann, "Phase diagram of mixed Cu (In x Cr 1− x) P 2 S 6 crystals," *Phys. Rev. B*, vol. 85, no. 13, p. 134105, 2012.

[141] G.-C. Xu, X.-M. Ma, L. Zhang, Z.-M. Wang, and S. Gao, "Disorder− order ferroelectric transition in the metal formate framework of [NH4][Zn (HCOO) 3]," *J. Am. Chem. Soc.*, vol. 132, no. 28, pp. 9588–9590, 2010.

[142] C. C. Stoumpos, C. D. Malliakas, and M. G. Kanatzidis, "Semiconducting tin and lead iodide perovskites with organic cations:

phase transitions, high mobilities, and near-infrared photoluminescent properties," *Inorg. Chem.*, vol. 52, no. 15, pp. 9019–9038, 2013.
[143] H.-S. Kim *et al.*, "Ferroelectric polarization in CH3NH3PbI3 perovskite," *J. Phys. Chem. Lett.*, vol. 6, no. 9, pp. 1729–1735, 2015.
[144] P. Zhao *et al.*, "Spontaneous polarization behaviors in hybrid halide perovskite film," *Scr. Mater.*, vol. 102, pp. 51–54, 2015.
[145] Z. Xiao *et al.*, "Giant switchable photovoltaic effect in organometal trihalide perovskite devices," *Nat. Mater.*, vol. 14, no. 2, pp. 193–198, 2015.
[146] M. Coll *et al.*, "Polarization switching and light-enhanced piezoelectricity in lead halide perovskites," *J. Phys. Chem. Lett.*, vol. 6, no. 8, pp. 1408–1413, 2015.
[147] I. M. Hermes *et al.*, "Ferroelastic fingerprints in methylammonium lead iodide perovskite," *J. Phys. Chem. C*, vol. 120, no. 10, pp. 5724–5731, 2016.
[148] Z. Fan *et al.*, "Ferroelectricity of CH3NH3PbI3 perovskite," *J. Phys. Chem. Lett.*, vol. 6, no. 7, pp. 1155–1161, 2015.
[149] Y. Rong *et al.*, "Challenges for commercializing perovskite solar cells," *Science*, vol. 361, no. 6408, p. eaat8235, 2018.
[150] C. C. Boyd, R. Cheacharoen, T. Leijtens, and M. D. McGehee, "Understanding degradation mechanisms and improving stability of perovskite photovoltaics," *Chem. Rev.*, vol. 119, no. 5, pp. 3418–3451, 2018.
[151] W. Ke and M. G. Kanatzidis, "Prospects for low-toxicity lead-free perovskite solar cells," *Nat. Commun.*, vol. 10, no. 1, p. 965, 2019.
[152] M. Saliba *et al.*, "Cesium-containing triple cation perovskite solar cells: improved stability, reproducibility and high efficiency," *Energy Environ. Sci.*, vol. 9, no. 6, pp. 1989–1997, 2016.
[153] G. Eperon and S. Stranks, "C. Menelaou, MB Johnston, LM Herz and HJ Snaith," *Energy Env. Sci*, vol. 7, pp. 982–988, 2014.
[154] R. J. Sutton *et al.*, "Bandgap-tunable cesium lead halide perovskites with high thermal stability for efficient solar cells," *Adv. Energy Mater.*, vol. 6, no. 8, p. 1502458, 2016.
[155] T. Singh and T. Miyasaka, "Stabilizing the efficiency beyond 20% with a mixed cation perovskite solar cell fabricated in ambient air under controlled humidity," *Adv. Energy Mater.*, vol. 8, no. 3, p. 1700677, 2018.

[156] M. V. Lee *et al.*, “Transamidation of dimethylformamide during alkylammonium lead triiodide film formation for perovskite solar cells,” *J. Mater. Res.*, vol. 32, no. 1, pp. 45–55, 2017.

[157] W. Ke, I. Spanopoulos, C. C. Stoumpos, and M. G. Kanatzidis, “Myths and reality of HPbI 3 in halide perovskite solar cells,” *Nat. Commun.*, vol. 9, no. 1, pp. 1–9, 2018.

[158] W. M. Franssen, B. J. Bruijnaers, V. H. Portengen, and A. P. Kentgens, “Dimethylammonium incorporation in lead acetate based MAPbI3 Perovskite solar cells,” *ChemPhysChem*, vol. 19, no. 22, pp. 3107–3115, 2018.

[159] F. Shao *et al.*, “Enhanced Photovoltaic Performance and Thermal Stability of CH3NH3PbI3 Perovskite through Lattice Symmetrization,” *ACS Appl. Mater. Interfaces*, vol. 11, no. 1, pp. 740–746, 2018.

[160] B. Charles, J. Dillon, O. J. Weber, M. S. Islam, and M. T. Weller, “Understanding the stability of mixed A-cation lead iodide perovskites,” *J. Mater. Chem. A*, vol. 5, no. 43, pp. 22495–22499, 2017.

[161] A. Pisanu, A. Speltini, P. Quadrelli, G. Drera, L. Sangaletti, and L. Malavasi, “Enhanced air-stability of Sn-based hybrid perovskites induced by dimethylammonium (DMA): synthesis, characterization, aging and hydrogen photogeneration of the MA 1− x DMA x SnBr 3 system,” *J. Mater. Chem. C*, vol. 7, no. 23, pp. 7020–7026, 2019.

[162] C. Anelli *et al.*, “Investigation of Dimethylammonium Solubility in MAPbBr3 Hybrid Perovskite: Synthesis, Crystal Structure, and Optical Properties,” *Inorg. Chem.*, vol. 58, no. 1, pp. 944–949, 2018.

[163] M. Geselle and H. Fuess, “Crystal structure of dimethylammonium tribromoplumbate (II),(CH3) 2NH2PbBr3,” *Z. Für Krist.-New Cryst. Struct.*, vol. 212, no. 1, pp. 234–234, 1997.

[164] A. Mancini *et al.*, “Synthesis, structural and optical characterization of APbX3 (A= methylammonium, dimethylammonium, trimethylammonium; X= I, Br, Cl) hybrid organic-inorganic materials,” *J. Solid State Chem.*, vol. 240, pp. 55–60, 2016.

[165] A. García-Fernández *et al.*, “Hybrid lead halide [(CH 3) 2 NH 2] PbX 3 (X= Cl− and Br−) hexagonal perovskites with multiple functional properties,” *J. Mater. Chem. C*, vol. 7, no. 32, pp. 10008–10018, 2019.

[166] W. Kleemann, “Relaxor ferroelectrics: Cluster glass ground state via random fields and random bonds,” *Phys. Status Solidi B*, vol. 251, no. 10, pp. 1993–2002, 2014.

[167] A. Bokov and Z.-G. Ye, “Recent progress in relaxor ferroelectrics with perovskite structure,” *J. Mater. Sci.*, vol. 41, no. 1, pp. 31–52, 2006.
[168] B. Vugmeister and M. Glinchuk, “Dipole glass and ferroelectricity in random-site electric dipole systems,” *Rev. Mod. Phys.*, vol. 62, no. 4, p. 993, 1990.
[169] L. M. Herz, “How lattice dynamics moderate the electronic properties of metal-halide perovskites,” *J. Phys. Chem. Lett.*, vol. 9, no. 23, pp. 6853–6863, 2018.
[170] J. N. Wilson, J. M. Frost, S. K. Wallace, and A. Walsh, “Dielectric and ferroic properties of metal halide perovskites,” *APL Mater.*, vol. 7, no. 1, p. 010901, 2019.
[171] W. Kleemann, “Relaxor ferroelectrics: Cluster glass ground state via random fields and random bonds,” *Phys. Status Solidi B*, vol. 251, no. 10, pp. 1993–2002, 2014.
[172] S. Dorogovtsev and N. Yushin, “Acoustical properties of disordered ferroelectrics,” *Ferroelectrics*, vol. 112, no. 1, pp. 27–44, 1990.
[173] S. Lushnikov, A. Fedoseev, S. Gvasaliya, and S. Kojima, “Anomalous dispersion of the elastic constants at the phase transformation of the Pb Mg 1⁄3 Nb 2⁄3 O 3 relaxor ferroelectric,” *Phys. Rev. B*, vol. 77, no. 10, p. 104122, 2008.
[174] P. Jain, N. S. Dalal, B. H. Toby, H. W. Kroto, and A. K. Cheetham, “Order− disorder antiferroelectric phase transition in a hybrid inorganic− organic framework with the perovskite architecture,” *J. Am. Chem. Soc.*, vol. 130, no. 32, pp. 10450–10451, 2008.
[175] P. Jain *et al.*, “Multiferroic behavior associated with an order− disorder hydrogen bonding transition in metal− organic frameworks (MOFs) with the perovskite ABX3 architecture,” *J. Am. Chem. Soc.*, vol. 131, no. 38, pp. 13625–13627, 2009.
[176] K. D. Hughey *et al.*, “Structure–Property Relations in Multiferroic [(CH3) 2NH2] M (HCOO) 3 (M= Mn, Co, Ni),” *Inorg. Chem.*, vol. 57, no. 18, pp. 11569–11577, 2018.
[177] W. Zhang and R.-G. Xiong, “Ferroelectric metal–organic frameworks,” *Chem. Rev.*, vol. 112, no. 2, pp. 1163–1195, 2012.
[178] P. Jain *et al.*, “Switchable electric polarization and ferroelectric domains in a metal-organic-framework,” *Npj Quantum Mater.*, vol. 1, no. 1, pp. 1–6, 2016.

[179] X.-Y. Wang, L. Gan, S.-W. Zhang, and S. Gao, “Perovskite-like metal formates with weak ferromagnetism and as precursors to amorphous materials,” *Inorg. Chem.*, vol. 43, no. 15, pp. 4615–4625, 2004.

[180] M. Sánchez-Andújar, S. Presedo, S. Yáñez-Vilar, S. Castro-García, J. Shamir, and M. Señarís-Rodríguez, “Characterization of the order− disorder dielectric transition in the hybrid organic− inorganic perovskite-like formate Mn (HCOO) 3 [(CH3) 2NH2],” *Inorg. Chem.*, vol. 49, no. 4, pp. 1510–1516, 2010.

[181] J.-R. Li, J. Sculley, and H.-C. Zhou, “Metal–organic frameworks for separations,” *Chem. Rev.*, vol. 112, no. 2, pp. 869–932, 2012.

[182] W.-Q. Liao *et al.*, “A molecular perovskite solid solution with piezoelectricity stronger than lead zirconate titanate,” *Science*, vol. 363, no. 6432, pp. 1206–1210, 2019.

[183] B. Pato-Doldán *et al.*, “Near room temperature dielectric transition in the perovskite formate framework [(CH 3) 2 NH 2][Mg (HCOO) 3],” *Phys. Chem. Chem. Phys.*, vol. 14, no. 24, pp. 8498–8501, 2012.

[184] Y. Tian *et al.*, “Cross coupling between electric and magnetic orders in a multiferroic metal-organic framework,” *Sci. Rep.*, vol. 4, p. 6062, 2014.

[185] D. Fu *et al.*, “A multiferroic perdeutero metal–organic framework,” *Angew. Chem. Int. Ed.*, vol. 50, no. 50, pp. 11947–11951, 2011.

[186] N. Abhyankar *et al.*, “Understanding ferroelectricity in the Pb-free perovskite-like metal–Organic framework [(CH3) 2NH2] Zn (HCOO) 3: Dielectric, 2D NMR, and theoretical studies,” *J. Phys. Chem. C*, vol. 121, no. 11, pp. 6314–6322, 2017.

[187] R. Yadav, D. Swain, H. Bhat, and S. Elizabeth, “Order-disorder phase transition and multiferroic behaviour in a metal organic framework compound (CH3) 2NH2Co (HCOO) 3,” *J. Appl. Phys.*, vol. 119, no. 6, p. 064103, 2016.

[188] R. Cowley, S. Gvasaliya, S. Lushnikov, B. Roessli, and G. Rotaru, “Relaxing with relaxors: a review of relaxor ferroelectrics,” *Adv. Phys.*, vol. 60, no. 2, pp. 229–327, 2011.

[189] Z. Yu, C. Ang, R. Guo, and A. Bhalla, “Ferroelectric-relaxor behavior of Ba (Ti 0.7 Zr 0.3) O 3 ceramics,” *J. Appl. Phys.*, vol. 92, no. 5, pp. 2655–2657, 2002.

[190] T. Asaji, S. Yoshitake, Y. Ito, and H. Fujimori, “Phase transition and cationic motion in the perovskite formate framework [(CH3) 2NH2][Mg (HCOO) 3],” *J. Mol. Struct.*, vol. 1076, pp. 719–723, 2014.

[191] T. Asaji and K. Ashitomi, “Phase Transition and Cationic Motion in a Metal–Organic Perovskite, Dimethylammonium Zinc Formate [(CH3) 2NH2][Zn (HCOO) 3],” *J. Phys. Chem. C*, vol. 117, no. 19, pp. 10185–10190, 2013.

[192] V. Bovtun *et al.*, “Broad-band dielectric response of PbMg1/3Nb2/3O3 relaxor ferroelectrics: Single crystals, ceramics and thin films,” *J. Eur. Ceram. Soc.*, vol. 26, no. 14, pp. 2867–2875, 2006.

[193] A. Loidl, J. Hemberger, M. Winterlich, H. Ries, and R. Böhmer, “Linear and nonlinear dielectric spectroscopy in dipolar glasses,” *Ferroelectrics*, vol. 176, no. 1, pp. 43–59, 1996.

[194] J. Banys *et al.*, “Dipolar glass behaviour in mixed CuInP2 (S0. 7Se0. 3) 6 crystals,” *Ferroelectrics*, vol. 318, no. 1, pp. 163–168, 2005.

[195] J. Scott, “Ferroelectrics go bananas,” *J. Phys. Condens. Matter*, vol. 20, no. 2, p. 021001, 2007.

[196] A. Tagantsev, V. Sherman, K. Astafiev, J. Venkatesh, and N. Setter, “Ferroelectric materials for microwave tunable applications,” *J. Electroceramics*, vol. 11, no. 1–2, pp. 5–66, 2003.

Acknowledgements

I'm truly thankful to:

Dr. Maksim Ivanov for guiding me through bachelor, master and PhD studies, and for participating in all those scientific discussions about ferroelectrics.

Prof. dr. Jūras Banys for providing friendly and fruitful working environment, for encouraging in doing various jobs and for all those scientific and non-scientific talks.

Dr. Mantas Šimėnas for all the collaborations and of course for being a great colleague and friend.

Dr. Martynas Kinka, Dr. Vytautas Samulionis for helping me with acoustic measurements and giving new insight about the compounds.

Prof. Dr. Doru Lupascu, Prof. dr. Satoshi Wada, Prof. dr. Miroslaw Maczka for providing samples for this thesis.

Dr. Vidmantas Kalendra for sharing an office and not kicking me out.

Dr. Robertas Grigalaitis, dr. Jan. Matcutkevic for all the projects and collaborations.

All the friends and colleagues dr. Šarūnas Svirskas, dr. Edita Palaiminė, dr. dr. Ilona Zamaraitė, dr. Ieva Kranauskaitė, dr. Jaroslavas Belovickis, dr. Džiugas Jablonskas, dr. Saulius Rudys, dr. Artyomas Plyushch for accepting me.

And lastly, I would like to thank my wife Egle Balčiūniene, my sister Nadežda Kovaliova - Matiukienė, and my parents Audris Balčiūnas and Svetlana Balčiūniene for supporting during all my studies.

Appendix A

Purity of the phases is confirmed by XRD, see Figure 1.

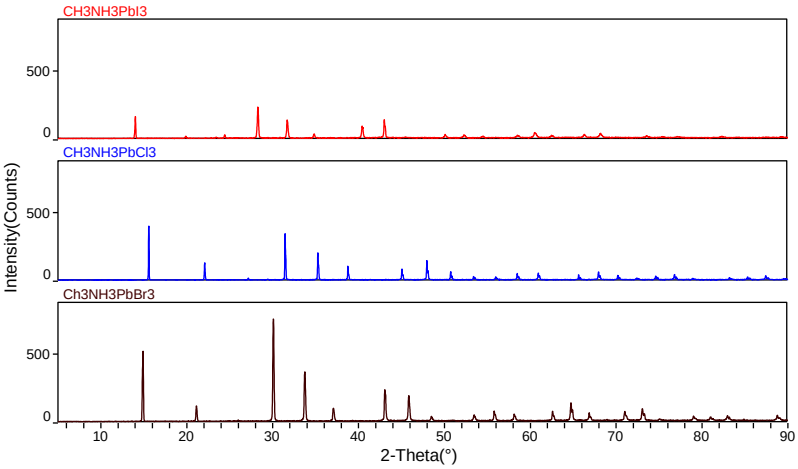

Figure 1 X-ray diffraction spectra for the $MAPbI_3$ (a), $MAPbCl_3$ (b), and $MAPbBr_3$ (c) samples.

Differential scanning calorimetry measurements display several phase transitions as endothermic or exothermic peaks upon heating or cooling respectively (Figure 2). A thermal hysteresis of ~ 4-6 K between measurements on cooling and heating show that the phase transitions are of 1st order. Further a temperature dependence of inverse dielectric permittivity at 1GHz reveals a negative Curie – Weiss temperature in $MAPbI_3$ and $MAPbBr_3$ crystals indicating anti-polar nature (Figure 3).

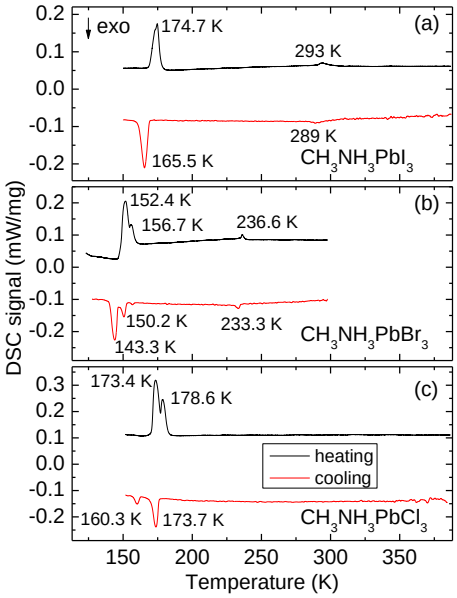

Figure 2 Results of differential scanning calorimetry measurements for (a) $CH_3NH_3PbI_3$, (b) $CH_3NH_3PbBr_3$, and (c)

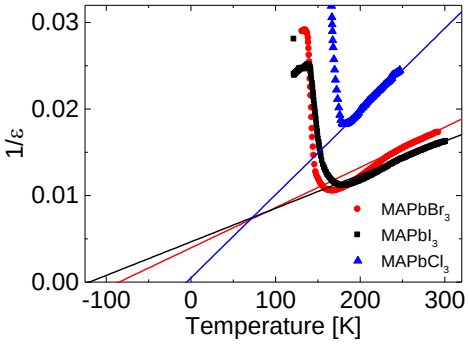

Figure 3 Inverse of dielectric constant at 1 GHz. Negative T_0 in a Curie-Weiss fit reflects anti-polar order.

Appendix B

Temperature dependence of real and imaginary parts of dielectric permittivity of $DMAPbBr_3$ (Figure 1) show anomaly at 251 K temperature which is related to hexagonal to monoclinic first order phase transition. Although due to narrow frequency range the movement of DMA molecule was not observed. Further temperature dependence of acoustic velocity and attenuation for $DMA_xMA_{1-x}PbBr_3$ crystals are shown in the figure 2. Here two anomalies for DMA concentrations of x =0 and 0.04 are observed and one very broad anomaly for DMA concentration of x = 0.14 and 0.21.

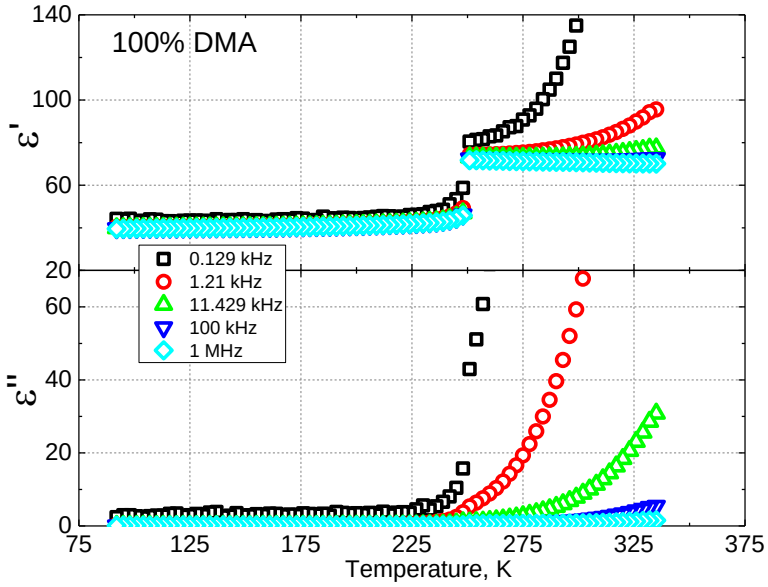

Figure 1 Temperature dependence of real (top) and imaginary (bottom) parts of dielectric permittivity.

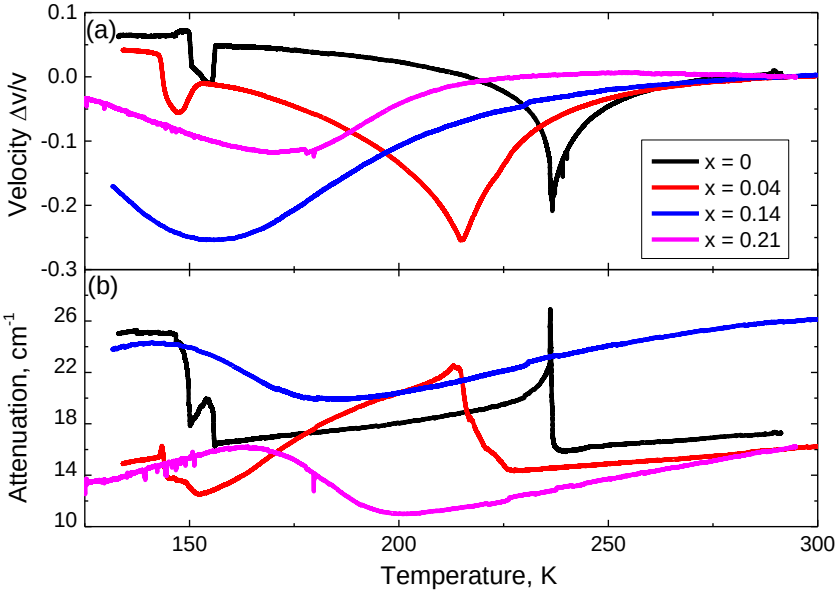

Figure 2 Temperature dependence of acoustic velocity (a) and attenuation (b) for $DMA_xMA_{1-x}PbBr_3$ *crystals.*

Appendix C

The inverse temperature dependence of relaxation time shown in figure 1 was obtained by evaluating the maxima position in the imaginary part of dielectric permittivity of $DMAZn(HCOO)_3$. The activation energy value is very close to the value of DMA hopping in the high temperature phase.

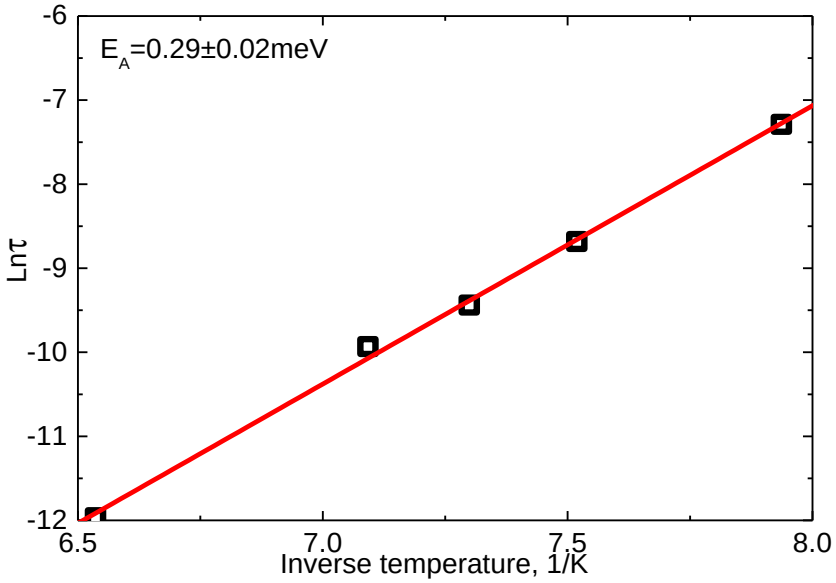

Figure 1 inverse temperature dependence of relaxation times of low temperature relaxation for $DMAZn(HCOO)_3$.

Vilnius University Press
9 Saulėtekio Ave., Building III, LT-10222 Vilnius
Email: info@leidykla.vu.lt, www.leidykla.vu.lt
Print run copies 20